Astronomy & Astrophysics manuscript no. PSZcatalogue
March 20, 2013

Planck 2013 results. XXIX. *Planck* catalogue of Sunyaev–Zeldovich sources

Planck Collaboration: P. A. R. Ade[96], N. Aghanim[66*], C. Armitage-Caplan[101], M. Arnaud[79], M. Ashdown[76,7], F. Atrio-Barandela[21], J. Aumont[66], H. Aussel[79], C. Baccigalupi[94], A. J. Banday[107,11], R. B. Barreiro[73], R. Barrena[72], M. Bartelmann[105,85], J. G. Bartlett[1,74], E. Battaner[110], K. Benabed[67,104], A. Benoît[64], A. Benoit-Lévy[29,67,104], J.-P. Bernard[11], M. Bersanelli[40,56], P. Bielewicz[107,11,94], I. Bikmaev[24,3], J. Bobin[79], J. J. Bock[74,12], H. Böhringer[86], A. Bonaldi[75], J. R. Bond[10], J. Borrill[16,98], F. R. Bouchet[67,104], M. Bridges[76,7,70], M. Bucher[1], R. Burenin[97,89], C. Burigana[55,38], R. C. Butler[55], J.-F. Cardoso[80,1,67], P. Carvalho[7], A. Catalano[81,78], A. Challinor[70,76,13], A. Chamballu[79,18,66], R.-R. Chary[63], X. Chen[63], L.-Y Chiang[69], H. C. Chiang[32,8], G. Chon[86], P. R. Christensen[90,43], E. Churazov[85,97], S. Church[100], D. L. Clements[62], S. Colombi[67,104], L. P. L. Colombo[28,74], B. Comis[81], F. Couchot[77], A. Coulais[78], B. P. Crill[74,91], A. Curto[7,73], F. Cuttaia[55], A. Da Silva[14], H. Dahle[71], L. Danese[94], R. D. Davies[75], R. J. Davis[75], P. de Bernardis[39], A. de Rosa[55], G. de Zotti[52,94], J. Delabrouille[1], J.-M. Delouis[67,104], J. Démoclès[79], F.-X. Désert[59], C. Dickinson[75], J. M. Diego[73], K. Dolag[109,85], H. Dole[66,65], S. Donzelli[56], O. Doré[74,12], M. Douspis[66], X. Dupac[46], G. Efstathiou[70], T. A. Enßlin[85], H. K. Eriksen[71], F. Feroz[7], F. Finelli[55,57], I. Flores-Cacho[11,107], O. Forni[107,11], M. Frailis[54], E. Franceschi[55], S. Fromenteau[1,66], S. Galeotta[54], K. Ganga[1], R. T. Génova-Santos[72], M. Giard[107,11], G. Giardino[47], M. Gilfanov[85,97], Y. Giraud-Héraud[1], J. González-Nuevo[73,94], K. M. Górski[74,112], K. J. B. Grainge[7,76], S. Gratton[76,70], A. Gregorio[41,54], N, E. Groeneboom[71], A. Gruppuso[55], F. K. Hansen[71], D. Hanson[87,74,10], D. Harrison[70,76], A. Hempel[72,44], S. Henrot-Versillé[77], C. Hernández-Monteagudo[15,85], D. Herranz[73], S. R. Hildebrandt[12], E. Hivon[67,104], M. Hobson[7], W. A. Holmes[74], A. Hornstrup[19], W. Hovest[85], K. M. Huffenberger[111], G. Hurier[66,81], N. Hurley-Walker[7], T. R. Jaffe[107,11], A. H. Jaffe[62], W. C. Jones[32], M. Juvela[31], E. Keihänen[31], R. Keskitalo[26,16], I. Khamitov[102,24], T. S. Kisner[83], R. Kneissl[45,9], J. Knoche[85], L. Knox[34], M. Kunz[20,66,4], H. Kurki-Suonio[31,50], G. Lagache[66], A. Lähteenmäki[2,50], J.-M. Lamarre[78], A. Lasenby[7,76], R. J. Laureijs[47], C. R. Lawrence[74], J. P. Leahy[75], R. Leonardi[46], J. León-Tavares[48,2], J. Lesgourgues[103,93], C. Li[84,85], A. Liddle[95,30], M. Liguori[37], P. B. Lilje[71], M. Linden-Vørnle[19], M. López-Caniego[73], P. M. Lubin[35], J. F. Macías-Pérez[81], C. J. MacTavish[76], B. Maffei[75], D. Maino[40,56], N. Mandolesi[55,6,38], M. Maris[54], D. J. Marshall[79], P. G. Martin[10], E. Martínez-González[73], S. Masi[39], S. Matarrese[37], F. Matthai[85], P. Mazzotta[42], S. Mei[49,106,12], P. R. Meinhold[35], A. Melchiorri[39,58], J.-B. Melin[18], L. Mendes[46], A. Mennella[40,56], M. Migliaccio[70,76], S. Mitra[61,74], M.-A. Miville-Deschênes[66,10], A. Moneti[67], L. Montier[107,11], G. Morgante[55], D. Mortlock[62], D. Munshi[96], P. Naselsky[90,43], F. Nati[39], P. Natoli[38,5,55], N. P. H. Nesvadba[66], C. B. Netterfield[23], H. U. Nørgaard-Nielsen[19], F. Noviello[75], D. Novikov[62], I. Novikov[90], I. J. O'Dwyer[74], M. Olamaie[7], S. Osborne[100], C. A. Oxborrow[19], F. Paci[94], L. Pagano[39,58], F. Pajot[66], D. Paoletti[55,57], F. Pasian[54], G. Patanchon[1], T. J. Pearson[12,63], O. Perdereau[77], L. Perotto[81], Y. C. Perrott[7], F. Perrotta[94], F. Piacentini[39], M. Piat[1], E. Pierpaoli[28], D. Pietrobon[74], S. Plaszczynski[77], E. Pointecouteau[107,11], G. Polenta[5,53], N. Ponthieu[66,59], L. Popa[68], T. Poutanen[50,31,2], G. W. Pratt[79], G. Prézeau[12,74], S. Prunet[67,104], J.-L. Puget[66], J. P. Rachen[25,85], W. T. Reach[108], R. Rebolo[72,17,44], M. Reinecke[85], M. Remazeilles[66,1], C. Renault[81], S. Ricciardi[55], T. Riller[85], I. Ristorcelli[107,11], G. Rocha[74,12], C. Rosset[1], G. Roudier[1,78,74], M. Rowan-Robinson[62], J. A. Rubiño-Martín[72,44], C. Rumsey[7], B. Rusholme[63], M. Sandri[55], D. Santos[81], R. D. E. Saunders[7,76], G. Savini[92], D. Scott[27], M. D. Seiffert[74,12], E. P. S. Shellard[13], T. W. Shimwell[7], L. D. Spencer[96], J.-L. Starck[79], V. Stolyarov[7,76,99], R. Stompor[1], R. Sudiwala[96], R. Sunyaev[85,97], F. Sureau[79], D. Sutton[70,76], A.-S. Suur-Uski[31,50], J.-F. Sygnet[67], J. A. Tauber[47], D. Tavagnacco[54,41], L. Terenzi[55], L. Toffolatti[22,73], M. Tomasi[56], M. Tristram[77], M. Tucci[20,77], J. Tuovinen[88], M. Türler[60], G. Umana[51], L. Valenziano[55], J. Valiviita[50,31,71], B. Van Tent[82], L. Vibert[66], P. Vielva[73], F. Villa[55], N. Vittorio[42], L. A. Wade[74], B. D. Wandelt[67,104,36], M. White[33], S. D. M. White[85], D. Yvon[18], A. Zacchei[54], and A. Zonca[35]

(Affiliations can be found after the references)

Preprint online version: March 20, 2013

ABSTRACT

We describe the all-sky *Planck* catalogue of clusters and cluster candidates derived from Sunyaev–Zeldovich (SZ) effect detections using the first 15.5 months of *Planck* satellite observations. The catalogue contains 1227 entries, making it over six times the size of the *Planck* Early SZ (ESZ) sample and the largest SZ-selected catalogue to date. It contains 861 confirmed clusters, of which 178 have been confirmed as clusters, mostly through follow-up observations, and a further 683 are previously-known clusters. The remaining 366 have the status of cluster candidates, and we divide them into three classes according to the quality of evidence that they are likely to be true clusters. The *Planck* SZ catalogue is the deepest all-sky cluster catalogue, with redshifts up to about one, and spans the broadest cluster mass range from (0.1 to 1.6) $\times 10^{15}\,M_{\odot}$. Confirmation of cluster candidates through comparison with existing surveys or cluster catalogues is extensively described, as is the statistical characterization of the catalogue in terms of completeness and statistical reliability. The outputs of the validation process are provided as additional information. This gives, in particular, an ensemble of 813 cluster redshifts, and for all these *Planck* clusters we also include a mass estimated from a newly-proposed SZ-mass proxy. A refined measure of the SZ Compton parameter for the clusters with X-ray counter-parts is provided, as is an X-ray flux for all the *Planck* clusters not previously detected in X-ray surveys.

Key words. large-scale structure of Universe – Galaxies: clusters: general – Catalogs

* Corresponding author: N. Aghanim
nabila.aghanim@ias.u-psud.fr

1. Introduction

This paper, one of a set associated with the 2013 release of data from the *Planck*[1] mission (Planck Collaboration I 2013), describes the construction and properties of the *Planck* catalogue of SZ sources (PSZ).

Clusters of galaxies play several important roles in astrophysics and cosmology. As rare objects, their number density is especially sensitive to properties of the cosmological model such as the amplitude of primordial density perturbations (Peebles 1980), and their development with redshift probes the growth of cosmic structure, hence perhaps helping to distinguish between dark energy and modified gravity explanations for cosmic acceleration (e.g., see reviews by Borgani & Kravtsov 2009; Allen et al. 2011). The galaxies, hot gas and dark matter held in their gravitational potential wells provide a sample of the universal abundance of these components (e.g., Voit 2005), while the thermal state of the gas probes both the cluster formation mechanism and physical processes within the cluster such as cooling and energy-injection feedback (e.g., reviews by Fabian 2012; McNamara & Nulsen 2012). The study of the constituent galaxies, including the brightest cluster galaxies normally found at their centres, allows sensitive tests of galaxy formation models.

Because of these uses, there is considerable interest in developing large galaxy cluster catalogues that can be used for population and cosmological studies (e.g., Schuecker et al. 2003; Böhringer et al. 2004). Clusters are genuinely multi-wavelength objects that can be selected in several ways: optical/infrared (IR) imaging of the galaxy populations; X-ray imaging of bremsstrahlung radiation from the hot cluster gas; and through the Sunyaev–Zeldovich (SZ) effect (Sunyaev & Zeldovich 1972; Sunyaev & Zeldovich 1980) whereby scattering of cosmic microwave background (CMB) photons from that hot gas distorts the spectral shape of the CMB along lines of sight through clusters and groups.

Construction of cluster catalogues in the optical/IR and in the X-ray are relatively mature activities. The first large optical cluster survey is now over 50 years old (Abell 1958; Abell et al. 1989), and current catalogues constructed from the Sloan Digital Sky Survey data contain over a hundred thousand clusters (e.g., Koester et al. 2007; Wen et al. 2012). In X-rays, large samples first became available via *ROSAT* satellite observations (e.g., Vikhlinin et al. 1998; Böhringer et al. 2000; Gioia et al. 2003; Böhringer et al. 2004; Burenin et al. 2007; Ebeling et al. 2007), but also more recently for instance from dedicated or serendipitous survey with *XMM-Newton* (Pacaud et al. 2007; Fassbender et al. 2011; Takey et al. 2011; Mehrtens et al. 2012). Currently several thousand X-ray selected clusters are known (see for instance the meta-catalogue MCXC by Piffaretti et al. 2011). By contrast, although proposed about fifteen years ago (e.g., Barbosa et al. 1996; Aghanim et al. 1997), it is only very recently that SZ-selected samples have reached a significant size, with publication of samples containing several hundred clusters from the Early SZ (ESZ) catalogue from the *Planck* Satellite (Planck Collaboration VIII 2011), the South Pole Telescope (SPT, Reichardt et al. 2013) and the Atacama Cosmology Telescope (ACT, Hasselfield et al. 2013).

[1] *Planck* (http://www.esa.int/Planck) is a project of the European Space Agency (ESA) with instruments provided by two scientific consortia funded by ESA member states (in particular the lead countries France and Italy), with contributions from NASA (USA) and telescope reflectors provided by a collaboration between ESA and a scientific consortium led and funded by Denmark.

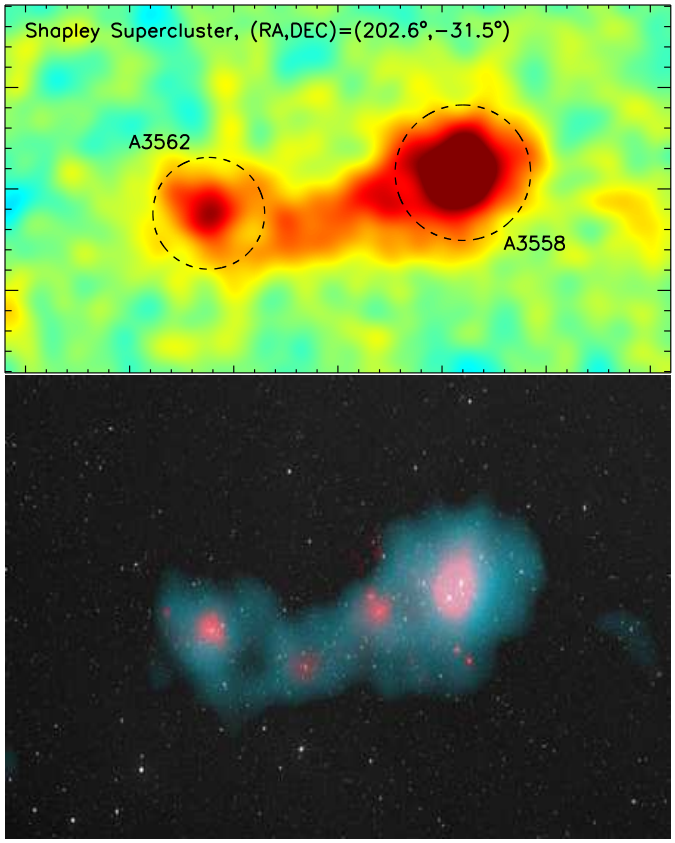

Fig. 1: The Shapley super-cluster as seen in the *Planck* survey. *Upper panel:* reconstructed thermal SZ map 3.2×1.8 square degrees from MILCA (Hurier et al. 2010). The dotted circles represent apertures of θ_{500} from the MCXC meta-catalogue around the resolved clusters. *Lower panel:* composite view of the optical from DSS images, X-rays from *ROSAT* (light pink) survey and from the thermal SZ effect as seen in *Planck* (cyan).

The usefulness of the different selection methods, particularly for cosmology, depends not just on the total number of clusters identified but also on how readily the selection function of the survey can be modelled, and on how well the observed cluster properties can be related to quantities such as the total cluster mass that are most readily predicted from theory (e.g., see Voit 2005). It has proven difficult to capitalize on the large size of optical/IR cluster samples because the observable, the number of galaxies in each cluster, exhibits large scatter with respect to the total cluster mass (e.g., Johnston et al. 2007). In this regard the X-ray selected samples are considerably more powerful, due to the tighter correlations of X-ray properties with mass (Arnaud et al. 2005; Vikhlinin et al. 2006; Pratt et al. 2009; Reichert et al. 2011; Maughan et al. 2012). Simulations predict that SZ-selected surveys may do even better, with a very tight relation between SZ signal and mass (e.g., da Silva et al. 2004; Motl et al. 2005; Nagai 2006; Wik et al. 2008; Aghanim et al. 2009; Angulo et al. 2012). Moreover, this relation, except at low redshifts, corresponds to a nearly redshift-independent mass limit, thus allowing such surveys to reach to high redshift and provide a strong lever arm on growth of structure.

We report on the construction and properties of the PSZ catalogue, which is to date the largest SZ-selected cluster catalogue and has value added through compilation of ancillary informa-

tion. It contains 1227 entries including many multiple systems, e.g., the Shapley super-cluster displayed in Fig. 1 together with a composite image. Of these 861 are confirmed, amongst which 178 are new discoveries, whilst amongst the 366 candidate clusters 54 are of high reliability (CLASS1 in our terminology), 170 are reliable, and the remaining 142 are in the lowest reliability class. In Sect. 2 we start with a description of the *Planck* data used to provide cluster candidates, and the two different methodologies (one of which has two independent implementations) used to carry out the extraction of the SZ sources. In Sect. 3 we provide a characterization of the PSZ catalogue in terms of completeness, statistical reliability, and accuracy of cluster parameters including size and photometry. Section 4 extensively describes validation of cluster candidates through pre-existing surveys and cluster catalogues in many wavebands, while Sect. 5 describes the follow-up campaigns conducted by the *Planck* collaboration to confirm new cluster discoveries. This leads to a description of the catalogue properties in Sect. 6. The physical properties of the clusters are exploited in Sect. 7. These include an update of the SZ–X-ray scaling relations from the *Planck* data, the measure of the X-ray flux for all SZ detections, and the production of homogenized SZ-mass estimates for 813 clusters with measured redshifts that are provided to the community as a value-added element to the *Planck* SZ catalogue.

Throughout the article, the quantities M_{500} and R_{500} stand for the total mass and radius where the mean enclosed density is 500 times the critical density at the cluster redshift. The SZ flux is denoted Y_{500}, where $Y_{500}\, D_{\rm A}^2$ is the spherically-integrated Compton parameter within R_{500}, and $D_{\rm A}$ is the angular-diameter distance to the cluster. The physical cluster quantities are computed with a fiducial ΛCDM cosmology with $H_0 = 70\,{\rm km\,s^{-1}\,Mpc^{-1}}$, $\Omega_{\rm m} = 0.3$ and $\Omega_\Lambda = 0.7$. Furthermore, all the fits are undertaken in the log-log plane using the BCES orthogonal regression method of Akritas & Bershady (1996), with bootstrap resampling, which allows for intrinsic scatter as well as uncertainties in both variables. All uncertainties are given at 68 per cent confidence level and all dispersions are given in $\log_{10}$.

2. Construction of the *Planck* SZ Catalogue

2.1. Input Planck data

The *Planck* catalogue of SZ sources is constructed from the total intensity data taken during the first 15.5 months of *Planck* survey observations. Raw data were first processed to produce cleaned time-lines (time-ordered information) and associated flags correcting for different systematic effects; channel maps were then produced for all the observing frequencies (see details in Planck Collaboration VI 2013; Planck Collaboration II 2013). These maps, together with the associated beam characteristics, are the main inputs for the SZ-finder algorithms presented in Sect. 2.2. Following Planck Collaboration VIII (2011), we used the six highest-frequency *Planck* channel maps, from 100 to 857 GHz, to produce the catalogue of SZ detections. This optimizes the signal-to-noise (S/N) of the extracted SZ detections and the usable sky fraction; see Appendix A for the choice of channel maps.

In order to optimize the SZ detection, together with avoiding contamination of the PSZ catalogue by bright point sources (PS), the latter are masked from the channel maps prior to the SZ detection as detailed in the following. To construct the PS mask, we use the *Planck* Catalogue of Compact Sources (PCCS). The PCCS (Planck Collaboration XXVIII 2013) is a collection of single-frequency source catalogues, one for each of the nine *Planck* frequency channels. The six single *Planck*-HFI frequency PS catalogues are used to first produce individual-frequency masks constructed by masking a radius equivalent to 1.28 FWHM ($3\,\sigma_{\rm beam}$) around every point source detected with $({\rm S/N})_{\rm PS} \geq 10$. Then a single common PS mask (see Fig. 2), which is the union of the six individual HFI-frequency channel masks, is constructed. It is applied to all six highest-frequency *Planck* channel-maps to mask the point sources prior to running the algorithms to detect SZ signal. The masked regions are filled using a harmonic in-painting method based on that of Bajkova (2005), which has the advantage of eliminating the discontinuities caused by the masking. In order to avoid any possible artificial spurious detections at the edges of the in-painted area, we further reject detections within an expanded common mask, constructed using the same procedure as described above, but using a masking radius equivalent to 2.13 FWHM ($5\,\sigma_{\rm beam}$) and covering less than 2.9% of the sky.

Bright radio sources are known to exist at the centre of galaxy clusters, but they generally have steep spectra and hence their flux is significantly reduced at the six highest *Planck* frequencies where the PS mask is constructed and where the clusters are detected. The Perseus cluster (see Fig. 19 later and the associated discussion) is one exception, with a point source that is so bright that the cluster is masked and thus not included in the *Planck* SZ catalogue.

2.2. Detection Methods

The catalogue of SZ sources is the result of a blind multi-frequency search, i.e., no prior positional information on known clusters is used as input to the detection, by three detection algorithms briefly described below. These algorithms were described and tested using simulations (Melin et al. 2012). They were used to construct the Early SZ (ESZ) *Planck* sample by Planck Collaboration VIII (2011). All three assume priors on the cluster spectral and spatial characteristics, which optimize the SZ detection by enhancing the SZ contrast over a set of observations containing contaminating signals. In the following we present the cluster model used as a template by the SZ-finder algorithms and we briefly describe the three detection methods (for details we refer the reader to Herranz et al. 2002; Melin et al. 2006; Carvalho et al. 2009, 2011; Melin et al. 2012).

2.2.1. Cluster model

The baseline pressure profile model used in the detection methods is the generalized NFW (Navarro et al. 1997) profile of Arnaud et al. (2010). This profile model was constructed by combining the observed, scaled, X-ray pressure profile of 31 clusters from the REXCESS sample (Böhringer et al. 2007) for $R < R_{500}$[2], with the mean pressure profile from three sets of numerical simulations (Borgani et al. 2004; Nagai et al. 2007; Piffaretti & Valdarnini 2008) for $R_{500} < R < 5\,R_{500}$. New observational constraints on the pressure distribution at $R > R_{500}$ have become available. Planck Collaboration Int. V (2013) constrained the detection of the thermal pressure distribution out to about $3\,R_{500}$ through stacking of the observed SZ profiles of 62 nearby massive clusters detected with high significance in the *Planck* ESZ sample. The resulting profile is in agreement with that derived for the Coma cluster (Planck Collaboration Int. X

[2] R_{500} relates to the characteristic cluster scale $R_{\rm s}$ through the NFW concentration parameter $c_{500} = 1.177$ for the baseline profile ($R_{\rm s} = R_{500}/c_{500}$).

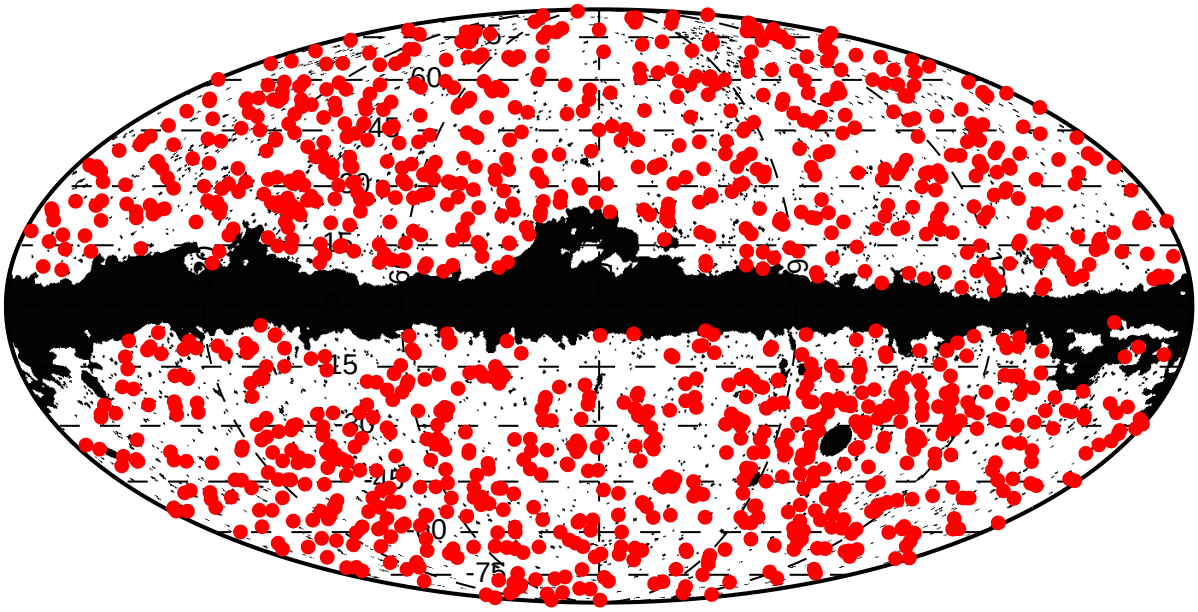

Fig. 2: The distribution, shown in Mollweide projection with the Galactic plane horizontal and the Milky Way centre in the middle, of the 1227 *Planck* clusters and candidates across the sky (red thick dots). The masked point-sources (black thin dots), the Magellanic clouds (large black areas) and the Galactic mask, covering a total of 16.3% of the sky and used by the SZ-finder algorithms to detect SZ sources, are also shown.

2013). Both show a slightly flatter distribution in the outer parts (i.e., beyond R_{500}) with respect to the predictions from the numerical simulations. These results are further confirmed by independent measurements from Bolocam in a smaller radial range ($r < 2\,R_{500}$, Sayers et al. 2012b). Using the profile of Planck Collaboration Int. V (2013) does not affect the detection yield (see Sect. 3) and only slightly modifies the measure of the SZ flux density (see Sect. 7.5) as compared to the generalized NFW (GNFW) profile adopted in the three cluster. The fiducial model parameters for the GNFW profile are given by the parameterization of the pressure profile in Eq. 12 of Arnaud et al. (2010). It states

$$\mathbf{p}(x) = \frac{P_0}{(c_{500}x)^{\gamma}\,[1 + (c_{500}x)^{\alpha}]^{(\beta-\gamma)/\alpha}}\,, \qquad (1)$$

with the parameters

$$[P_0, c_{500}, \gamma, \alpha, \beta] = [8.40\,h_{70}^{-3/2}, 1.18, 0.308, 1.05, 5.49]\,. \qquad (2)$$

The (weak) mass dependence of the profiles is neglected. Within the SZ-finder algorithms, the size and amplitude of the profile are allowed to vary but all other parameters are fixed. The cluster model is thus equivalent to a shape function characterized by two free parameters, its amplitude and a characteristic scale $\theta_s = \theta_{500}/c_{500}$.

2.2.2. Matched Multi-filter (MMF)

Two different implementations of the matched multi-frequency filter algorithm (`MMF1` and `MMF3`) are used to detect SZ clusters. Both are extensions, over the whole sky, of the `MMF` algorithm (Herranz et al. 2002; Melin et al. 2006). The matched filter optimizes the cluster detection using a linear combination of maps (which requires an estimate of the statistics of the contamination) and uses spatial filtering to suppress both foregrounds and noise (making use of the prior knowledge of the cluster pressure profile and thermal SZ spectrum).

The `MMF1` algorithm divides the full-sky *Planck* frequency maps into 640 patches, each 14.66×14.66 square degrees, covering 3.33 times the sky. The `MMF3` algorithm divides the maps into a smaller set of 504 overlapping square patches of area 10×10 square degrees with the sky covered 1.22 times. The smaller redundancy of `MMF3` with respect to `MMF1` implies a potentially lower reliability of the SZ detections. In order to increase the reliability of the detections, the `MMF3` algorithm is thus run in two iterations. After a first detection of the SZ candidates, a subsequent run centred on the positions of the candidates refines the estimated S/N and candidate properties. If the S/N of a detection falls below the threshold at the second iteration, it is removed from the catalogue. For both implementations, the matched multi-frequency filter optimally combines the six frequencies of each patch. Auto- and cross-power spectra are directly estimated from the data and are thus adapted to the local instrumental noise and astrophysical contamination, which constitutes the dominant noise contribution. Figure 3 illustrates, for a six arcmin filter size, the ensemble noise maps as measured by `MMF3` in each of the patches. For both `MMF1` and `MMF3`, the detection of the SZ-candidates is performed on all the patches, and the resultant sub-catalogues are merged together to produce a single SZ-candidate catalogue per method.

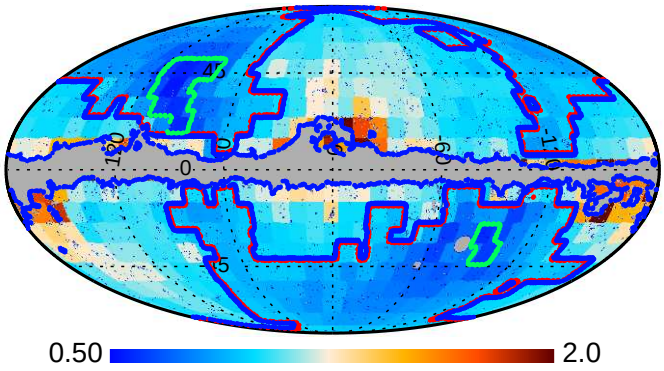

Fig. 3: The noise maps per detection patch of MMF3 method measured for a six arcmin filter. The noise ranges from 0.5 to 2 times the average noise of the map, which is $\sigma_Y = 2.4 \times 10^{-4}$ arcmin^2. The Ecliptic polar regions, delimited by green contours, with increased redundancy in the observations define a deep survey zone covering in total 2.7% of the sky. It is less noisy than the areas near the Galactic plane, where the dust emission is higher. Two other zones are defined: a medium-deep survey zone of 41.3% coverage delimited by the red contours and with higher noise level; and a shallow-survey zone covering 56% of the sky and with the highest noise levels including regions near the Galactic plane.

The candidate size in both algorithms is estimated by filtering the patches over the range of potential scales, and finding the scale that maximizes the S/N of the detected candidate. When merging the sub-catalogues produced from the analysis of individual patches, it is also the S/N of the detection (the refined S/N estimate for MMF3) which is used when deciding which detection of the candidate is kept. Furthermore, both MMF1 and MMF3 can also be run with fixed cluster size and position to estimate the SZ signal. This version of the algorithms is used to assess the reliability of the association with known clusters and/or to refine the measurement of the integrated Compton parameters of known X-ray clusters, as presented in Sect. 7.2.1.

2.2.3. PowellSnakes

PowellSnakes (PwS) is different from the MMF methods. It is a fast Bayesian multi-frequency detection algorithm designed to identify and characterize compact objects buried in a diffuse background. The detection process is grounded in a statistical model comparison test. The statistical foundations of PwS are described in Carvalho et al. (2009), and more recently in Carvalho et al. (2011) with a greater focus on the *Planck* setup. PwS may be run either based on a Generalized Likelihood Ratio Test or in full Bayesian mode. This duality allows PwS measured quantities to be consistently compared with those of the MMF algorithms.

PwS also operates in square flat patches of 14.66×14.66 square degrees. The total number of patches employed, of order 2800, varies with sky area but always guarantees a very large overlap; on average each cluster is detected about 4.7 times. PwS detects putative clusters and at the same time it computes the evidence ratio and samples from the posterior distributions of the cluster parameters. Then, it merges all intermediate sub-catalogues and applies the criterion of acceptance/rejection (Carvalho et al. 2011). PwS computes the cross-channel covariance matrix directly from the pixel data. To reduce the contamination of the background by the SZ signal itself, the estimation of the covariance matrix is performed iteratively. After an initial estimate, all detections in the patch with S/N higher than the current target detection are subtracted from the data using their best-fit values and the cross-channel covariance matrix is re-estimated. This is PwS '*native*' mode of background estimation that produces, on average, an S/N estimate about 20% higher than MMF. However, in order to produce a homogeneous *Planck* SZ catalogue from the three algorithms, it is possible to run PwS in '*compatibility*' mode, skipping the re-estimation step to mimic more closely the evaluation of the background noise cross-power spectrum of the MMF algorithms and thus their evaluation of the S/N. In this mode, PwS is a maximum likelihood estimator like the MMF.

In the following, unless stated otherwise, all quoted or plotted S/N values from PwS are obtained in '*compatibility*' mode in order to ensure homogeneity across the catalogue entries and in order to ease the comparison with the MMF outputs.

2.3. Outputs of the detection methods

Each of the three detection algorithms outputs a catalogue of SZ detections above S/N = 4.5 outside the highest-emitting Galactic regions (this corresponds to a mask of about 15% of the sky, see masked area in Fig. 2) and the Small and Large Magellanic Clouds and outside the PS mask described in Sect. 2.1. The union PS-Galactic mask covers 16.3% of the sky. The survey area used for the SZ detections in *Planck* is thus 83.7% of the sky coverage. The three individual lists of SZ candidates are cleaned by removal of obvious false detections. These are spurious sources that pass the MMF and PwS filters despite the pre-processing step applied to the *Planck* channel maps, see Sect. 2.1. In order to identify them, we cross-match the SZ detections with an intermediate, low signal-to-noise cut of 4, catalogue of point sources detected at the highest frequencies of *Planck*. Galactic sources in dense and cold regions at high latitudes also contaminate the SZ detections outside the Galactic mask. These cold Galactic sources (CGS hereafter, see Planck Collaboration XXIII 2011; Planck Collaboration XXII 2011) are detected in the *Planck* channel maps following an optimized method proposed by Montier et al. (2010). The SZ detections matching with PS at both 545 and 857 GHz, or with CGS sources, all show a rising spectrum at high frequencies, indicating that they are false detections. The SZ detections corresponding to such PCCS or CG sources are removed from the individual lists and from the published *Planck* catalogue of SZ sources.

The three detection algorithms used in the present study deploy the GNFW cluster profile to detect SZ signal with the two parameters of the shape function, the central value and the characteristic scale θ_s let free, with $\theta_s = \theta_{500}/c_{500}$. Each of the three algorithms therefore assigns, to each detected SZ candidate, a position with estimated uncertainty, a signal-to-noise value, and an estimated size, θ_s or equivalently θ_{500}, with its uncertainty. The detection likelihood or the posterior probability of the integrated Compton parameter within $5\theta_{500}$, denoted $Y_{5R_{500}}$, exhibits a large correlation with the size. Figure 4 illustrates the likelihood plots for two cases: a spatially-resolved cluster detected with a high signal-to-noise, Abell 2163; and a non-resolved cluster at high redshift ($z \simeq 1$), PSZ1 G266.6-27.3 (also known as PLCK G266.6-27.3 in Planck Collaboration XXVI 2011). We also show in Fig. 5 the distribution of maximum likelihood SZ fluxes ($Y_{5R_{500}}$) and sizes (θ_{500}) for the MMF3 detections.

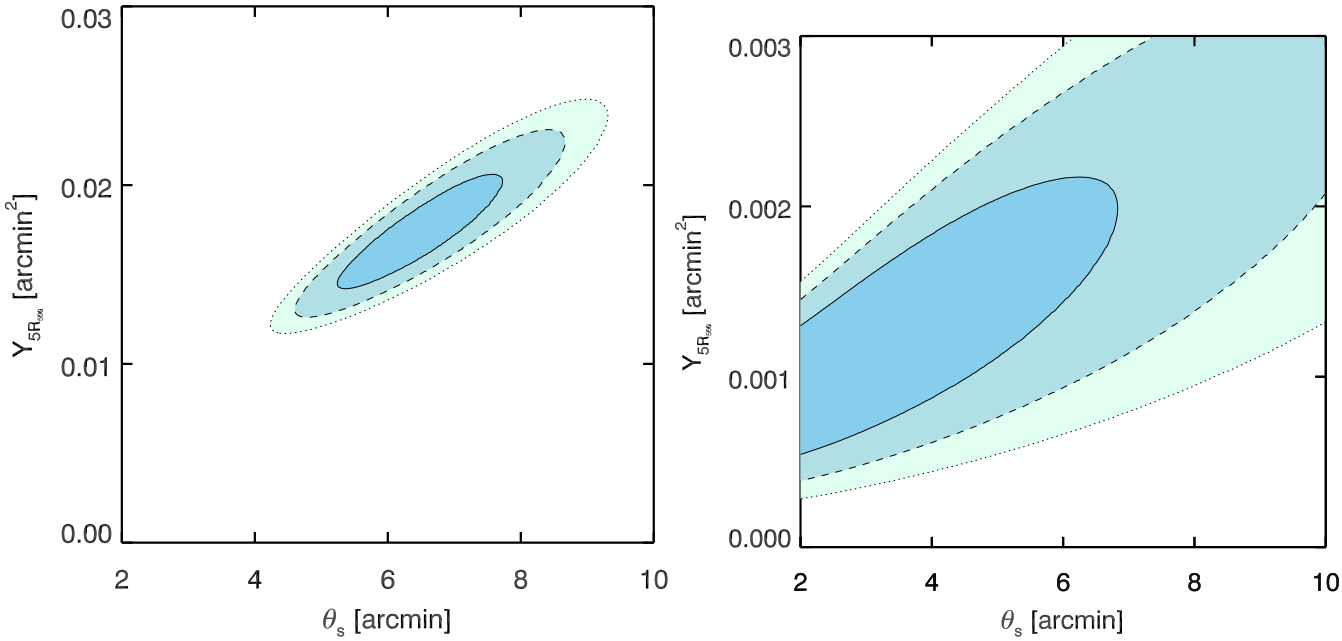

Fig. 4: Illustration of the SZ size–flux degeneracy for two clusters detected by *Planck*. *Right:* Abell 2163 (S/N = 27) and *left:* PSZ1 G266.6-27.3 (S/N = 6 at $z \simeq 1$). The contours show the 68, 95, and 99 percent confidence levels.

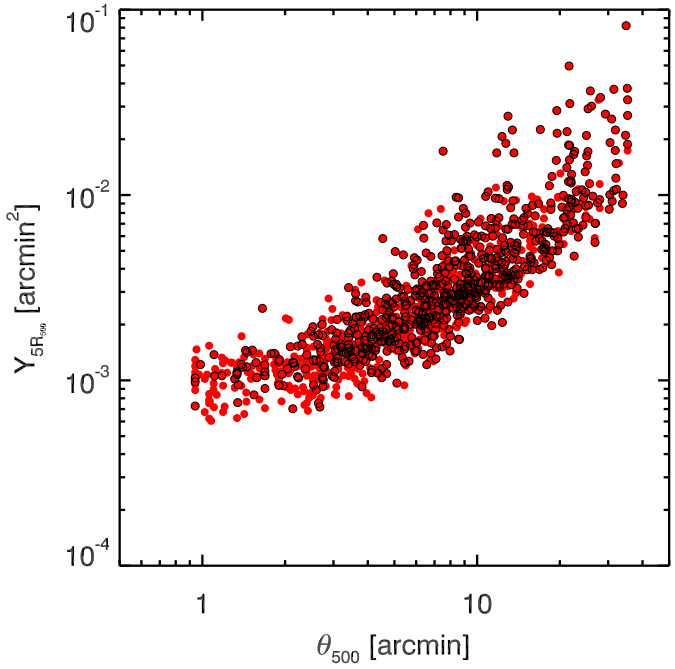

Fig. 5: Distribution of the maximum likelihood SZ flux $Y_{5R_{500}}$ and size θ_{500} for *Planck* SZ detections in the union catalogue down to S/N = 4.5. Detections associated with known or new confirmed clusters are shown as open black circles. SZ cluster candidates are shown as filled-red circles.

This "degeneracy" between cluster size and SZ flux propagates the size uncertainty to the SZ flux estimate, increasing and biasing its value dramatically. This effect being so detrimental, both the SZ blind flux and size best-fit estimates, and respective error bars, are not quoted in the catalogue outputs to avoid their misuse. Only the full joint $Y_{5R_{500}}-\theta_s$, or equivalently $Y_{5R_{500}}-\theta_{500}$, posterior probability contours provide a complete description of the information output by each detection method. They are thus provided for each detection. In order to use the flux measure, one ought to break the size–flux degeneracy. This can be achieved by a joint analysis with a high-resolution observation of the same objects, or by assuming a prior on, or fixing, the cluster size e.g., to the X-ray size. The SZ signal can then be re-extracted with an uncertainty much smaller than the variation of the joint Y–θ probability distribution.

We now perform a systematic comparison of the outputs of the three algorithms. We compare the S/N ratio. In addition and for purposes of illustration, we compare the best-fit blind Y value from maximum-likelihood or posterior probability outputs, namely $Y_{5R_{500}}$[3]. We show the comparison in Fig. 6, considering detections down to S/N = 4.5. We quantify the difference between a given quantity estimated by two different algorithms, Q_2 and Q_1, by fitting a power law to the data in the form $Q_2/Q_p = 10^A (Q_1/Q_p)^\alpha$ with a pivot $Q_p = 6$ for S/N and $Q_p = 4\times10^{-3}$arcmin^2 for $Y_{5R_{500}}$. The results are given in Table 1, including the scatter estimates. The raw scatter was estimated using the error-weighted vertical distances to the regression line. The intrinsic scatter on Y_{500} was computed from the quadratic difference between the raw scatter and that expected from the statistical uncertainties. Table 1 also lists the mean difference in logarithm, $\Delta(\log Q)=\log(Q_2/Q_1)$, computed taking into account both statistical errors and intrinsic scatter, estimated iteratively.

2.3.1. Signal-to-noise

A crucial ingredient of the SZ detection algorithms, either the MMFs or PwS, is the background cross-power spectrum used to estimate the noise level. It is evaluated from the data locally on a per-patch basis (see Fig. 3 for an example of the noise per patch

[3] $Y_{5R_{500}}$ can be rescaled to Y_{500} for the fiducial GNFW model as $Y_{5R_{500}} = 1.79 \times Y_{500}$ (Arnaud et al. 2010).

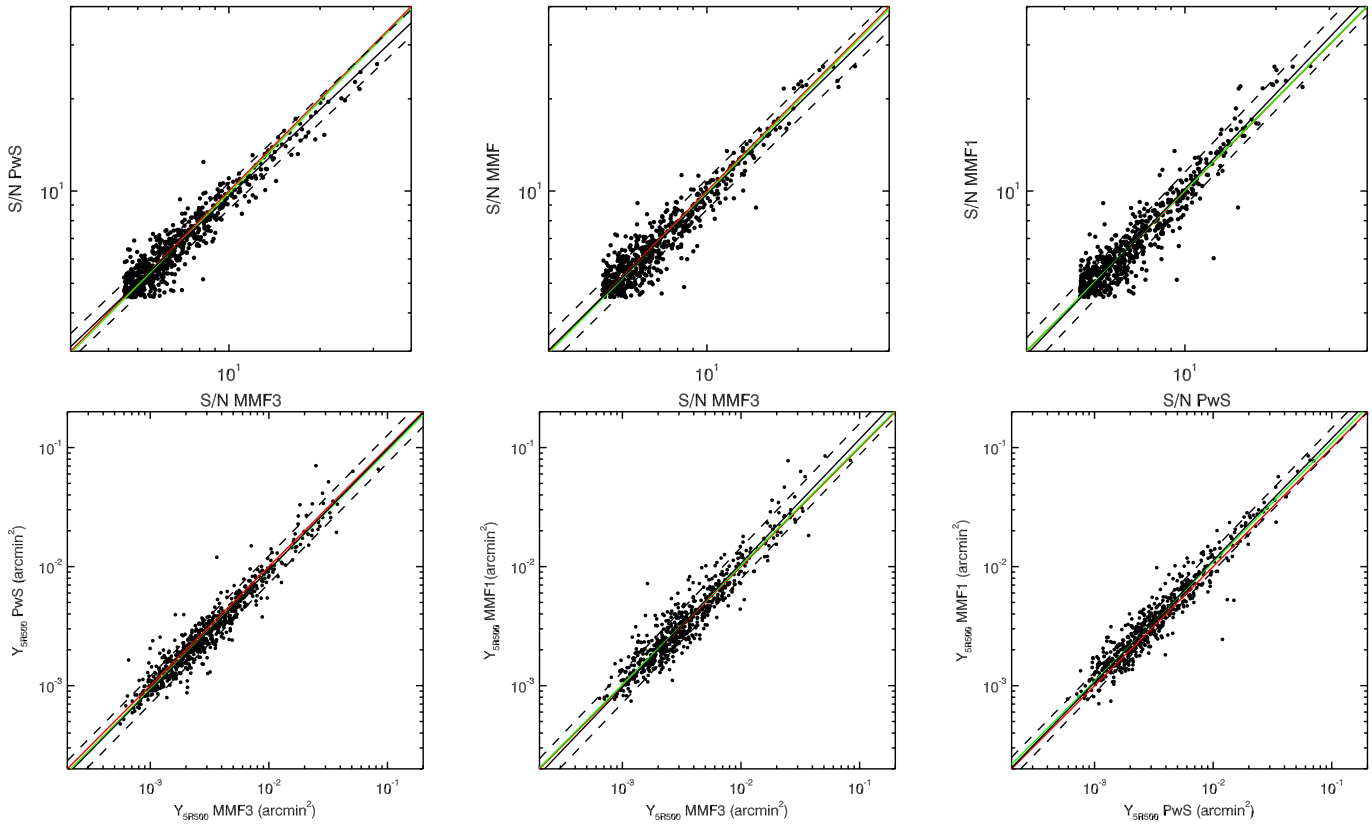

Fig. 6: Comparison of S/N (top panels) and maximum likelihood Compton-parameter values (bottom panels) from the three detection algorithms, MMFs and PwS, down to S/N = 4.5 after removing obvious false detections (see Sect. 2.3). In each panel, the red line denotes the equality line. The black line is the best fit to the data, and the dashed lines correspond to the $\pm 1\sigma$ dispersion about the fit relation. For clarity, error bars are omitted on $Y_{5R_{500}}$ values in the plot, but are taken into account in the fit. The green line of slope fixed to unity corresponds to the mean offset between the two quantities.

Table 1: Quantitative comparison between S/N and maximum likelihood Compton-parameter $Y_{5R_{500}}$ values from the three individual algorithms. Column(1): considered pair of algorithms ; Column(2-3): slope and normalization of the best-fit relation between the quantities estimated by the two algorithms, $Q_2/Q_p = 10^A\,(Q_1/Q_p)^\alpha$, using BCES orthogonal regression, with the pivot being $Q_p = 6$ for S/N and $Q_p = 4\times10^{-3}$ arcmin^2 for $Y_{5R_{500}}$; Column (4-5) intrinsic and raw scatter around the best-fit relation; Column (6): mean difference in logarithm, $\Delta(\log(Q))=\log(Q_2/Q_1)$; Column (7-8): corresponding intrinsic scatter and raw scatter.

	Power-law fit				Mean offset		
S/N	A	α	$\sigma_{\log}$		$\Delta\log(Q)$	$\sigma_{\log}$	
MMF3–PwS	-0.003 ± 0.002	0.94 ± 0.01	0.043 ± 0.002		-0.006 ± 0.002	0.045 ± 0.002	
MMF3–MMF1	-0.005 ± 0.002	0.97 ± 0.01	0.050 ± 0.002		-0.006 ± 0.002	0.051 ± 0.002	
PwS–MMF1	-0.000 ± 0.002	1.04 ± 0.02	0.054 ± 0.003		$+0.002 \pm 0.002$	0.054 ± 0.002	
$Y_{5R_{500}}$	A	α	$\sigma_{\log,\mathrm{int}}$	$\sigma_{\log,\mathrm{raw}}$	$\Delta\log(Q)$	$\sigma_{\log,\mathrm{int}}$	$\sigma_{\log,\mathrm{raw}}$
MMF3–PwS	-0.030 ± 0.004	1.01 ± 0.01	0.08 ± 0.03	0.116 ± 0.018	-0.027 ± 0.004	0.065 ± 0.006	0.102
MMF3–MMF1	$+0.011 \pm 0.005$	1.04 ± 0.02	0.11 ± 0.02	0.131 ± 0.014	$+0.010 \pm 0.005$	0.085 ± 0.006	0.118
PwS–MMF1	$+0.041 \pm 0.004$	1.02 ± 0.01	0.04 ± 0.01	0.088 ± 0.005	$+0.038 \pm 0.004$	0.040 ± 0.007	0.079

across the sky). The algorithms, and implementations, slightly differ with respect to the stabilization assumptions (e.g., smoothing) of the background noise cross-power spectrum and to the treatment of the background SZ signal, now acting as a contaminant. These differences translate into variations in the S/N values per method. In particular, when operated in "*compatibility*" mode (without background cluster subtraction), PwS estimation of the background cross-power spectrum is more affected than the MMF by SZ signal contamination. The SZ signal adds an extra component to the background noise producing lower S/N estimates. This is particularly noticeable when the SZ signal is very strong compared with background (typically S/N $\geq$ 15).

Despite the differences in background estimates, the yields from the three algorithms agree. In the left panel of Fig. 7, we show that the detection counts as a function of S/N for each detection method are in good overall agreement. The right panel of Fig. 7 shows the fraction of common detections over the union of detections from all three algorithms as a function of S/N. Sources with S/N > 8.5 are detected by all three methods. However, we note that PwS number counts decrease more rapidly than MMF counts above S/N = 15. This reflects the be-

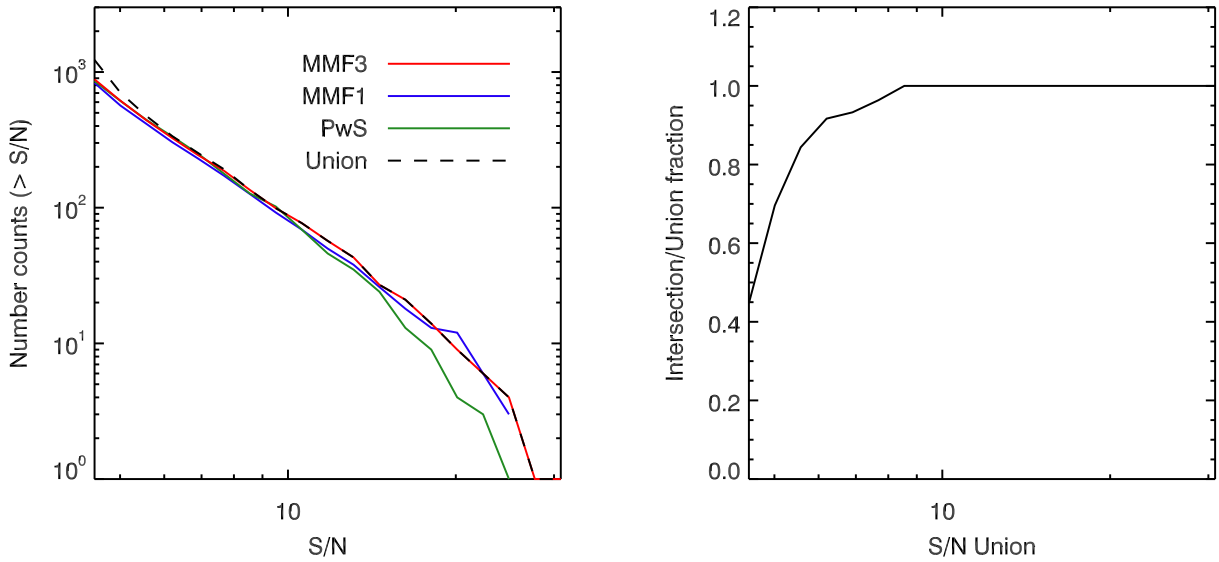

Fig. 7: *Left:* detection number counts as a function of S/N of the individual algorithms. The S/N value in the union catalogue is that of the MMF3 detections when available, followed by that of PwS followed by MMF1 (see Sect. 2.4). See text for discussion on the lower S/N values of PwS compared to the MMF-based algorithms. *Right:* fraction of common detection over counts from the union catalogue. Sources with S/N > 8.5 are detected by all methods.

haviour of PwS in "*compatibility*" mode described above, which estimates a higher background than the MMF methods at high S/N. Figure 6 shows the comparison of the S/N estimates from all three methods. The agreement is good on average. The mean ratio (or the normalization at the pivot of the power-law relation) deviates from unity by less than 2% and at less than $3\,\sigma$ significance. Here again at high S/N values, we note the tendency for lower S/N in PwS as compared to MMF (Fig. 6), and indeed the slope of the power-law relation is smaller than unity ($\alpha = 0.94 \pm 0.01$ for MMF3).

2.3.2. Photometry

We now compare the best-fit Y values (from maximum likelihood and posterior probability) for the three detection algorithms. The comparison (Fig. 6, lower panels) shows a systematic bias with PwS, yielding slightly smaller values than MMF, typically by 10%. However, the slope is consistent with unity, showing that this bias is not flux dependent. The MMF values differ from each other by less than 3% on average. The scatter between Y estimates is dominated by the intrinsic scatter (Table 1). It is clearly related to the size–flux degeneracy, the ratio between Y estimates for a given candidate being correlated with the size estimate ratio, as illustrated by Fig. 8. The scatter becomes compatible with the statistical scatter when a prior on the size is used, e.g., size fixed to the X-ray size.

2.4. Definition of the Planck SZ catalogue

As discussed above, the processing details of each algorithm/implementation differ in the computation of the background noise. The significance of the detections in terms of S/N, although in overall agreement, differs from one algorithm to the other and translates into different yields for the candidate lists from the three algorithms. We choose to construct a catalogue of SZ candidates that ensures, through redundant detections, an increased reliability of the low S/N sources, when they are detected by two methods at least, together with maximizing the yield of the catalogue.

The *Planck* SZ cluster catalogue described in the following is thus constructed from the union of the cleaned SZ-candidate lists produced at S/N $\geq$ 4.5 by all three algorithms. It contains in total 1227 SZ detections above S/N = 4.5. Note that in order to ensure homogeneity, in terms of detection significance, the S/N values of PwS quoted in the the union catalogue are obtained in *compatibility* mode, whereas the S/N obtained from PwS *native* mode are quoted in the PwS individual list. The union catalogue is constructed by merging detections from the three methods within an angular separation of at most five arcmin, in agreement with *Planck* position accuracy shown later in Fig. 12. As mentioned, no reference photometry is provided. However a reference position for the SZ detection is needed. For compatibility with the ESZ *Planck* sample, in the case of matching detection between methods we arbitrarily choose to take the coordinates from the MMF3 detection as the fiducial position (MMF3 was the reference method used to construct the ESZ *Planck* sample). When no detection by MMF3 above S/N = 4.5 is reported, we took the PwS coordinates as fiducial, and the MMF1 coordinates elsewhere. The S/N values in the union catalogue are taken following the same order, which explains why the MMF3 curve in Fig. 6 coincides with the union curve. The cluster candidates in the union catalogue are cross-referenced with the detections in the individual lists. The reference positions and the S/N values are reported in the union catalogue. Given the size–flux degeneracy, the full information on the degeneracy between size and flux is provided with each individual list in the form of the two-dimensional marginal probability distribution for each cluster candidate as discussed above. It is specified on a grid of 256×256 values in θ_s and $Y_{5R_{500}}$ centred at the best-fit values found by each algorithm for each SZ detection.

An extract of the *Planck* SZ catalogue is given in Appendix B. The full online table for union *Planck* catalogue, the individual lists of SZ detections, and the union mask used by the SZ-finder algorithms together with comments assembled

Table 2: Statistical characteristics of the *Planck* SZ catalogues. The intersection is defined as the set of SZ detections common between to three extraction algorithms. Completeness is a function of both Y_{500} and θ_{500}: the Y_{500} at a given completeness is estimated by marginalizing over θ_{500}, weighting each (Y_{500}, θ_{500}) bin by the theoretically-expected cluster counts. Positional accuracy is the median angular separation between real and estimated positions.

	Stat. Reliability(%)	Y_{500} 10^{-3} arcmin^2 at **C**% completeness			Positional accuracy (arcmin)
		C=50	**C**=80	**C**=95	
Union	84	0.61	1.2	3.2	1.2
Intersection	98	0.85	1.8	6.6	1.1
MMF1	87	0.75	1.6	4.7	1.2
MMF3	91	0.71	1.5	3.8	1.2
PwS	92	0.65	1.4	3.2	0.9

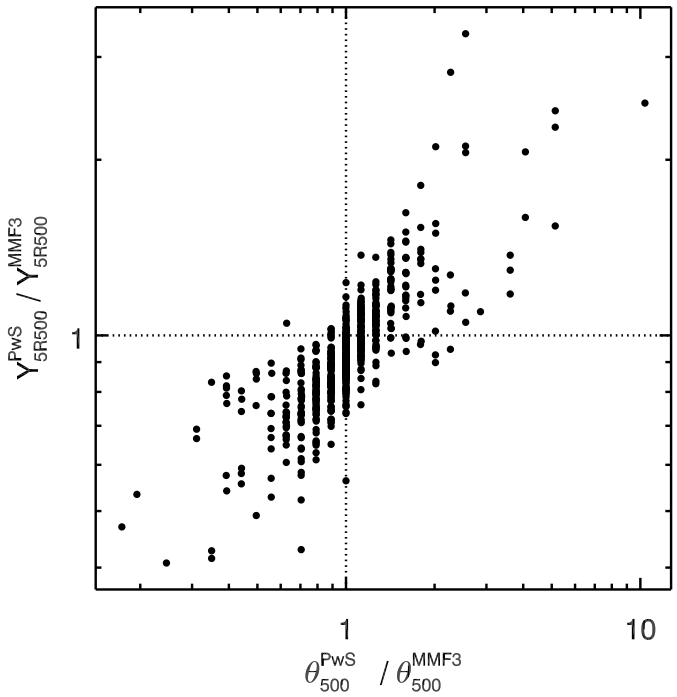

Fig. 8: Correlation between the ratio of $Y_{5R_{500}}$ estimates with PwS and MMF3 and the ratio of size estimates, shown on a grid of sizes.

in an external file are available at ESA's *Planck* Legacy Archive (PLA)[4].

3. Statistical Characterization

The statistical characterization of the PSZ catalogue is achieved through a process of MonteCarlo quality assessment (MCQA) that can be applied to each individual catalogue and to the merged union catalogues. The statistical quantities produced include completeness, fraction of detections associated with true clusters called, statistical reliability or purity, positional accuracy, and accuracy of parameter estimation. Together, these statistics describe the quality of detections in the catalogue. The quality of the parameter estimation, including astrometry (cluster position and extent), is determined through comparison with the parameters of the input clusters. The statistical characteristics of the different lists are summarized in Table 2.

3.1. MCQA Pipeline and simulations

The MCQA pipeline contains a common segment producing simulated input catalogues and processed, source-injected maps, which are then fed into the detection pipeline. In summary, the pipeline steps per MonteCarlo loop are:

1. creation of an input cluster catalogue;
2. injection of clusters into common simulated diffuse frequency maps, including beam convolution;
3. injection of multi-frequency point sources;
4. pre-processing of maps, including masking and filling point sources;
5. detection and construction of individual cluster-candidate catalogues;
6. construction of a union catalogue given merging criteria;
7. collation of input and output catalogues, producing detection truth-tables and catalogues of unmatched spurious detections[5].

To estimate the completeness, clusters are injected into the real data. In this case, steps 3 and 4 are skipped and each detection algorithm estimates noise statistics on the real data prior to injection in order to avoid artificially raising the S/N and biasing the completeness estimates. The pressure profiles of the injected clusters follow that described in Sect. 2.2.1. To account for the profile variation across the cluster population, the profile parameters are drawn from the covariance matrix of the 62 measured pressure profiles from Planck Collaboration Int. V (2013), ensuring that the injected profiles are consistent with measured dispersion and consistent, on average, with the extraction filter. The injected clusters are convolved with effective beams in each pixel including asymmetry computed following Mitra et al. (2011).

The simulated input cluster catalogues differ for statistical reliability and completeness determination. For completeness, clusters injected in real data are drawn from a uniform distribution in (Y_{500}, θ_{500}) so as to provide equal statistics in each completeness bin. To avoid an over-contamination of the signal, injected clusters are constrained to lie outside an exclusion radius of $5R_{500}$ around a cluster, either detected in the data or injected.

For the statistical reliability estimation of the input cluster distribution injected in simulations is such that cluster masses and redshifts are drawn from a Tinker et al. (2008) mass function and converted into the observable parameters (Y_{500}, θ_{500})

[4] http://www.sciops.esa.int/index.php?page=Planck_Legacy_Archive\&project=planck.

[5] A cluster is considered to be matched if there is a detection within five arcmin of its position.

using the *Planck* ESZ Y_{500}–M_{500} scaling relation (Planck Collaboration X 2011). The simulated maps consist of CMB realizations, diffuse Galactic components and instrumental noise realizations, including realistic power spectra and inter-detector correlations, from the FFP6 simulations (Planck Collaboration XII 2013; Planck Collaboration ES 2013). Residual extragalactic point sources are included by injecting, mock-detecting, masking and filling realistic multi-frequency point sources using the same process as for the real data (see Sect. 2.1).

3.2. Completeness

The completeness is the probability that a cluster with given intrinsic parameters (Y_{500}, θ_{500}) is detected given a selection threshold (here in S/N).

If the Compton-Y estimates are subject to Gaussian errors, the probability of detection per cluster follows the error function and is parameterized by $\sigma_{Yi}(\theta_{500})$, the standard deviation of pixels in the multi-frequency matched-filtered maps for a given patch i at the scale θ_{500}, the *intrinsic* Compton Y_{500}, and the detection threshold q:

$$P\left(d|Y_{500}, \sigma_{Yi}(\theta_{500}), q\right) = \frac{1}{2}\left[1 + \mathrm{erf}\left(\frac{Y_{500} - q\sigma_{Yi}(\theta_{500})}{\sqrt{2}\sigma_{Yi}(\theta_{500})}\right)\right], \quad (3)$$

where $\mathrm{erf}(x) = (2/\pi)\int_0^x \exp\left(-t^2\right) dt$ and d is the Boolean detection state.

The completeness of the catalogue, thresholded at S/N q, is expected to follow the integrated per-patch error function completeness

$$C(Y_{500}, \theta_{500}) = \sum_i f_{\mathrm{sky},i} P\Big(d|Y_{500}, \sigma_{Yi}(\theta_{500}), q\Big), \quad (4)$$

where $f_{\mathrm{sky},i}$ is the fraction of the unmasked sky in the patch i. The true completeness departs from this theoretical limit. This is due to the non-Gaussian nature of the noise dominated by the astrophysical, namely Galactic, contamination. This is also the case when the actual cluster pressure profile deviates from the GNFW used in the SZ-finder algorithms, or when the effective beams deviate from constant symmetric Gaussians, and also when the detection algorithm includes extra steps of rejection of spurious sources not formulated in Eq. 3. This is why an MCQA-based assessment of the completeness is essential to characterize the *Planck* detections.

The MonteCarlo completeness of each of the individual lists and the union catalogue are shown in Fig. 9. The `MMF` lists are consistent with one another at $\theta_{500} > 4$ arcmin, but `MMF3` is more complete at lower radii. This is due to an extra step implemented in `MMF1` that rejects as spurious the detections estimated to be point-like. The union improves upon the completeness of each of the individual catalogues, because it includes the faint real detections by one method alone. In contrast, the intersection of the lists from the three algorithms, while more robust, is markedly less complete than the union and each of the individual catalogues. The intersection and union catalogues represent the extremes of the trade-off between statistical reliability and completeness. The quantities for each of the catalogues, plus the union and intersection, are summarized in Table 2. Figure 9 shows four constant θ_{500} slices through the completeness contours for `MMF3`, comparing the MCQA-based completeness with the integrated error function completeness. At radii smaller than 6 arcmin, the MCQA-based completeness is systematically less complete, and the drop-off of the completeness function shallower, than the theoretical expectation. This effect is a consequence of the variation of intrinsic cluster profiles from the GNFW profile assumed for extraction.

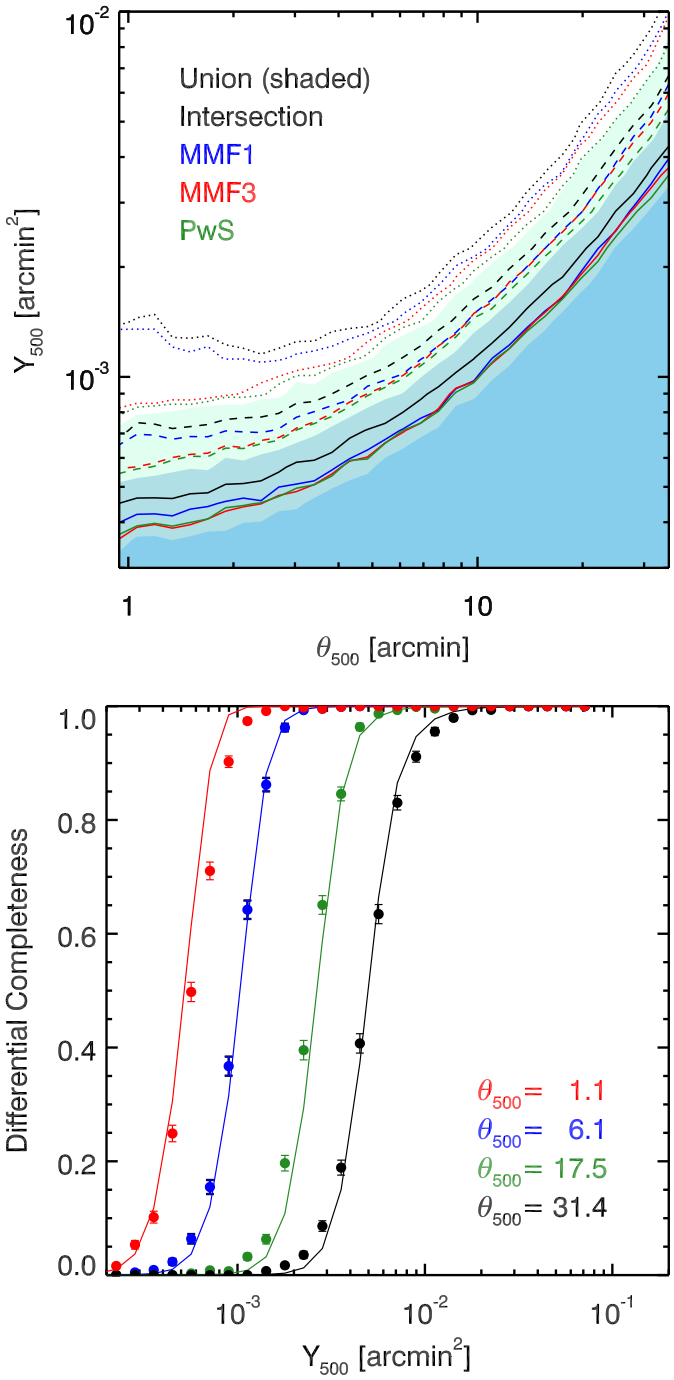

Fig. 9: *Top panel:* differential completeness as a function of (Y_{500}, θ_{500}) for each detection algorithm (`MMF1` in blue, `MMF3` in red, and `PwS` in green) and for the union (shaded area) and intersection (black) catalogues. From bottom to top, the solid, dashed, and dotted lines show 15%, 50% and 85% completeness, respectively. *Bottom panel:* slices through the MCQA-based completeness function at various θ_{500} for `MMF3` compared to the error function approximation (solid curves).

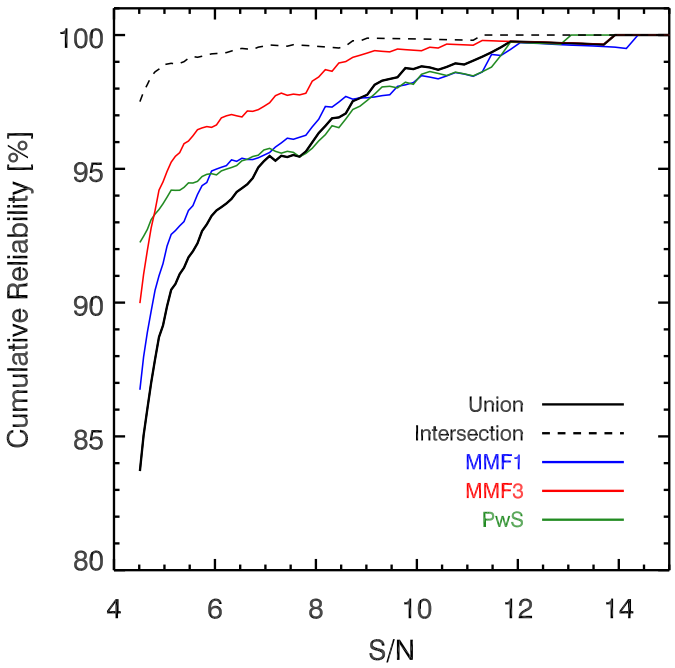

Fig. 10: Cumulative statistical reliability, defined as the fraction of sources above a given S/N associated with a "real" cluster from the simulated input catalogue.

3.3. Statistical reliability

The fraction of detections above a given S/N that are associated with a real cluster is characterized by injecting clusters into high-fidelity simulations of the *Planck* channels. Unassociated detections from these simulations define the fraction of spurious detections. We have verified that the simulations produced detection noise $\sigma_{Y_{500}}$ consistent with the real data and that the simulated detection counts match the real data.

The cumulative fraction of true clusters, as characterized by the simulations, is shown for the output of each detection algorithm and for the union catalogue in Fig. 10. The union catalogue is less pure than any of the individual lists because it includes all the lower-reliability, individual-list detections, in addition to the more robust detections made by all three SZ-finder algorithms. The union catalogue constructed over 83.7% of the sky at S/N of 4.5 is 84% pure.

The fraction of false detections is dominated by systematic foreground signals, in particular Galactic dust emission. This is illustrated in Fig. 11 by the effect of dust contamination on the cumulative reliability. We define two sky regions by the level of dust contamination: "region 1" is the low dust-contamination region outside of the *Planck* Galactic dust, and PS, mask that excludes 35% of the sky. This mask is used in Planck Collaboration XX (2013) for cosmological analysis of SZ counts. "Region 2" is the complementary region included by the smaller 15% dust mask but excluded by the 35% mask. When the larger Galactic dust mask is applied leaving 65% of the *Planck* sky survey in which to detect SZ signal, the statistical reliability increases from 84% in 83.7% of the sky to 88% in 65% of the sky. As seen in Fig. 11 upper panel, the reliability of the detections deteriorates markedly in "region 2" relative to "region 1". The noisy behaviour of the curves in Fig. 11 upper panel is due to the reduced size of sky area used in the analysis.

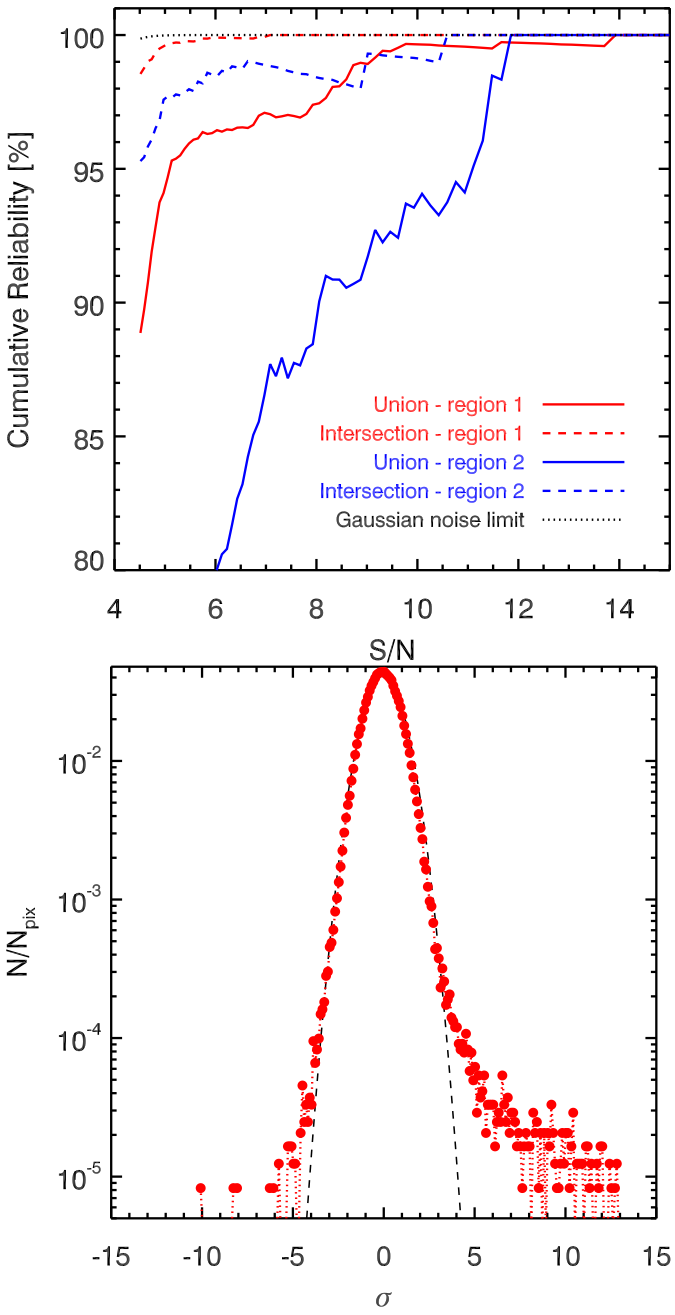

Fig. 11: *Top panel:* cumulative reliability for the union and intersection catalogues, as a function of dust contamination. Region 1 is the low-dust contamination region, being the 65% of the sky outside the Galactic dust mask, and region 2 is the complementary dustier region added to this when the smaller 15% dust mask is applied. The Gaussian noise limit is the expected reliability from purely Gaussian fluctuations. *Bottom panel:* histogram of the *y*-signal in a typical filtered patch from a null-test simulation, compared to the best-fit Gaussian (black dashed line). The distribution of *y*-noise is non-Gaussian.

In both regions, the spurious count much higher than is predicted by Gaussian fluctuations. This reflects the non-Gaussian nature of the filtered patches. The bottom panel of Fig. 11 illustrates this for a typical mid-latitude patch from a null-test simulation with no injected clusters. The patches are well ap-

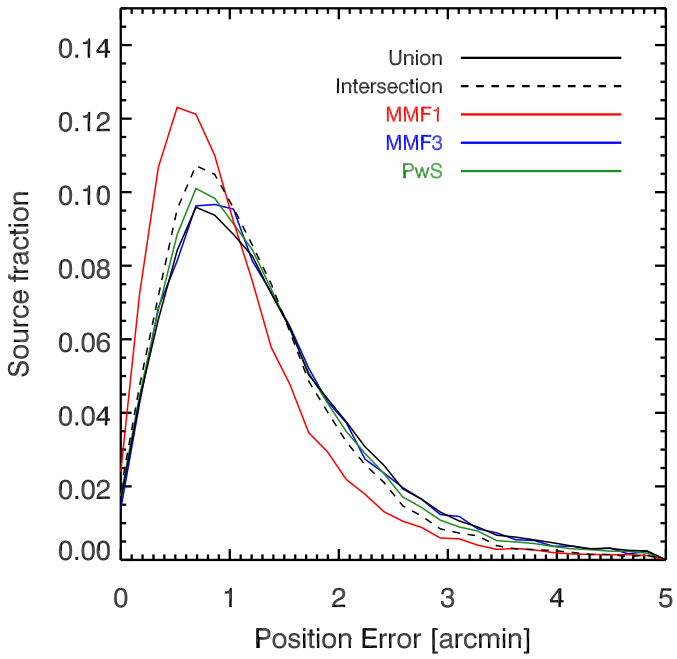

Fig. 12: Distributions of positional error for each catalogue, normalized by the total number of detections in the catalogue. By construction, the positional error is defined to be less than five arcmin.

proximated as Gaussian at deviations smaller than 3σ (consistent with the assumptions of Eq. 3), but show enhanced numbers of high significance deviations, which can translate into spurious detections.

3.4. Positional Accuracy

Positional accuracy is characterized by the radial offset between estimated and injected positions. The distribution of position error is shown in Fig. 12, for each individual list and the union catalogue. In contrast to the MMFs, which estimate the maximum-likelihood position, the PwS position estimator is the mean of the position posterior, which produces more accurate positional constraints. The union catalogue positions are taken from MMF3 if available, followed by PwS and then MMF1. Its positional estimates are hence consistent with the MMFs. The mode of the union distribution is consistent with a characteristic position error scale of half an HFI map pixel (0.86 arcmin).

3.5. Parameter Recovery

The Compton $Y_{5R_{500}}$ is characterized by comparing detected and input values for matched detections from the injection of clusters into the real data (see Fig. 13). The injection follows the scheme outlined above with one exception: input cluster parameters are drawn using the Tinker mass function and the scaling relations discussed above for reliability simulations. This ensures a realistic distribution of parameters and S/N values.

What we characterize is slightly different for each catalogue. For the MMFs, we characterize the maximum-likelihood point of the 2-D degeneracy contours provided in the individual lists. For PwS, we characterize the mean of the marginal distribution for each parameter. In each case, the 2D $(Y_{5R_{500}}, \theta_s)$ are marginalized over position. The contours are scaled for each cluster and are time consuming to compute, so we characterize the parameters from a lower-resolution grid that is better suited to Monte-Carlo analysis.[6]

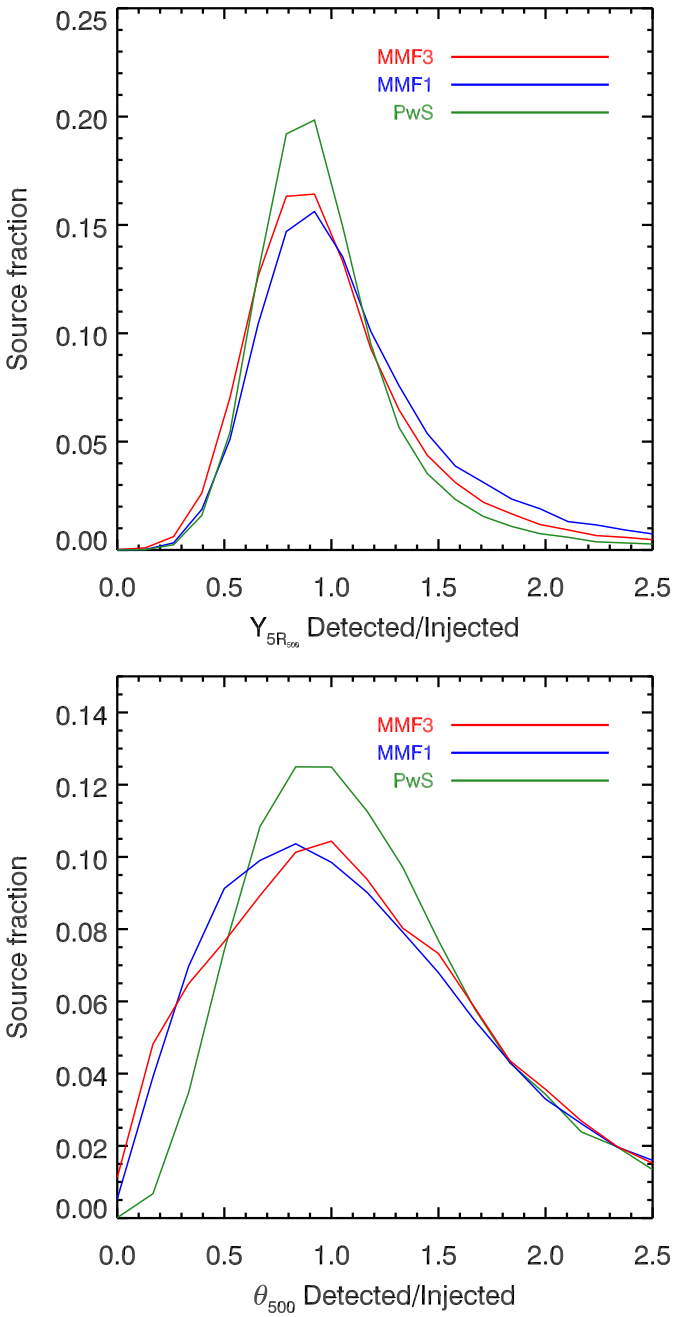

Fig. 13: Distributions of the ratio of detected over injected parameters for $Y_{5R_{500}}$ and θ_{500}.

The scatter between input and detected parameters is shown in Fig. 14 as an example for PwS. Biases are evident at both the low and high end for $Y_{5R_{500}}$. The low-flux bias is the Malmquist bias related to the S/N $\geq$ 4.5 threshold. The high-flux bias is due to a hard prior on the upper limit for cluster radius. Figure 14 also shows the distribution of the ratio of estimated over injected

[6] PwS does not resort to a low-resolution scale grid and always works at the full resolution.

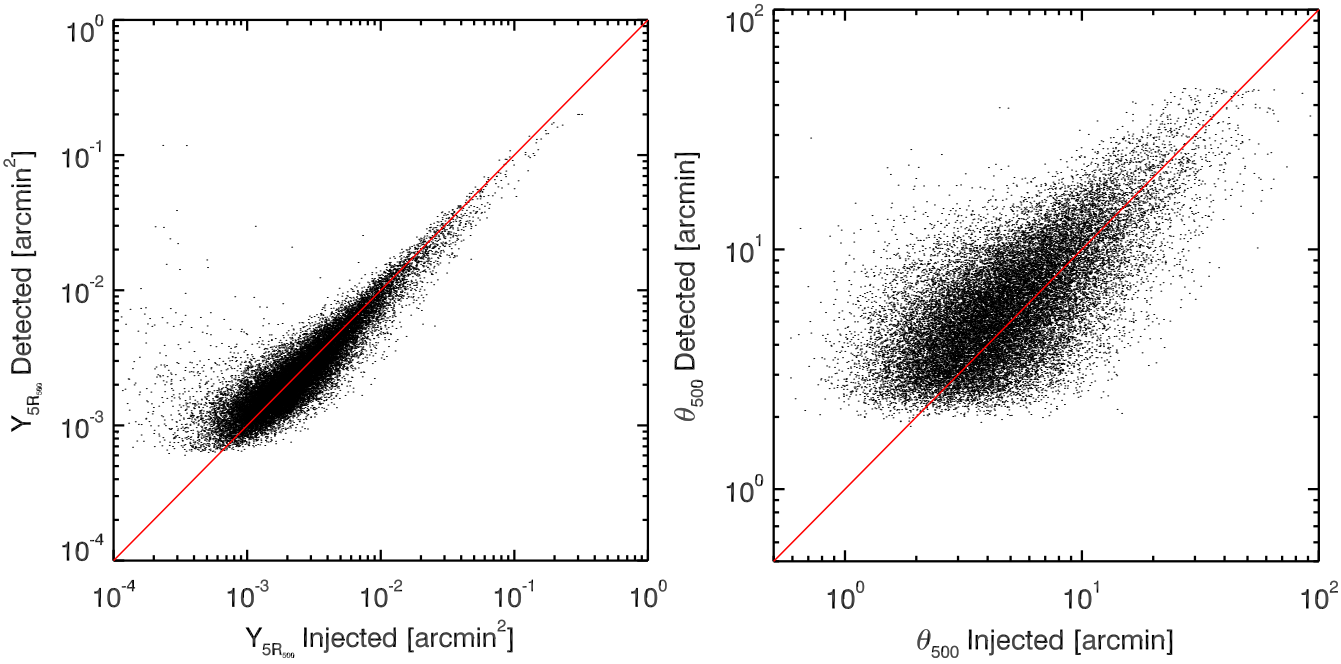

Fig. 14: Injected versus detected values of $Y_{5R_{500}}$ (left panel) and θ_{500} (right-panel), illustrated for PwS.

Table 3: Median and median absolute deviation (MAD) of the ratio of detected over injected parameters.

	$Y_{5R_{500}}$		θ_s	
	median	MAD	median	MAD
MMF1	1.09	0.39	1.17	0.70
MMF3	1.02	0.34	1.19	0.69
PwS	0.99	0.27	1.21	0.56

parameters. The median and median absolute deviation of these ratios are shown in Table 3.

The distributions for flux are positively skewed due to Malmquist bias. The median ratios of the flux recoveries are consistent with unity for MMF3 and PwS and are slightly higher for MMF1. The recovery of θ_s is biased high in the median by about 20% for each of the codes. This bias is a consequence of the intrinsic cluster profile variation and disappears when the injected profiles match the detection filter. The $Y_{5R_{500}}$ estimate by contrast is relatively unaffected by profile variation. The parameter constraints from PwS are tighter than the MMFs due to the PwS priors and the definition of the estimator as the expected value of the parameters rather than the maximum likelihood.

4. External Validation

The cluster-candidate catalogue constructed from the union of all three SZ-finder algorithms undergoes a thorough validation process that permits us to identify previously-known clusters and to assess the reliability of the *Planck* SZ candidates not associated with known clusters. In order to achieve this, we make use of the existing cluster catalogues and we also search in optical, IR, and X-ray surveys for counter-parts at the position of the *Planck* SZ sources. In Sect. 5, we present the follow-up programmes that were undertaken by the *Planck* collaboration in order to confirm and measure the redshifts of the *Planck* candidate new-clusters.

The first step of the validation of the PSZ catalogue is to identify among the *Planck* SZ candidates those associated with known clusters. For this purpose, we use existing X-ray, optical or SZ cluster catalogues. A positional matching is not sufficient to decide on the association of a *Planck* SZ source with a previously-known cluster, and a consolidation of the association is needed. For the X-ray associations, a mass proxy can be built and used to estimate the SZ flux, S/N, etc, that are compared with measured quantities for the *Planck* cluster candidates. In contrast to the X-ray clusters, optical clusters either have no reliable mass estimates or suffer from large uncertainties in the mass–richness relations. In this case, the consolidation cannot be performed uniquely through the coherence of measured versus predicted properties. It rather relies on extra information from surveys in the X-ray, optical, or IR at the *Planck* cluster-candidate positions.

In the following, we detail the search for counter-parts in optical, IR, and X-ray surveys; list the cluster catalogues used for the identification; and finally present the identification procedure followed to associate *Planck* SZ detections with bona fide clusters. In this process, we define quality flags for the association of *Planck* SZ detections with external data. We set $Q = 1$ for high-reliability associations, i.e., very clear cluster signatures, $Q = 2$ for reliable associations, and $Q = 3$ for low-reliability associations, i.e., unclear cluster signature.

4.1. Search for counter-parts of Planck detections in surveys

We made use of the *ROSAT* All Sky Survey (RASS, Voges et al. 1999), the all-sky survey with the Wide-field Infrared Survey Explorer (WISE, Wright et al. 2010), and the Sloan Digital Sky Survey (SDSS, York et al. 2000) to search for counter-parts of the *Planck* SZ detections. This information was used in two

ways. When *Planck* detections were associated with known clusters from catalogues, in particular in the optical, the counterparts in RASS, WISE, or SDSS helped in consolidating the association, increasing the confidence in the identification of *Planck* candidates with known clusters. When no association between *Planck* detections and previously-known clusters was found, the information on the counter-parts, in the surveys, of *Planck* SZ detections was used to assess the reliability of the *Planck* cluster candidates, i.e., clear or unclear cluster signatures.

4.1.1. Search in RASS data

As detailed in Planck Collaboration Int. IV (2013), the validation follow-up with *XMM-Newton* has shown the importance of the RASS data to assess the reliability of the *Planck* sources. In particular, Planck Collaboration Int. IV (2013) showed that a large fraction of *Planck* clusters are detectable in RASS maps, but this depends on the region of the sky and on the ratio Y_{500}/S_X which exhibits a large scatter (see later in Fig. 31 the case of the PSZ sources). We therefore exploit the RASS data to consolidate the identification with clusters from optical catalogues (see below Sect. 4.3.2) and to assess the reliability of the *Planck* SZ candidates.

We first perform a cross-match with the RASS bright source catalogue (BSC, Voges et al. 1999) and the faint source catalogue (FSC, Voges et al. 2000) within a five-arcmin radius of the position of each of the *Planck* SZ detections. We then perform a reanalysis of the RASS data following the methodology and prescriptions given by Böhringer et al. (2000, 2004) and Reiprich & Böhringer (2002). We compute count-rate growth curves in order to check for the extension of the signal. We estimate the source flux from both the growth curve (when adequate) and from a fixed five-arcmin aperture radius with respect to the surrounding background (after PS subtraction). We then derive the associated signal-to-noise in RASS, $(S/N)_{RASS}$. For this, we make use of the RASS hard-band, [0.5–2] keV, data that maximize the S/N of the detections. We furthermore computed the source density map of the BSC and FSC catalogues and the associated probability that a *Planck* cluster candidate will be associated with a B/FSC source within a radius of five arcmin. For the BSC, the probability of chance association is relatively low, with a median <1 %. As detailed in Planck Collaboration Int. IV (2013), the correspondence of a *Planck* SZ-candidate with a RASS-BSC source is a semi-certain association with a real cluster, whereas for the FSC catalogue the probability of chance association is larger, 5.2%.

We define a quality flag, Q_{RASS}, for the association of *Planck* candidates with RASS counter-parts using both the signal-to-noise in RASS and the association with B/FSC sources. This is of particular importance for the *Planck* candidate new clusters. Based on the results from Planck Collaboration Int. IV (2013), the quality of the association with RASS counter-parts is high, $Q_{RASS} = 1$, for *Planck* cluster candidates matching a RASS-BSC source or with $(S/N)_{RASS} \geq 2$. We find a total of 887 out of 1227 *Planck* SZ detections in this category, with mean and median signal-to-noise of 7.4 and 5.8, respectively. The quality is poor, $Q_{RASS} = 3$, for RASS counter-parts with $(S/N)_{RASS} < 0.5$ in regions of reasonable depth (quantified by the probability of chance association with FSC sources being larger than 2.5% (Planck Collaboration Int. IV 2013)).

4.1.2. Search in SDSS data

We performed a systematic search for counter-parts in the SDSS Data Release DR9 (SDSS-III Collaboration et al. 2012) at the position of all the *Planck* SZ detections. This was performed based on a cluster-finder algorithm developed by Fromenteau et al. (2013) to search for red galaxy over-densities in the SDSS galaxy catalogues.

For each associated counter-part within a five arcmin circle centred at the position of the *Planck* SZ detection, a quality criterion is defined on the basis of a fit to the luminosity function and the associated mass limit, and on the number of galaxies within five arcmin, N_{gal}, such that we have $Q_{SDSS,dat} = 1$, i.e., high quality, for cases where $N_{gal} \geq 40$ and for masses $M_{200} \geq 5.7 \times 10^{14}\,M_\odot$, $Q_{SDSS,dat} = 2$, i.e., good quality, for N_{gal} between 40 and 20 for masses between $1.5 \times 10^{14}\,M_\odot$ and $5.7 \times 10^{14}\,M_\odot$, and $Q_{SDSS,dat} = 3$ otherwise.

The cluster-finder algorithm outputs the position of the counter-part (Brightest Cluster Galaxy (BCG) and barycentre) and the estimated photometric redshift. When spectroscopic data are available for the brightest selected galaxy a spectroscopic redshift is also reported. The outputs of the cluster-finder algorithm are compared to those obtained by Li & White (2013) from different method based on the analysis of the full photometric-redshift probability distribution function (Cunha et al. 2009). In this approach, the position and redshift in the SDSS data that maximizes the S/N are considered as the best estimates for the counter-parts of the *Planck* SZ detections.

4.1.3. Search in WISE data

The Wide-field Infrared Survey Explorer (WISE, Wright et al. 2010) provides an all-sky survey at 3.4, 4.6, 12, and 22 μm (W1, W2, W3, W4) with an angular resolution of 6.1 to 12.0 arcsec in the four bands.

We search for counter-parts of the *Planck* SZ detections in the WISE source catalogue in two ways. On the one hand, we run an adaptive matched filter cluster finder developed by Aussel et al. (2013), similar to the one described by Kepner et al. (1999), using the cluster members' luminosity function of Lin et al. (2012). The background counts were determined from the neighbouring square degree in the vicinity of the *Planck* cluster candidate, excluding regions of fifteen arcmin centred on candidate positions. On the other hand, we use a method developed by Aghanim & Fromenteau (2013) based on a search for overdensities of bright ($W1 \leq 17$) and red ($W1-W2 > 0$) sources within a five-arcmin radius circle centred on the position of *Planck* detections with respect to a background computed in a fifteen-arcmin radius area.

Aghanim & Fromenteau (2013) find that a good-quality association between a *Planck* SZ-detection and a counter-part overdensity in WISE data is reached when there are at least ten galaxies above $2\,\sigma$ in the five-arcmin search region, and when the corresponding fraction of galaxies is at least 30% of the total number of galaxies retained in the fifteen-arcmin circle. Performing the search for counter-parts of an ensemble of random positions on the sky, we compute the purity of the detections, i.e., the probability of a *Planck* candidate having a real counter-part in the WISE data as opposed to a chance association. The quality criterion for the association between *Planck* detection and WISE overdensity is high, $Q_{WISE} = 1$, for a purity larger than 90%. When it lies between 90% and 80% the association of *Planck* SZ-detections and WISE overdensities is assigned a lower quality criterion $Q_{WISE} = 2$. We set the quality

of the association to $Q_{\rm WISE} = 3$, bad, when the purity is below 80%. We find 856 *Planck* SZ detections with high or good quality counter-parts in WISE data, including 658 $Q_{\rm WISE} = 1$ detections.

4.1.4. DSS images

Finally for each *Planck* cluster candidate, the second Digitized Sky Survey[7] (DSS) database was queried for a field of 5×5 arcmin^2 centred at the position of the *Planck* SZ detections in the *r* and *ir* bands. The DSS images were used for visual inspection.[8] Clusters and rich groups out to $z \simeq 0.3$ to 0.4 can easily be identified in these plates as an obvious concentration of galaxies. This qualitative information was thus used: (i) to consolidate some identifications of *Planck* SZ detections with previously-known clusters; (ii) to optimize our strategy for the follow-up observations of *Planck* candidates (see Sect. 5); and (iii) to qualitatively assess the reliability or significance of the *Planck* SZ detections.

4.2. Cluster catalogues

We now present the ensemble of catalogues that were used to identify the *Planck* SZ detections with previously-known clusters. In the case of the *ROSAT*- and SDSS-based catalogues, we have used homogenized quantities, see below, that allowed us to perform the identification with comparable association criteria, which ensures homogeneity in the output results.

MCXC meta-catalogue – For the association of *Planck* SZ candidates with previously-known X-ray clusters, we use the Meta-Catalogue of X-ray detected Clusters of galaxies (MCXC, Piffaretti et al. 2011, and reference therein) constructed from the publicly available *ROSAT* All Sky Survey-based and serendipitous cluster catalogues, as well as the *Einstein* Medium Sensitivity Survey. For each cluster in the MCXC several properties are available, including the X-ray coordinates, redshift, identifiers, and standardized luminosity, $L_{\rm X,500}$, measured within R_{500}. The MCXC compilation includes only clusters with available redshift information (thus X-ray luminosity) in the original catalogues. We updated the MCXC, considering the first release of the REFLEX-II survey (Chon & Böhringer 2012), the third public release of clusters from the MACS sample (Mann & Ebeling 2012), individual MACS cluster publications and a systematic search in NED and SIMBAD for spectroscopic redshift for clusters without this information in the *ROSAT* catalogues. This yields an ensemble of 1789 clusters with *z* and $L_{\rm X,500}$ values, adding 20 MACS clusters, 21 REFLEX-II clusters and 5 SGP clusters to the MCXC. For these clusters, the expected Compton-parameter, $Y_{500}^{L_{\rm X}}$, and size, $\theta_{500}^{L_{\rm X}}$, are estimated combining the M_{500}–$L_{\rm X,500}$ relation of Pratt et al. (2009) and the M_{500}–Y_{500} relation given by Arnaud et al. (2010). The expected S/N ratio, $({\rm S/N})^{L_{\rm X}}$, is computed taking into account the noise within $\theta_{500}^{L_{\rm X}}$ at the cluster location. We furthermore supplement the updated MCXC with 74 clusters from *ROSAT* catalogues without redshift information and 43 unpublished MACS clusters observed by *XMM-Newton* or *Chandra*. For these 117 objects, only centroid positions are available. Finally, we considered the published catalogues from *XMM-Newton* serendipitous cluster surveys with available redshifts, the XCS catalogue (Mehrtens et al. 2012), the 2XMMi/SDSS catalogue (Takey et al. 2011) and the XDCP catalogue (Fassbender et al. 2011). However, these catalogues mostly extend the MCXC to lower masses and only two *Planck* candidates were found to be associated with these new clusters.

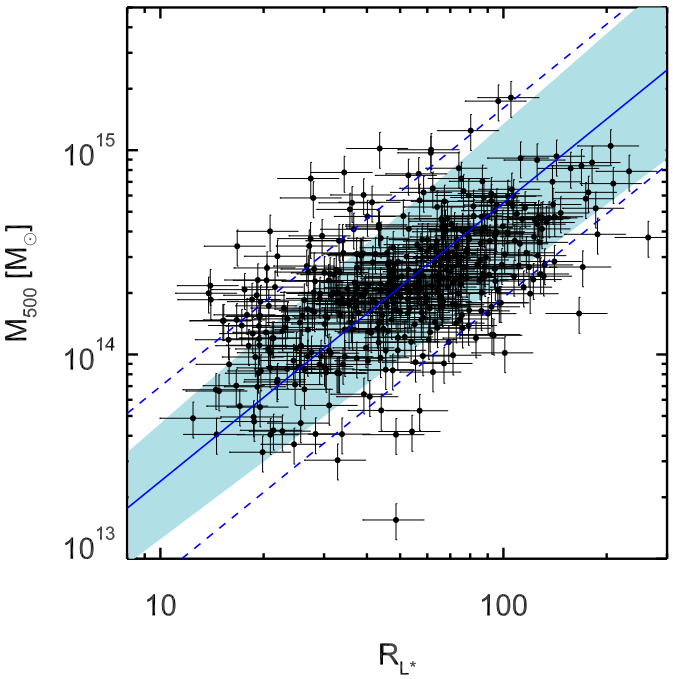

Fig. 15: Mass to richness scaling relation, M_{500}–$R_{\rm L^*}$, for the 444 MCXC clusters included in the WHL12 catalogue (Wen et al. 2012). The best-fit relation, from BCES fit, is given by the solid blue line. We adopted 15% uncertainties on the MCXC masses as prescribed in Piffaretti et al. (2011). As no uncertainty is provided for the WHL12's richness, we arbitrarily assumed a 20% uncertainty for all richness values. The blue shaded area shows the associated errors on the best-fit, while the dashed line marks the intrinsic scatter.

Optical-cluster catalogues – The identification of the *Planck* SZ candidates with clusters known in the optical is based on the Abell (Abell 1958) and the Zwicky (Zwicky et al. 1961) cluster catalogues. Furthermore, we have used four different catalogues of clusters based on the Sloan Digital Sky Survey (SDSS, York et al. 2000) data: (1) the MaxBCG catalogue (13, 823 objects, Koester et al. 2007); (2) the GMBCG catalogue (55, 424 objects, Hao et al. 2010); (3) the AMF catalogue (69, 173 objects, Szabo et al. 2011); and (4) the WHL12 catalogue (132, 684 objects, Wen et al. 2012). We refer the reader to Wen et al. (2012) for a comparison of the existing SDSS-based catalogues of clusters and groups. Each of the SDSS-based catalogues provides an estimated richness; we first start by homogenizing the richness estimates to that of WHL12. For each catalogue, we compute the median ratio of WHL12's richness to that of the considered catalogue over its intersection with WHL12's. We then renormalize the individual richness by the corresponding ratio. The correcting factors applied to the richness estimators[9] are respectively 1.52, 1.75, and 0.74 for MaxBCG, GMBCG, and AMF, obtained

[7] http://stdatu.stsci.edu/dss/.

[8] Images from the RASS, SDSS and WISE surveys at the position of the *Planck* SZ detections were also inspected.

[9] Field NGALS_R200 for MaxBCG, GM_SCALED_NGALS for GMBCG and LAM200 for AMF.

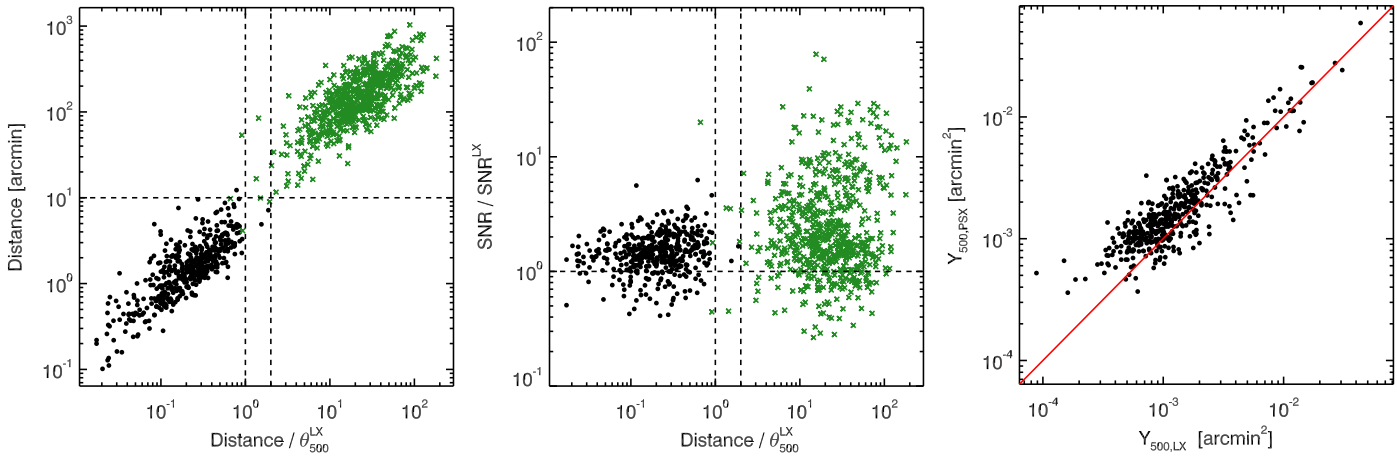

Fig. 16: Identification of the *Planck* cluster candidates with X-ray clusters from the MCXC catalogue. Black points are candidates firmly identified with MCXC clusters, while green points are candidates with no association. *Left panel:* distance of the *Planck* position to the position of the closest MCXC cluster as a function of the distance normalized to the cluster size $\theta_{500}^{L_X}$. *Middle panel:* S/N normalized to the expected value as a function of normalized distance. *Right panel:* SZ flux, $Y_{500,PSX}$, re-extracted fixing the position and size to the X-ray value, as a function of expected values. The red line is the equality line. In all panels, $Y_{500}^{L_X}$, and $\theta_{500}^{L_X}$ are estimated from the cluster X-ray luminosity used as mass proxy (see text).

from 7627, 17245, and 1358 common clusters.[10] The richness is then related to the halo mass, M_{500}, by extending the Wen et al. (2012) richness–mass relation provided on about 40 clusters[11] to 444 MCXC clusters, with masses estimated from the X-ray luminosities. The data points and the best-fit scaling relation are presented in Fig. 15. The derived M_{500}–$R_{L^\star}$ and $L_{X,200}$–$R_{L^\star}$ relations are compatible with the findings of Wen et al. (2012). We find $\log(M_{500}/10^{14}\,M_\odot) = (-2.00\pm0.17)+(1.37\pm0.10)\times\log R_{L^\star}$. The relation presents a large intrinsic log-scatter, $\sigma_{int} = 0.27 \pm 0.02$, hampering any accurate estimation of the cluster mass. This is further illustrated by the richest clusters with $R_{L^\star} > 110$ having MCXC masses systematically below the best-fit M_{200}–$R_{L^\star}$ relation (although within the 1σ intrinsic scatter).

SZ catalogues – At millimetre wavelengths, we cross-check the *Planck* SZ catalogue with the recent ACT and SPT samples (Menanteau et al. 2010; Vanderlinde et al. 2010; Williamson et al. 2011), including the most recent data that increased the number of SZ detections and updated the redshift estimates for the clusters (Reichardt et al. 2013; Hasselfield et al. 2013). We have furthermore identified the *Planck* SZ detections associated with previous SZ observations of galaxy clusters from the literature. We used a compilation of SZ observations conducted with the numerous experiments developed during the last 30 years (Ryle, OVRO, BIMA, MITO, Nobeyama, SZA, APEX-SZ, AMI, Diabolo, Suzie, Ryle, AMIBA, ACBAR, etc.).

4.3. Identification with previously-known clusters

4.3.1. Identification with X-ray clusters

The *Planck* SZ candidates are cross-checked against previously-known X-ray clusters from the updated version of the MCXC. For a given *Planck* candidate-cluster we identify the closest MCXC cluster.[12] The reliability of the association is assessed based on distance, D, compared to the cluster size and on the measured Y_{500} and S/N values compared with the expected values (see Fig. 16). Two clouds of points stand out in the scatter plot of absolute versus relative distance, $D/\theta_{500}^{L_X}$ (Fig. 16, left panel). They correspond to two clouds in the scatter plot of the measured over expected S/N ratio versus $D/\theta_{500}^{L_X}$ (Fig. 16, middle panel).

The association process follows three main steps. First, we provisionally assign an X-ray identification flag based on distance:

- $Q_X = 3$ if $D > 2\theta_{500}^{L_X}$ and $D > 10$ arcmin. Those are considered as definitively not associated with an MCXC cluster in view of *Planck* positional accuracy and cluster extent.
- $Q_X = 1$ if $D < \theta_{500}^{L_X}$ and $D < 10$ arcmin. Those are associated with an MCXC cluster.
- $Q_X = 2$ otherwise, corresponding to uncertain associations.

We then refine the classification. In the $Q_X = 1$ category, we identify outliers in terms of the ratio of measured to expected S/N and Y_{500}, taking into account the scatter and the size–flux degeneracy. Their flags are changed to $Q_X = 2$. In some cases, two distinct $Q_X > 1$ candidates are associated with the same MCXC cluster. The lowest S/N detection is flagged as $Q_X = 2$.

In the final step, we consolidate the status of $Q_X < 3$ candidates. We first re-extract the SZ signal at the X-ray position, both leaving the size free and fixing it at the X-ray value. The Y_{500} obtained with the cluster and size fixed to the X-ray values are compared to the expected values, $Y_{500}^{L_X}$, in the right panel of Fig. 16. For bona fide association, we expect no major change of Y_{500} and S/N, with, on average, a better agreement with the expected Y_{500} value and some decrease of S/N.

- For $Q_X = 1$ candidates, the re-extracted Y_{500} and S/N values are compared to both blind and expected values (as a function of distance, S/N, etc.) to identify potential problematic

[10] We considered the associations of clusters with positions matching within 6 arcsec radius and with $\Delta z \leq 0.05$ (typical uncertainty for photometric redshifts in SDSS).

[11] Their M_{200} are taken from the literature either from weak lensing or X-ray measurements (Wen et al. 2010).

[12] The information of the second closest is also kept to identify potential confusion or duplicate associations.

cases, e.g., important decrease of S/N or outliers in terms of measured-over-expected Y_{500} ratio. We found only one such case, whose flag is changed to $Q_X = 2$. The identification of other candidates is considered as consolidated, with definitive flag $Q_X = 1$.
– We then examine the $Q_X = 2$ candidates. We consider the re-extracted Y_{500} and S/N, but also perform a visual inspection of the SZ maps and spectra and ancillary data, including RASS and DSS images. The $Q_X = 2$ candidates were identified as clearly identified as multiple detections of extended clusters or duplicate detections of the same clusters by different methods that were not merged (the former are flagged as false detections, the latter are merged with the corresponding candidate in the union catalogue) or not associated (e.g., SZ sources clearly distinct from the MCXC clusters with no significant re-extracted signal at the cluster position and size).

Finally, for MCXC clusters without redshift and luminosity information, the association was only based on distance, setting $D_X < 5$ arcmin, and the consolidated based on visual inspection of SZ, RASS and DSS images and other ancillary information. Two cases were found to be a mis-identification. The SZ candidate was closer by chance to a faint XCS cluster, in the vicinity of the real counter-part (another MCXC cluster and an Abell cluster, respectively).

4.3.2. Identification with optical clusters

The *Planck* SZ candidates are associated with known clusters from optical catalogues (Abell, Zwicky, SDSS-based catalogues) on the basis of distance with a positional matching within a search radius set to five arcmin. The consolidation of the association was performed using the RASS information as described below, which allows us to mitigate the chance associations with poor optical galaxy groups and clusters.

SDSS-based catalogues – We have considered the four catalogues listed in Sect. 4.2. We define a quality criterion for the association, Q_{SDSS}, in terms of cluster richness as a proxy of the cluster mass (see for instance Johnston et al. 2007; Rozo et al. 2009). We set the quality criterion, Q_{SDSS}, to 3 for low reliability, to 2 for good reliability and to 1 for high reliability. The corresponding richness thresholds are 110 and 70 for $Q_{SDSS} = 1/2/3$, respectively. The corresponding estimated masses (given the M_{500}–$R_{L^\star}$ relation) are $M_{500} > 6.5 \times 10^{14}\,M_\odot$ and $M_{500} > 3.5 \times 10^{14}\,M_\odot$. However due to the large scatter and associated uncertainty in the mass estimate from the mass–richness relation, we consolidate the association of the *Planck* candidates with SDSS clusters by combining the Q_{SDSS} with the RASS signal at the *Planck*-candidate position (see Sect. 4.1.1). In practice, only associations with $Q_{SDSS} = 1$ or 2 and a signal-to-noise, measured at the *Planck* position in an aperture of five arcmin in the RASS survey, $(S/N)_{RASS} \geq 1$ are retained as firm identifications. We stress that our choice of richness thresholds is relatively conservative on average. Indeed, our $Q_{SDSS} = 1$ and 2 matched candidates are found with high $(S/N)_{RASS}$ values as shown in Fig. 17, with mean $(S/N)_{RASS} = 7.1$ and 6.6 and median $(S/N)_{RASS} = 5.9$ and 5.4 for $Q_{SDSS} = 1$ and 2 matches, respectively.

Abell and Zwicky catalogues – The *Planck* candidates are associated with Abell and Zwicky clusters on the basis of a positional matching within five arcmin. In the present case, we do not make use of any richness information in order to consolidate the association. We rather use here solely the RASS signal, $(S/N)_{RASS}$, at the SZ-candidate position. *Planck*-candidates associated with Abell or Zwicky clusters and with $(S/N)_{RASS} \geq 1$ are retained as firmly identified. For associations with $(S/N)_{RASS} < 1$, we decided on a firm identification only after checking the status of the counter-part in the WISE data and performing a visual inspection of the SZ signal and of the images from ancillary data, including DSS images.

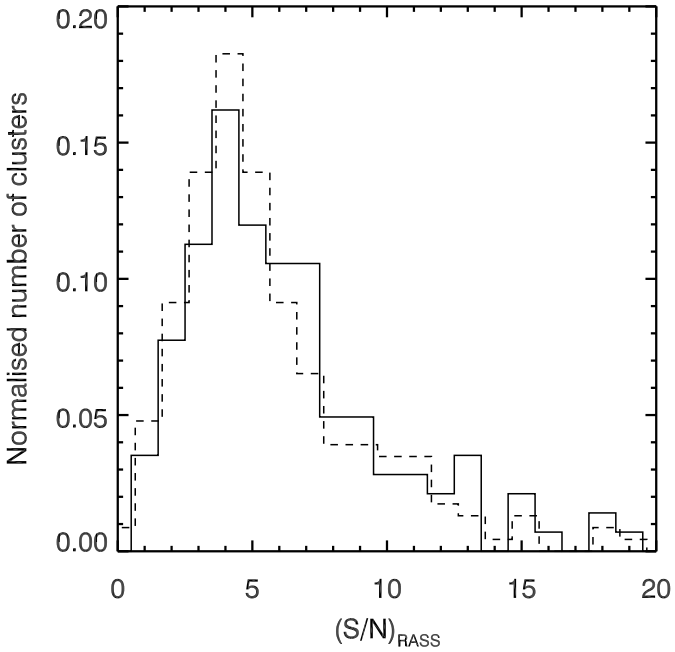

Fig. 17: Normalized distribution of the signal-to-noise in RASS survey at the position of *Planck* SZ detections with SDSS richness-based quality $Q_{SDSS} = 1$ (solid line) and $Q_{SDSS} = 2$ (dashed line).

4.3.3. Identification with SZ clusters

The association with known SZ clusters was performed within a five-arcmin radius. A visual inspection of the ancillary data and an *a posteriori* check of the RASS signal at the position of the *Planck* candidates associated with clusters from SZ catalogues is performed. It confirms that the values of $(S/N)_{RASS}$, when the coverage is significant, are high with an average value of 5.4.

4.3.4. Identifications from NED and SIMBAD

The information provided from querying NED and SIMBAD databases is mainly redundant with cross-checks with cluster catalogues. However, it lets us avoid missing a few associations. We therefore performed a systematic query in SIMBAD and NED with an adopted search radius set to five arcmin. Similarly to the association with clusters in optical catalogues, the positional association is consolidated using the results of the search in RASS data. Furthermore, the *Planck*-candidates solely matching NED or SIMBAD entries were inspected and the identification was confirmed or discarded using the information from WISE counter-parts and the DSS images.

Table 4: List of the main observing facilities used for the confirmation of the *Planck* newly-discovered clusters, and for the measurement of their redshifts.

Site	Telescope	Aperture (m)	Instrument	Filters	Redshift
...	XMM-Newton		EPIC/MOS & PN	...	Fe K
La Palma	NOT	2.56	ALFOSC	...	spec
La Palma	INT	2.5	WFC	*griz*	phot
La Palma	GTC	10.4	OSIRIS	...	spec
La Palma	TNG	3.5	DOLORES	...	spec
La Palma	WHT	4.2	ACAM	*griz*	phot
La Silla	NTT	3.7	EFOSC2	...	spec
La Silla	MPG/ESO 2.2m	2.2	WFI	VRI	phot
Mullard Radio Ast. Obs.	AMI	3.7 and 13	SA & LA	13.5 to 18 GHz	...
Tenerife	IAC80	0.82	CAMELOT	*griz*	phot
TUBITAK Nat. Obs.	RTT	1.5	TFOSC	*gri*	spec,phot

5. Follow-up programme for confirmation of *Planck* candidates

We have undertaken, since Spring 2010, an extensive follow-up programme in order to perform a cluster-by-cluster confirmation of the *Planck* cluster candidates and obtain a measurement of their redshifts. A total of 276 *Planck* candidates, selected down to S/N = 4 from intermediate versions of the *Planck* SZ catalogue, were observed in pursuit of their redshift measurement. We have constructed our strategy for the selection of the *Planck* targets primarily on the successful results of the series of follow-up observations in X-rays based on Director's Discretionary Time on the *XMM-Newton* observatory (Planck Collaboration IX 2011; Planck Collaboration Int. I 2012; Planck Collaboration Int. IV 2013). Snapshot observations, sufficient to detect extended X-ray emission associated with *Planck* clusters and to estimate redshifts from the Fe line for the brightest clusters, were conducted sampling the SZ detections down to S/N = 4. These observations allowed us to better understand the SZ signal measured by *Planck* and hence to refine the criteria to select targets, especially for further optical follow-up.

We have engaged numerous campaigns on optical facilities, which now constitute our main means of confirmation of *Planck* SZ detections. *Planck* candidates with low-quality DSS images or without SDSS information, or low $(S/N)_{RASS}$, were primarily sent for deeper multi-band imaging observations. They were followed-up to the depth needed for the confirmation, i.e., finding an optical counter-part, and for the determination of a photometric redshift. Candidates with galaxy concentrations in DSS or with counter-parts in SDSS, and/or with high $(S/N)_{RASS}$, were preferentially sent for spectroscopic confirmation. The priority being to confirm the clusters and to secure the largest number of robust redshifts, no systematic spectroscopic confirmation of photometric redshifts was performed for low-redshift clusters ($z_{phot} < 0.4$). For higher-redshift clusters, spectroscopic confirmation of the photometric redshifts is more crucial. As a result, we have made use of telescopes of different sizes, from 1-m to 10-m class telescopes, optimizing the selection of targets sent to the different observatories (Table 4 gives the list of the main telescopes). Eight- and ten-metre class telescopes, e.g., GTC, GEMINI and VLT, were used to spectroscopically confirm redshifts above 0.5 for already confirmed clusters.

Our efforts to confirm the *Planck* cluster candidates, measure redshifts, and characterize cluster physical properties relies on ongoing follow-up of a large number of cluster candidates in the optical (ENO, RTT150, WFI), in the infrared (Spitzer[13]) and at SZ wavelengths (Arcminute Microkelvin Imager, AMI). The output of the confirmation and redshift measurements from the observing campaigns is summarized in Sect. 6.2. Companion publications, in preparation, will detail the observing campaigns and their results.

5.1. XMM-Newton observatory

The X-ray validation follow-up programme of 500 ks observations undertaken in *XMM-Newton* DDT is detailed in Planck Collaboration IX (2011), Planck Collaboration Int. I (2012), and Planck Collaboration Int. IV (2013). It consisted of observing 51 *Planck* targets and led to the confirmation of 43 *Planck* cluster candidates, two triple systems and four double systems. There were eight false candidates. This follow-up programme has constituted the backbone of the *Planck* cluster confirmation and most importantly has allowed us to better understand the SZ signal measured by *Planck* and thus to better master the criteria for confirmation (or pre-confirmation) of the *Planck* cluster candidates. By providing us with the physical properties and redshift estimates of the confirmed clusters, it has furthermore given us a first view on the physical characteristics of the newly discovered *Planck* clusters. Snapshot observations (around 10 ks) of the *Planck* candidates took place between May 2010 and October 2011. All the results from the four observing campaigns were published in Planck Collaboration IX (2011), Planck Collaboration Int. I (2012), and Planck Collaboration Int. IV (2013). Calibrated event lists were produced with v11.0 of *XMM-Newton*-SAS, and used to derive redshifts and global physical parameters for the confirmed clusters (Planck Collaboration IX 2011). The redshifts were estimated by fitting an absorbed redshifted thermal plasma model to the spectrum extracted within a circular region corresponding to the maximum X-ray detection significance. Most of the redshifts were confirmed using optical observations. Additional observations at VLT were conducted to confirm spectroscopically the highest redshifts.[14]

[13] Under Spitzer programs 80162 and 90233.

[14] Observations are conducted under programme 090A-0925.

5.2. Optical observation in the Northern hemisphere

5.2.1. ENO telescopes

In total 64 cluster candidates from *Planck* were observed at European Northern Observatory (ENO[15]) telescopes, both for imaging (at IAC80, INT and WHT) and spectroscopy (at NOT, GTC, INT and TNG), between June 2010 and January 2013.[16] The aims of these observations were the confirmation, photometric redshift measurement, and spectroscopic confirmation of redshifts above $z = 0.3$.

INT, WHT and IAC80 – The optical imaging observations were taken either with the Wide-Field Camera (WFC) on the 2.5-m Isaac Newton Telescope (INT), the auxiliary-port camera (ACAM) at the 4.2-m William-Herschel Telescope (WHT), or with CAMELOT, the optical camera at the 0.82-m telescope (IAC80). The targets were observed in the Sloan *gri* filters. For the majority of fields, either Sloan *z* or Gunn *Z* images are also available. Images were reduced using the publicly-available software `Iraf` and `Sextractor` (Bertin & Arnouts 1996). The data reduction included all standard steps, i.e., bias and flat field corrections, astrometric and photometric calibrations. The photometric calibration is based either on standard star observations or, if available, on data from the SDSS. Finally, all magnitudes were corrected for interstellar extinction, based on the dust maps by Schlegel et al. (1998). We obtained photometric redshifts using the BPZ code (Benítez 2000), using a prior based on SDSS data, and fitting a set of galaxy templates. The BPZ code provides the Bayesian posterior probability distribution function for the redshift of each object, which is later used in the process of cluster identification. The identification of the galaxy overdensity located near the *Planck* positions and the estimate of the photometric redshifts of the associated clusters were performed using a modified version of the cluster-algorithm described in Sect. 4.1.2.

GTC and TNG – Spectroscopic observations were performed using the 10-m Gran Telescopio Canarias (GTC) telescope and the 3.6-m Telescopio Nazionale Galileo (TNG) telescope. The OSIRIS spectrograph at GTC was used in long-slit mode to observe a total of eight targets with two slit positions per candidate. We used the R500R grism and a binning 2×1, which provides a resolution $R = 300$ with a slit width 1 arcsec, and a wavelength coverage 4800–10000 Å. We retrieved three exposures of 1200 s each. The final spectra present a S/N of about 20 in galaxies with $r' = 20$ mag. We used the DOLORES multi-object spectrograph (MOS) at TNG to observe 9 candidates. The masks were designed to contain more than 30 slitlets, 1.5 arcsec width, placed within an area about 6 arcmin ×8 arcmin in order to cover the target field. We used the LR-B grism, which provides a dispersion of 2.7 Å/pixel, and a wavelength coverage between 4000 and 8000 Å. We carried out three acquisitions of 1800 s each and obtained spectra with S/N $\simeq$ 15 in galaxies with $r' = 20$ mag using a total integration time of 5400 s.

Nordic Optical Telescope (NOT) – Spectroscopic redshift measurements were obtained using the Andalucia Faint Object Spectrograph and Camera (ALFOSC) at the NOT.[17] Most targets were observed in MOS mode, targeting typically ten to fifteen galaxies per ALFOSC field (covering 6.4×6.4 arcmin^2, with an image scale of 0.188 arcsec/pixel). One or two unfiltered 300s pre-imaging exposures were obtained per candidate cluster, in addition to a single 300s exposure in each of the SDSS *g*-and *i* bands. The de-biased and flat field calibrated pre-imaging data were used to select spectroscopy targets. The final mask design[18] was carved out using custom software, generating slits of fixed width 1.5 arcsec and of length typically 15 arcsec. Grism No. 5 of ALFOSC was used, covering a wavelength range 5000 – 10250 Å with a resolution of about $R = 400$ and dispersion 3.1 Å/pixel. Redwards of 7200 Å strong fringing is present in the ALFOSC CCD. It was effectively suppressed using dither pattern alternating the placement of the spectroscopy targets between these sets of slits.

In addition to the MOS observations, spectroscopic observations in single-slit mode were conducted for some *Planck* candidates. For these observations, a long slit covering the entire 6.4 arcmin length of the ALFOSC field and a width of 1.3 arcsec was employed, with the same grism and wavelength coverage as for the MOS observations. The field angle was rotated to place the long slit over multiple targets, to include the apparent BCG as well as two to three other bright cluster galaxies within the ALFOSC field.

5.2.2. RTT150

A total of 88 *Planck* cluster candidates were followed up with the Russian Turkish Telescope (RTT150[19]) from July 2011 to December 2012 within the Russian quota of observational time. In total, about 50 dark nights, provided by Kazan Federal University and Space Research Institute (IKI, Moscow), were used for these observations. Direct images and spectroscopic redshift measurements were obtained using TÜBİTAK Faint Object Spectrograph and Camera (TFOSC[20]), similar in layout to ALFOSC at NOT (see above) and to other instruments of this series.

The TFOSC CCD detector cover a 13.3×13.3 arcmin^2 area with 0.39 arcsec per pixel image scale. Direct images of cluster candidates were obtained in Sloan *gri* filters, in series of 600s exposures with small ($\approx$ 10–30 arcsec) shifts of the telescope pointing direction between the exposures. All standard CCD calibrations were applied using `Iraf` software, individual images in each filter were then aligned and combined. The total of 1800 s exposure time in each filter was typically obtained for each field, longer exposures were used for more distant cluster candidates. Deep multi-filter observations were obtained for all candidates, except those unambiguously detected in SDSS. With these data, galaxy clusters can be efficiently identified at redshifts up to $z \approx 1$.

Galaxy clusters were identified as enhancements of surface number density of galaxies with similar colours. Cluster red sequences were then identified in the colour–magnitude diagram

[15] ENO: http://www.iac.es/eno.php?lang=en.

[16] The observations were obtained as part of proposals for the Spanish CAT time (semesters 2010A, 2010B, 2011A, 2011B, 2012A and 2012B), and an *International Time Programme (ITP)*, accepted by the International Scientific Committee of the Roque de los Muchachos (ORM, La Palma) and Teide (OT, Tenerife) observatories (reference ITP12_2).

[17] The observing runs took place on June 28 - July 3, 2011, January 20-25, 2012, July 16-21, 2012 and January 9-14, 2013.

[18] The MOS masks were cut at the Niels Bohr Institute, Copenhagen University.

[19] http://hea.iki.rssi.ru/rtt150/en/index.php.

[20] http://hea.iki.rssi.ru/rtt150/en/index.php?page=tfosc.

of galaxies near the optical centre of the identified cluster. The detected red sequence was used to identify the BCG and cluster member galaxies. Using the measured red-sequence colour photometric redshift estimates were obtained, which were initially calibrated using the data on optical photometry for galaxy clusters from the 400SD X-ray galaxy cluster survey (Burenin et al. 2007).

For spectroscopy we used the long-slit mode of the instrument with grism No. 15, which covers the 3900–9100 Å wavelength range with ≈ 12 Å resolution when a slit of 1.8 arcsec width is used. Galaxy redshifts were measured through the cross-correlation of obtained spectra with a template spectrum of an elliptical galaxy. Spectroscopic redshifts were typically obtained for the spectra of a few member galaxies, including the BCG, selected from their red sequence in the imaging observations. These data allow us to efficiently measure spectroscopic redshifts for clusters up to $z \approx 0.4$. For the highest-redshift clusters, complementary spectroscopic observations were performed with the BTA 6-m telescope of SAO RAS using SCORPIO focal reducer and spectrometer (Afanasiev & Moiseev 2005).

5.3. Optical observation in the Southern hemisphere

5.3.1. MPG/ESO 2.2-m Telescope

Optical imaging of 94 *Planck* cluster candidates in the Southern hemisphere was performed under MPG programmes at the MPG/ESO 2.2-m telescope using the Wide-Field Imager (WFI).[21] The WFI detector is a mosaic of 8 2k × 4k CCDs, covering a total area of 33 arcmin ×34 arcmin on the sky, with an image scale of 0.238 arcsec/pixel. Each field was observed in the *V*-, *R*-, and *I*-bands with a default exposure time of 1800s (with five dithered sub-exposures) per passband. The basic data calibration, including de-biasing and flat-field frame calibration, followed standard techniques. The individual exposures were re-registered and WCS calibrated using the USNO-B1 catalogue as an astrometric reference before being stacked into a combined frame for each filter, covering the entire WFI field. Photometric redshifts of the observed clusters were then determined from an algorithm that searches for a spatial galaxy overdensity located near the position of the SZ cluster candidate that also corresponds to an overdensity in $V - R$ versus $R - I$ colour–colour space. The median colour of galaxies located in this overdensity was then compared to predicted colours of early-type galaxies at different redshifts by convolving a redshifted elliptical galaxy spectral energy distribution template with the combined filter+telescope+detector response function.

5.3.2. New Technology Telescope (NTT)

Observations[22] were conducted at the 3.5-m NTT at the ESO observatory at La Silla to measure spectroscopic redshifts of 33 *Planck* clusters with the EFOSC2 instrument in the MOS mode. A clear BCG was identified in the clusters in pre-imaging data, and besides the BCG a redshift was measured for at least one other member of the cluster. In the following a brief outline of the observations and the data reduction are given (see Chon & Böhringer 2012, for details).

Each field of the *Planck* target candidates was optically imaged in Gunn *r* band for target selection and mask making. The imaging resolution is 0.12×0.12 arcsec^2, and the field of view is 4.1×4.1 arcmin^2 for both imaging and spectroscopic observations. When necessary, the field was rotated to optimize target selection. We used the grism that covers the wavelength range between 4085 Å and 7520 Å, with 1.68 Å per pixel at resolution 13.65 Å per arcsec. We typically applied 10 to 15 slitlets per field with a fixed width of 1.5 arcsec for the MOS and of 2.0 arcsec for the long-slit observations. Including at least three bright objects, preferably stars, to orient the field, the slitlets were allocated to the candidate member galaxies. The exposure times for the clusters range from 3600s to 10800s.

The data were reduced with the standard reduction pipeline of `Iraf`. The redshifts from the emission lines were determined separately after correlation with the passive galaxy templates. We use the `rvsao` package, which applies the cross-correlation technique to the input templates of galaxy spectra to measure the object redshift. The REFLEX templates were used for this analysis, which include 17 galaxy and stellar templates. We confirmed a spectroscopic cluster detection if at least three galaxies have their R-value greater than 5, and lie within ± 3000km/s of the mean velocity of the cluster members. We then took the median of those galaxy redshifts as the cluster redshift. For the long-slit observation, the cluster was confirmed with the redshift of the BCG and another galaxy at similar redshift within the aforementioned criteria.

5.4. Observations in the SZ domain with AMI

An ensemble of 60 *Planck* blind SZ candidates, spanning a range of S/N between 4 and 9 and meeting the Arcminute Microkelvin Imager (AMI) observability criteria, was observed with AMI. The goal of this programme was to confirm *Planck* cluster candidates through higher-resolution SZ measurements with AMI and to refine the position of confirmed clusters in order to optimize the subsequent optical follow-up observations aiming at redshift measurement. AMI comprises of two arrays: the Small Array (SA); and the Large Array (LA). Further details of the instrument are given in AMI Consortium et al. (2008). Observations carried out with the SA provide information that is well coupled to the angular scales of the SZ effect in clusters, whereas snapshot observations obtained with the LA provide information on the discrete radio-source environment. The latter allowed us to detect the presence of nearby, bright radio sources, helping in further selecting the targets for observation with the SA. Details of the AMI data reduction pipeline and mapping are described in Planck and AMI Collaborations (2013).

6. Results of the validation and follow-up

The external validation allows us to identify *Planck* SZ detections with previously-known clusters and to assemble crucial information on the identified clusters such as their redshifts. The validation steps corresponding to the association with known clusters were performed following a chosen hierarchy: X-ray clusters from the updated MCXC meta-catalogue; then optical clusters from Abell and Zwicky catalogues; then optical clusters from the SDSS-based catalogues; followed by SZ clusters from SPT and ACT samples; and finally clusters from NED and

[21] Based on observations under MPG programmes 086.A-9001, 087.A- 9003, 088.A-9003, 089.A-9010, and 090.A-9010. The observations were conducted during the periods of November 27 - December 3, 2010, March 8-19, May 21 - June 3, and November 30 - December 4, 2011, December 30, 2011 - January 7, 2012, June 10-18, 2012, and January 6-13 2013.

[22] The observations were performed during three spectroscopic observing campaigns, 087.A-0740, 088.A-0268 and 089.A-0452.

Table 5: Summary of the external validation and confirmation from follow-up observations. In each category, the number represents the total number of *Planck* candidates identified exclusively with X-ray, optical, or SZ clusters. The category X-ray clusters covers identifications from the updated MCXC meta-catalogue. The category optical clusters covers identification from the Abell, Zwicky, and SDSS-based catalogues only. The category SZ clusters covers identification from SPT and ACT catalogues only. Confirmations from follow-up do not cover the observations performed by the *Planck* collaboration to measure the missing redshifts of known clusters. Confirmation from archival data covers X-ray data from Chandra, *XMM-Newton*, and *ROSAT* PSPC pointed observations only.

Planck SZ sources	1227		
Previously known clusters	683		
		X-ray only	472
		Optical only	182
		SZ only	16
		NED and SIMBAD	13
Planck new clusters	178		
		Confirmed with follow-up observations	157
		Confirmed with SDSS galaxy catalogues or archival data	21
Planck candidate new clusters	366		
		CLASS1	54
		CLASS2	170
		CLASS3	142

SIMBAD queries. The first identifiers of the *Planck* SZ detections given in Table B.1 reflect the validation hierarchy.

In the following, we present the results of the external validation process and of the follow-up campaigns for confirmation of *Planck* candidates and measurement of their redshifts (see Table 5 and Fig. 18). We also present the confirmation from SDSS galaxy catalogues and from X-ray archival data. We further discuss the unconfirmed candidate new clusters detected by *Planck*, which we classify into three categories of different reliability.

6.1. *Planck* clusters associated with known clusters

A total of 683 out of 1227 SZ detections in the *Planck* catalogue, i.e., 55.7%, are associated with previously-known clusters from X-ray, optical, or SZ catalogues, or with clusters found in the NED or SIMBAD databases. We give the number of clusters identified in each category and we discuss notable cases of known clusters that are not included in the *Planck* SZ catalogue.

6.1.1. Identification with known X-ray clusters

A total of 472 *Planck* SZ-candidates are identified with known X-ray clusters from the MCXC meta-catalogue, which represents 38.5% of the *Planck* SZ detections and 69.1% of the identifications with previously-known clusters. These identifications of course account for many Abell clusters in the RASS-based catalogues of X-ray clusters.

Using the cluster properties reported in the MCXC and the *Planck* noise maps at the cluster positions, we computed the expected SZ signal and the expected S/N ratio for a measurement with *Planck*. We have compared the number of detected clusters in the *Planck* catalogue with S/N $\geq$ 4.5 to the number MCXC clusters at an expected significance of 4.5. Only 68 clusters expected to be detected at S/N > 4.5 are not included in the *Planck* catalogue, including 16 with predicted S/N between 4 and 4.5. Of the 52 clusters with expected S/N $\geq$ 4.5, only 41 are outside the masked regions and could thus be in the PSZ catalogue. Our computation of the expected SZ signal and S/N were based on scaling relations for X-ray-selected clusters, not accounting for

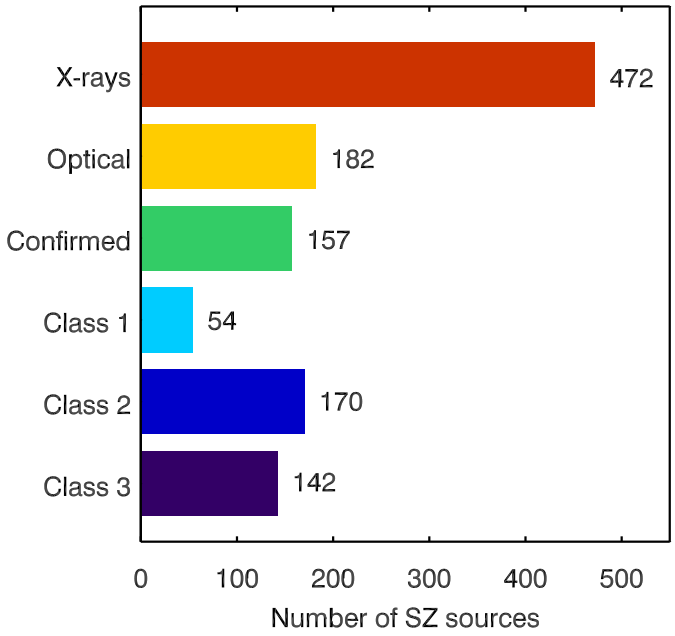

Fig. 18: Distribution of the *Planck* clusters and candidates in the different categories defined in the external validation process. The validation follows the order association with MCXC clusters, then Abell and Zwicky clusters, then SDSS clusters, then SZ clusters, and finally clusters from NED/SIMBAD.

the dispersion in the relations. We therefore focus on the non-detected MCXC clusters that significantly depart from the expected S/N value, namely by more than 5σ. A total of 13 clusters are in this category. The two objects RXCJ2251.7-3206 and RXCJ0117.8-5455 show emission in high-resolution *Chandra* imaging that is point-like rather than extended and are likely not clusters of galaxies (Mantz et al. 2010; Magliocchetti & Brüggen 2007). Of the other eleven missing MCXC clusters, some present AGN contamination. This is the case for RXC J1326.2+1230 (Magliocchetti & Brüggen 2007), RXJ1532.9+3021 (Hlavacek-Larrondo et al. 2012), RXCJ1958.2-3011, RXCJ2251.7-3206, and RXCJ0117.8-5455 (Magliocchetti & Brüggen 2007), Abell 689 (Giles et al. 2012), ZwCl2089 (Rawle et al. 2012), PKS 0943-76 (Abdo et al. 2010), and Abell 2318 (Crawford et al. 1999). In these cases, the presence of the AGN affects the X-ray luminosity measure leading to an overprediction of the SZ signal. Some exhibit significant radio contamination, e.g., RXCJ1253.6-3931 (Plagge et al. 2010) and RXCJ1958.2-3011 (Magliocchetti & Brüggen 2007), which hampers the SZ detection. Cool-core clusters for which the X-ray luminosity is boosted due to the central density peak have an over-estimated expected SZ signal. This is the case for RXCJ0425.8-0833 (Hudson et al. 2010), ZwCl2701 (Rawle et al. 2012), Abell 1361 (Rafferty et al. 2008), and RBS 0540 (Eckert et al. 2011; Belsole et al. 2005). Other "missing" clusters are CIZA clusters: RXC J0643.4+4214, RXC J1925.3+3705, RXC J2042.1+2426 and RXC J0640.1-1253, REFLEX cluster RXCJ2149.9-1859, APMCC 699, Abell 3995, Abell 2064 and RBS 171.

In addition to the clusters discussed above which are not included in the catalogue due to contamination by AGN or presence of cool-cores etc., we note that some notable nearby extended clusters are also not included in the *Planck* SZ catalogue. Indeed, the detection methods used to detect the SZ effect are not optimized for the detection of sources with scale radius θ_{500} in excess of 30 arcmin. Of the 25 clusters in this category (with $z < 0.03$) in the MCXC meta-catalogue, six are included in the *Planck* catalogue. The remaining 19 fall into the masked areas (seven out of 19, among which Perseus and Abell 1060 lie in the PS mask (Fig. 19, first two panels), and Ophiuchus and 3C 129.1 lie in the Galactic mask (Fig. 19, second two panels)) and/or have a S/N ratio below the PSZ catalogue threshold S/N = 4.5. This is the case of Virgo cluster (Fig. 19, lowest panel), which is detected in the *Planck* survey but with a signal-to-noise ratio at its position of about 3.9. Virgo's extension on the sky ($\theta_{500} = 168$ arcmin) further hampers its blind detection.

We show in Fig. 19 the reconstructed SZ signal from the `MILCA` algorithm (Hurier et al. 2010) for five of the "missing" extended clusters. These clusters, despite not being part of the *Planck* catalogue of SZ sources, are well detected in the *Planck* survey. They all are included in the thermal SZ map constructed from the *Planck* channel maps and presented in Planck Collaboration XXI (2013).

6.1.2. Identification with known optical clusters

A total of 182 *Planck* SZ detections are identified exclusively with optical clusters from Abell and Zwicky catalogues, and from the SDSS-based published catalogues, i.e., 26.6% of the known clusters in the *Planck* catalogue.

The *Planck* SZ candidates at S/N $\geq$ 4.5 have 111 exclusive associations with Abell or Zwicky clusters, i.e., with clusters not in any of the catalogues compiled in the MCXC meta-catalogue. In addition to these associations, 72 *Planck* detections are solely identified with clusters from the SDSS-based catalogues. These are either rich and massive systems ($R_{L^\star}$ greater than 110, $Q_{\rm SDSS} = 1$ clusters) or moderately low-richness systems ($Q_{\rm SDSS} = 2$ clusters, exhibiting hot gas as indicated by their S/N value in the RASS survey). However, not all the rich $Q_{\rm SDSS} = 1$ clusters in SDSS-based catalogues are found in the *Planck* catalogue. A total of 213 $Q_{\rm SDSS} = 1$ clusters from all four SDSS-based catalogues (201 outside the *Planck* union PS and Galactic mask) are not included in the *Planck* catalogue.

We explore why these rich clusters are not detected blindly by the SZ-finder algorithms. We first compare the richness-based masses against the X-ray luminosity-based masses of 26 of these "missing" clusters found in the MCXC meta-catalogue. We find a median ratio of 2.6 ± 1.2 for the richness-to-X-ray based masses, indicating that the richness-based masses seem to be systematically overestimated. Unlike the X-ray clusters, we thus cannot compute a reliable estimate of the expected S/N value for SZ detection of these optical clusters. We therefore directly search for the SZ signal at the positions of the 201 "missing" SDSS-clusters and found that all of them have S/N values below the *Planck* threshold, with a mean signal-to-noise of 1.6, except for three clusters. Two of these three "missing" SDSS-clusters have their S/N value from the extraction at the cluster position slightly higher than 4.5. The increase in S/N value is due to the difference in estimated background noise when centring the extraction at the cluster position as opposed to the blind detection. The third missing rich cluster is affected by contamination from CMB anisotropy, which results in a bad estimate of its size and consequently of its SZ signal.

6.1.3. Identification with known SZ clusters

The majority of the SZ clusters, from SPT or ACT, used in the validation process are low-mass systems ($M_{500}^{\rm median}$ around 2.3×10^{14} $M_\odot$). *Planck* is particularly sensitive to massive rich clusters and thus only a total of 56 of these clusters match *Planck* SZ detections, out of which 16 candidates are exclusively associated with SZ clusters[23] from ACT or SPT. Nine more ACT and SPT clusters are associated with *Planck* SZ detections between S/N = 4 and 4.5. We have searched for the SZ signal in the *Planck* data at the position of the remaining non-observed ACT/SPT clusters by extracting the SZ signal at their positions. We found that all had signal-to-noise values lower than 4.

We have also checked the redundancy of SZ detections within *Planck* by comparing the ESZ sample, constructed from 10 months of survey with a cut at Galactic latitudes of ± 14 degrees, with the present *Planck* catalogue. Of the 189 high significance ($(S/N)_{\rm ESZ} \geq 6$ ESZ detections, 184 ESZ confirmed clusters are included the present *Planck* catalogue within a distance of five arcmin from their ESZ position. The mean separation between the ESZ and present positions is of order 1.35 arcmin, within *Planck*'s positional accuracy. Their S/N values were increased by a factor 1.17 on average with respect to their $(S/N)_{\rm ESZ}$, (Fig. 20) and only four out of six of the ESZ clusters have new S/N values significantly lower than ESZ signal-to-noise threshold $(S/N)_{\rm ESZ} = 6$. They are displayed as stars in Fig. 20. Four ESZ clusters are not included the present *Planck* catalogue, they fall in, or nearby, the PS mask used for the pre-processing of the channel maps prior to running the detection algorithms. Such a mask was not utilized for the construction of ESZ sample. We choose not to a posteriori include these four "missing" ESZ clusters in the present *Planck* SZ catalogue.

[23] Six *Planck* clusters were confirmed from *XMM-Newton* or NTT observations and are also published in Reichardt et al. (2013).

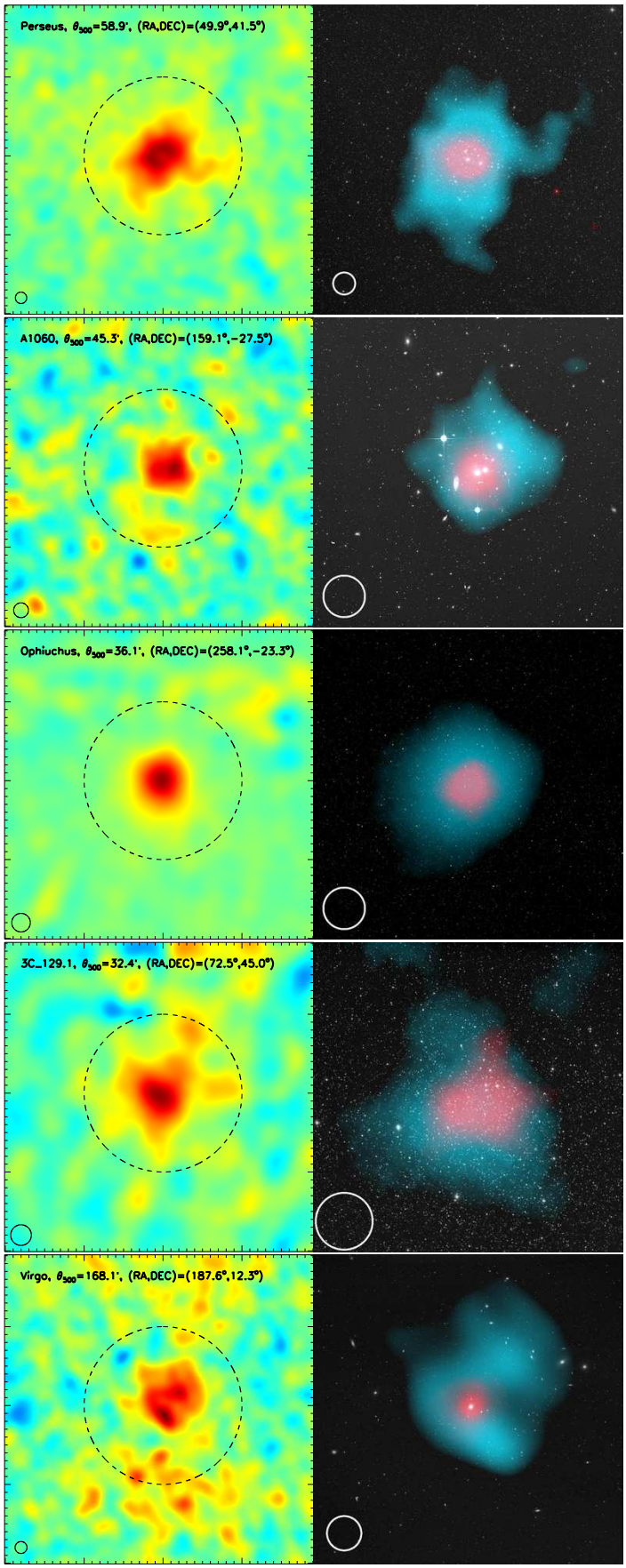

Fig. 19: Five selected nearby and extended clusters not included in the PSZ catalogue. All exhibit an extended SZ signal detected in the *Planck* survey. From top to bottom: Perseus cluster and Abell 1060 (in the point-source mask); Ophiuchus cluster and 3C 129.1 (in the Galactic mask); and Virgo cluster (below the S/N threshold of the catalogue). *Left panels:* reconstructed thermal SZ maps from the MILCA algorithm (Hurier et al. 2010). The dashed circles represent the apertures of θ_{500} from the MCXC catalogue. Each SZ-map covers an area of $4\theta_{500} \times 4\theta_{500}$. *Right panels:* composite images of the optical (DSS), X-ray (ROSAT) and SZ signal (*Planck*). The size of the composite images is adapted to optimize the display (Perseus: 2×2 square degrees; Abell 1060: 1×1 square degree; Ophiuchus: 1×1 square degree; 3C 129.1: 0.77×0.77 square degrees; Virgo: 3.84×3.84 square degrees). The solid circle in the left corner shows, both in the SZ *Planck* map and in the composite image, a 10 arcmin field of view; except for Virgo for which it shows a 30 arcmin field of view.

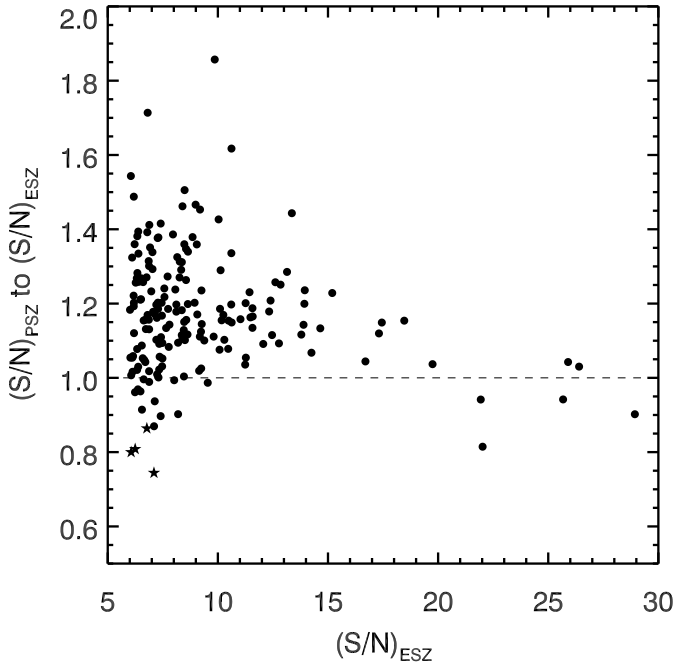

Fig. 20: Ratio of the signal-to-noise in the present *Planck* catalogue, $(S/N)_{PSZ}$, to that in the ESZ sample (Planck Collaboration VIII 2011), $(S/N)_{ESZ}$, for 184 confirmed ESZ clusters included in the *Planck* catalogue. Four clusters with signal-to-noise in the PSZ catalogue significantly smaller than the ESZ threshold ($(S/N)_{ESZ} = 6$) are shown as stars.

6.1.4. Identification with clusters from NED or SIMBAD

As expected only a small number of clusters are identified from querying the databases, supplying identifiers for thirteen SZ *Planck* detections. This is because the information in NED and SIMBAD is redundant with that in the X-ray, optical, or SZ catalogues used for the external validation. The thirteen clusters found solely from querying the databases are found in the RASS survey but not in dedicated cluster catalogues, and thus not included in the MCXC; they are found in serendipitous *Chandra* surveys, or they are part of miscellaneous cluster catalogues.

6.2. Newly-discovered Planck clusters and candidates

Among the 544 *Planck* SZ sources, we distinguish two categories: (1) confirmed clusters, i.e., those that have been confirmed by the follow-up programmes of the *Planck* collaboration[24] or using the SDSS galaxy catalogues. We also add eight confirmations from X-ray archival data; (2) Candidate clusters with different levels of reliability, namely, CLASS1 cluster candidates, that fulfil high-quality criteria for the SZ detection and for the associations and/or counterparts in ancillary data, CLASS2 candidate clusters, i.e., those that fulfil, on average, good-quality criteria, and CLASS3, low-reliability cluster candidates.

Confirmation from *Planck* collaboration follow-up programmes At S/N ≥ 4.5, a total of 233 *Planck* SZ detections were followed up in X-rays, optical, and SZ at the different facilities listed previously, with some observations targeted to the measurement of spectroscopic redshifts for already known clusters. In total 157 *Planck* SZ detections with S/N ≥ 4.5 were confirmed as new clusters. Some of the *Planck*-confirmed clusters were also reported in recent cluster catalogues in the optical, e.g., Wen et al. (2012) or in the SZ e.g., Reichardt et al. (2013).
The analysis of the observations of *Planck* sources by AMI yielded ten sources with strong Bayesian evidences that have clearly visible decrements and were considered as confirmed, including the confirmation of three associations with optical clusters.
For the candidates confirmed by *XMM-Newton* and by optical telescopes, redshifts from Fe lines and from photometric or spectroscopic data are available. The validation of *Planck* cluster candidates with *XMM-Newton* has shown its particular efficiency in confirming SZ candidates due both to the high sensitivity of *XMM-Newton*, allowing *Planck* clusters to be detected up to the highest redshifts (Planck Collaboration XXVI 2011), and the tight relation between X-ray and SZ properties. The detection of extended *XMM-Newton* emission and a comparison between the X-ray and SZ flux permits an unambiguous confirmation of the candidates. By contrast, confirmation in the optical may be hampered by the *Planck* positional accuracy and by the scatter between the optical observables and the SZ signal, which increase the chance of false associations. The *XMM-Newton* follow-up programme yielded 51 bona fide newly-discovered clusters, including four double systems and two triple systems. There were eight false candidates. Thirty-two of the 51 individual clusters have high-quality redshift measurements from the Fe line. The relation between the X-ray and SZ properties was used to further constrain the redshift of the other clusters; most of these redshifts were confirmed clusters using optical observations. Out of a total of 37 single clusters confirmed by *XMM-Newton*, 34 are reported in the *Planck* catalogue of SZ sources at S/N ≥ 4.5. Additionally four double systems are included in the present PSZ catalogue and were also confirmed by *XMM-Newton*.
The follow-up observations conducted with optical telescopes lead to the confirmation and to the measurement of spectroscopic or photometric redshifts (companion publications, in preparation, will present the detailed analysis and results from these follow-up). In the Northern hemisphere, 26 spectroscopic redshifts for *Planck* clusters detected at S/N ≥ 4.5 and observed at the RTT150 are reported, to date, in the PSZ catalogue. A dozen additional spectroscopic redshifts were measured for known clusters. Confirmation of 21 *Planck* SZ clusters detected above 4.5 were obtained with the ENO facilities (at INT, GTC and NOT), and robust redshift measurements were obtained for 19 of them, including 13 spectroscopic redshifts. In the Southern hemisphere, WFI observations provided photometric redshifts for 54 clusters included in the *Planck* catalogue at S/N ≥ 4.5, while 19 spectroscopic redshifts obtained with the NTT-EFOCS2 instrument are reported in the *Planck* catalogue.

Confirmation from SDSS galaxy catalogues The firm confirmation of the candidates was done through the follow-up observations for confirmation and measurement of their redshift as detailed above. However in the case of the *Planck* candidates falling in the SDSS footprint we also used the SDSS galaxy catalogues to search, as presented in Sect. 4.1.2, for galaxy overdensities associated with *Planck* SZ detections. This provides us with an estimate of the photometric redshifts, and in some cases we could retrieve spectroscopic redshifts for the BCG as well.

[24] A handful of new *Planck* clusters from the ESZ sample were confirmed independently from the *Planck* collaboration by SPT (Story et al. 2011), AMI (AMI Consortium et al. 2011), Bolocam (Sayers et al. 2012a) and CARMA (Muchovej et al. 2012).

In this process, the major uncertainty in the associations of *Planck* SZ detections with galaxy overdensities is due to chance associations with low-richness systems or associations with diffuse concentrations of galaxies in the SDSS data. The *XMM-Newton* confirmation programmes (see Planck Collaboration Int. IV (2013) for discussion) showed that *Planck* candidates with SDSS counterparts were confirmed including PLCK G193.3−46.1 at $z \simeq 0.6$. However, the X-ray analysis of the *Planck* detections with SDSS counterparts illustrated the difficulty in distinguishing between associations of *Planck* SZ signals with massive clusters and with pre-virialized structures. In particular, in the case of extended filamentary structures or dynamically perturbed sources, an offset between the BCG position and the concentration barycentre is noted.

We considered the *Planck* SZ candidates with counterparts in the SDSS data taking into account diagnostics such as the richness/mass estimates as well as the offsets between the SZ, the BCG and the barycentre positions. We further used the outputs of the search in WISE and in RASS data, and the associated images, in order to assess the significance of the galaxy overdensity in SDSS at the position of the *Planck* candidates. For the *Planck* SZ detections where both ancillary data and SDSS barycentre/BCG positions agreed, we set that they are confirmed. We found a total of 13 such associations for which we report the photometric or the spectroscopic redshifts. It is worth noting that firm confirmation of these associations is needed and needs to be performed using either optical spectroscopic observations or X-ray observations of the *Planck* SZ detections. In the cases where the offsets between barycentre and BCG position output by the search in SDSS data were too large, and/or when other ancillary information was unable to discriminate between reliable or chance associations, we have chosen to keep the status of candidate for the *Planck* SZ detection. These cases sometimes also coincide with association of *Planck* detections with clusters from the SDSS cluster catalogues, with a quality flag $Q_{\rm SDSS} = 0$, or with confusion in the association, i.e., with positions not in agreement between counterpart and published SDSS clusters. We provide a note for all these cases in order to indicate that an overdensity in SDSS data was found.

Candidate new clusters The remaining 366 *Planck* SZ sources, not identified with previously known cluster nor confirmed by follow-up observation or ancillary data, are distributed over the whole sky (Fig. 21) and are yet to be firmly confirmed by multi-wavelength follow-up observations. They are characterized by an ensemble of quality flags defined in Sects. 4.1.1, 4.1.2, and 4.1.3 based on the systematic searches for counterparts in the public surveys during the external validation process. We further define an empirical *Planck*-internal quality flag $Q^{\rm SZ}$. It assesses the reliability of the SZ detection itself from three independent visual inspections of the nine *Planck* frequency maps, of frequency maps cleaned from Galactic emission and CMB, and of reconstructed *y*-maps or *y*-maps produced from component separation methods (e.g., Hurier et al. 2010; Remazeilles et al. 2011). Moreover, we visualize the SZ spectra from the SZ-finder algorithms and from aperture photometry measurements at the candidate positions. Finally we correlate, at the position of the *Planck* SZ candidates and within an area of 10 arcmin radius, the *y*-map to the 857 GHz channel map, as a tracer of the dust emission, and to the *Planck* mono-frequency CO map at 217 GHz (Planck Collaboration XIII 2013). The qualitative flag $Q^{\rm SZ}$ combines all this information into three values 1 to 3 from highest to lowest reliability with the following criteria:

– $Q^{\rm SZ} = 1$, i.e., high reliability: (i) Clear compact SZ source in the SZ maps; (ii) significant measurements of the SZ decrement below 217 GHz and good or reasonable detection at 353 GHz; (iii) no correlation with dust nor CO emission and no rise of the 545 and 857 GHz fluxes on the thermal SZ spectrum.
– $Q^{\rm SZ} = 2$, i.e., good reliability: (i) visible SZ detection in the SZ map or significant detection of the SZ signal below 217 GHz; (ii) contamination causing rise of the 545 GHz and possibly 857 GHz flux on the SZ spectrum without a strong correlation with dust and CO signals.
– $Q^{\rm SZ} = 3$, i.e., low reliability: (i) weak SZ signal in the *y*-maps and/or noisy SZ maps; (ii) weak or no SZ signal in the cleaned frequency maps (iii) strong correlation (≥80%) with dust and CO emission contamination with rising fluxes on the SZ spectrum at high frequencies, 353 GHz and above.

We combine the qualitative SZ quality flag with the information from the search in the all-sky surveys, RASS and WISE, for counterparts of *Planck* candidates in order to assess the overall reliability of the cluster candidates. We thus distinguish three classes of candidates:

- **CLASS1** candidates. *Highly-reliable candidates or pre-confirmed clusters:* these are the *Planck* SZ detections that have a high probability of being associated with bona fide clusters and need to fulfil high-quality criteria for SZ, RASS, and WISE detections. We retain in this category *Planck* SZ detections with high or good SZ quality flags ($Q^{\rm SZ} = 1$ or 2) and with a RASS-BSC source (not coinciding with stars) or with $({\rm S/N})_{\rm RASS} \geq 2$, i.e., SZ detections with quality flag $Q_{\rm RASS} = 1$. The CLASS1 candidates furthermore have to fulfil a condition of high or good probability (≥80%) of being associated with an overdensity of galaxies in the WISE survey.
  We find 54 CLASS1 *Planck* candidates ranging from S/N of 4.5 to 6.3, with a median signal-to-noise ratio of 4.8. The majority of them are detected by two methods and 25.9% of them are detected only by one method. They are distributed as 26 and 28 $Q^{\rm SZ} = 1$ and 2 candidates, respectively. These candidates show significant X-ray emissions with a median $({\rm S/N})_{\rm RASS} \simeq 3.7$ and a mean of 4.2.
- **CLASS2** candidates. *Reliable cluster candidates:* they represent 170 *Planck* SZ detections that show good or high quality criteria either in SZ or in RASS or in WISE without fulfilling all of them at once. Amongst them 61 have $Q^{\rm SZ} = 1$ and 109 have $Q^{\rm SZ} = 2$.
- **CLASS3** candidates. *Low-reliability cluster candidates:* these *Planck* SZ detections are the poor-quality, $Q^{\rm SZ} = 3$, detections. They can also be associated with good quality, $Q^{\rm SZ} = 2$, detections for which there are no good indications of the presence of an X-ray counterpart ($({\rm S/N})_{\rm RASS} < 0.5$ and high probability of false association with FSC sources >2.5%) or a counterpart in the WISE survey (probability of association <70%).
  This class of candidates contains 142 *Planck* SZ detections with 27 and 115 SZ detection of quality $Q^{\rm SZ} = 2$ and 3, respectively.

It is worth noting that this definition of the CLASS3 *Planck* candidates is dominated by the assessment of the SZ quality complemented by information from ancillary data. In doing so we assemble in this category of candidates the SZ detections that are either false or very low quality due to contamination. Moreover, according to the statistical characterization from simulations,

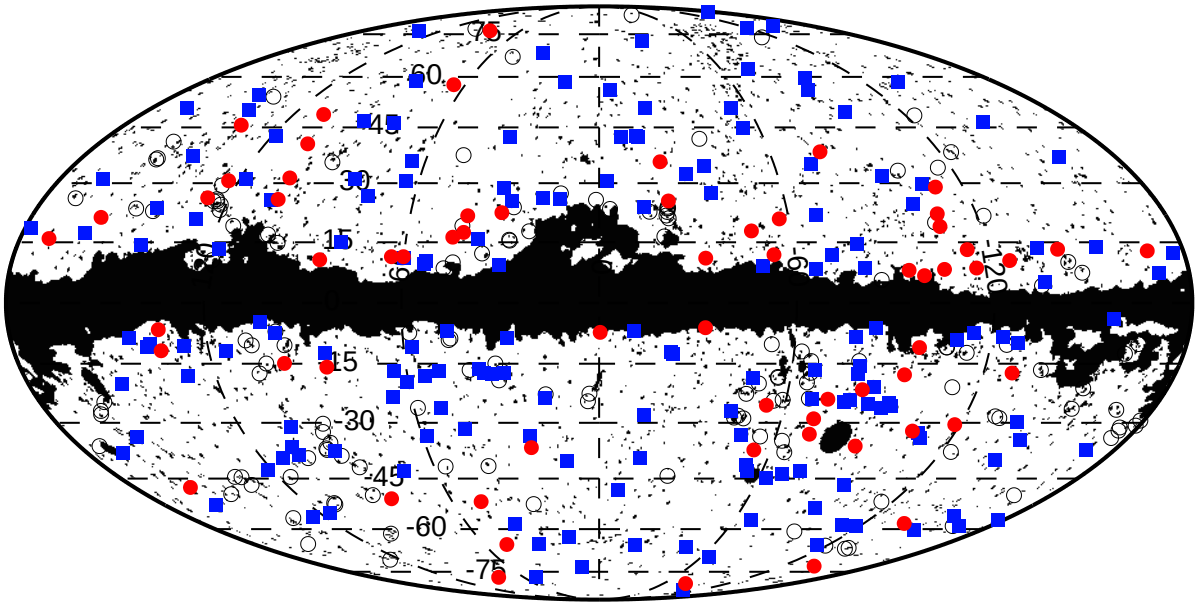

Fig. 21: Distribution of the *Planck* SZ candidates across the sky. Blue symbols represent the CLASS1 candidate clusters and red the CLASS2 candidates. The open symbols stand for the CLASS3 low-reliability SZ sources.

about 200 false detections are expected. The number of false detections could be smaller since the simulations do not reproduce the entire validation procedure, in particular omitting the cleaning from obvious false detections. Figure 22 suggests that the CLASS3 candidates are likely to be dominated by false detections. Therefore, we would like to warn against dismissing entire CLASS3 of the catalogue as populated with false detections as some CLASS3 candidates may be real clusters. For this reason, we choose not to remove these detections from the PSZ catalogue but rather flag them as low-reliability candidates. Careful follow-up programmes are needed in order to separate real clusters of galaxies from false detections among the CLASS2 and CLASS3 objects.

In order to illustrate our classification defined in terms of reliability, we stack the signal in patches of 2.51 degrees across, centred at the position of the *Planck* clusters and candidates in the nine channel maps of *Planck*, removing a mean signal estimated in the outer regions where no SZ signal is expected (see Fig. 22 with the rows arranged from 30 GHz, upper row, to 857 GHz, lower row). The stacked and smoothed images are displayed for the *Planck* SZ detections identified with known clusters, CLASS1, CLASS2 and CLASS3 candidates, Fig. 22 from left to right column. We clearly see the significant detection of both the decrement and increment of the 683 *Planck* clusters and of the *Planck* candidates of CLASS1 and CLASS2. For the *Planck* SZ detections associated with bona fide clusters the increment is clearly seen at 353 and 545 GHz and is detected at 857 GHz. The smaller sample of the CLASS1 highly reliable candidates shows, in addition to the decrement at low frequency, a good detection of the increment at 353 GHz. The significance of the increment at 545 GHz is marginal and no signal is seen at 857 GHz. The case of the CLASS2 candidates (good reliability) shows that we now have lower-quality SZ detections (62% of the CLASS2 candidates have a good but not high SZ quality flag). This is illustrated by the fact that an excess emission is detected at 217 GHz, most likely due to contamination by IR sources, and both at 545 and 857 GHz where emission from dust is dominating. As for the stacked signal of the CLASS3 sample of low-reliability candidates, it does not show any significant SZ detection across frequencies, as compared to the sample of *Planck* detections identified with known clusters (Fig. 22, right column). This confirms on statistical grounds the definition of the sample dominated by definition by the low-quality SZ, $Q^{\rm SZ} = 3$, detections representing 84% of the detections in this class. Not surprisingly, the stacked signal of the CLASS3 candidates shows a large amount of contamination across all *Planck* frequencies. The low-frequency signal is dominated by radio contamination, and/or CO emission at 100 GHz, while the high-frequency signal is contaminated by emission from dust or extragalactic point sources. A more quantitative analysis is presented in Sect. 7.1.

6.3. Summary of the external validation and redshift assembly

The *Planck* catalogue of SZ sources comprises a total of 861 identified or confirmed clusters with only nine percent of them being detected by one SZ-finder algorithm. We summarize in Table 5 and Fig. 18 the results of the cluster identification. Figure 23 illustrates the status of the *Planck* SZ detections. In particular, 70.2% of the *Planck* SZ detections with S/N≥4.5 have so far been associated with clusters. The fraction increases to about 73% at S/N = 6.

We have assembled, at the date of submission, a total of 813 redshifts for the 861 identified or confirmed *Planck* clus-

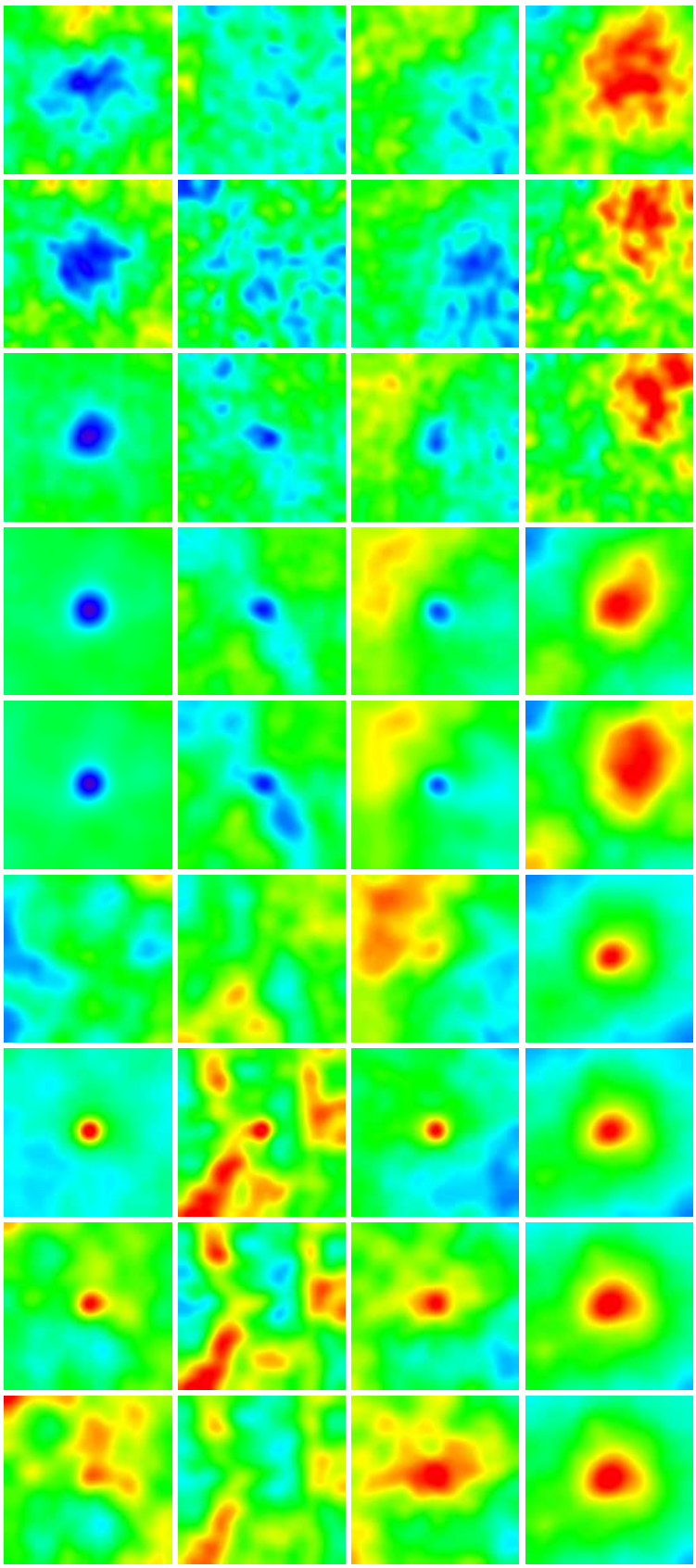

Fig. 22: Stacked signal in the nine *Planck* frequencies (30 to 857 GHz from upper to lower row). From left to right are displayed the *Planck* SZ detections identified with known clusters, the CLASS1 high-reliability *Planck* SZ candidates, the CLASS2 good-reliability *Planck* SZ candidates, and finally the CLASS3 low-reliability SZ sources. The three lowest-frequency-channel images were convolved with a 10 arcmin FWHM Gaussian kernel, whereas the remaining six highest-frequency-channel images were smoothed with a 7 arcmin FWHM Gaussian kernel.

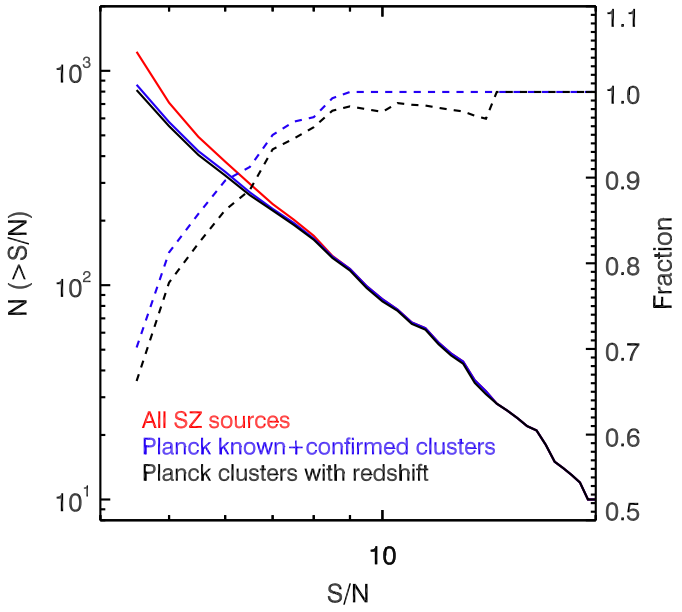

Fig. 23: Status of the *Planck* SZ sources. Left-hand-axis plots show the distribution of all *Planck* sources (in red). The blue line represents the known or new confirmed clusters and, among these, the clusters with a reported redshift measurement in black. Right-hand-axis cumulative distributions show, as a function of signal-to-noise, the fraction of known or new confirmed clusters in blue and those with a redshift in black.

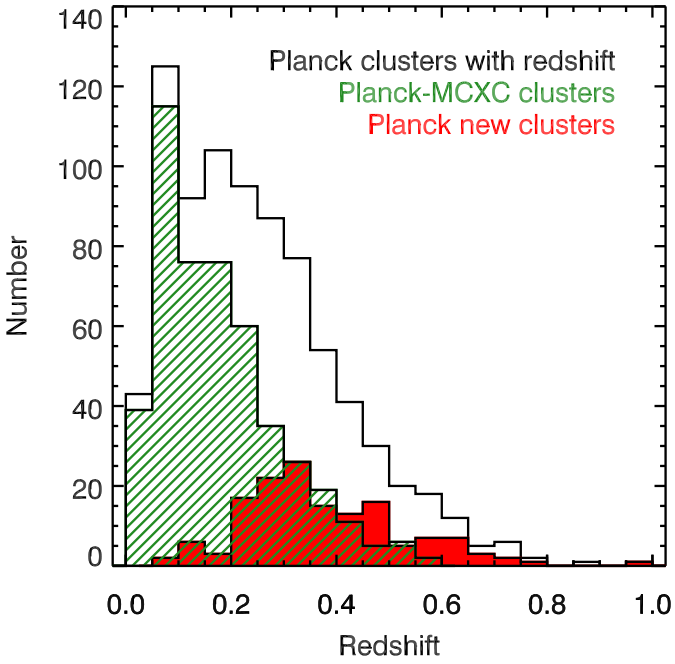

Fig. 24: Distribution of redshifts for the *Planck* SZ clusters (black line). The *Planck* clusters associated with MCXC clusters are shown in dashed green and the brand new *Planck* clusters are in the filled red histogram.

ters, which we provide together with the published *Planck* catalogue. Their distribution is shown in Fig. 24. In the process of the redshift assembly that is summarized below, especially for the already known clusters, we have favoured homogeneity for the sources of redshift rather than a cluster-by-cluster assembly of the most accurate z measure. A large fraction of the redshifts, 456 of them, shown as the dashed green histogram in Fig. 24 correspond to the spectroscopic redshifts quoted in the updated MCXC meta-catalogue (Piffaretti et al. 2011). They are associated with the *Planck* clusters identified with known X-ray clusters and they are denoted *Planck*-MCXC. For the *Planck*-MCXC clusters without reported redshifts from the MCXC, we have complemented the information with the available redshifts from NED and SIMBAD. We have further quoted when available, mainly for the MACS clusters, the estimated photometric redshifts from SDSS cluster catalogue of Wen et al. (2012). At the end only two *Planck* detections identified with MCXC clusters remain without redshifts. The redshift distribution of the *Planck* clusters identified with MCXC clusters mostly reflects that of the REFLEX/NORAS catalogues at low and moderate redshifts and the MACS clusters at higher redshifts.

For the *Planck* detections exclusively identified with Abell or Zwicky clusters, we choose to report the redshifts published in the NED and SIMBAD data bases rather than those quoted in the native catalogues. As for the *Planck* detections identified with clusters from the SDSS-based catalogues, we choose to favour homogeneity by reporting whenever possible the Wen et al. (2012) redshifts. Furthermore, we favour when available spectroscopic redshifts over photometric ones. The *Planck* detections exclusively associated with ACT or SPT clusters have published redshifts (Sifon et al. 2012; Hasselfield et al. 2013; Reichardt et al. 2013). We select in priority the spectroscopic ones when available. If not, we quote the photometric redshifts.

Finally, the follow-up observations for confirmation of *Planck* detections started in 2010 and are still ongoing. As mentioned earlier our priority was to assemble the largest possible number of confirmations and redshifts. Therefore, we did not systematically confirm the photometric redshift estimates spectroscopically. We report the obtained redshifts when available. In some cases, the new *Planck* clusters were confirmed from imaging or pre-imaging observations and the analysis is still ongoing. The spectroscopic redshifts will be updated when available. Spectroscopic redshifts for some known clusters will also be updated. A dozen *Planck* clusters were confirmed by a search in the SDSS galaxy catalogues. For these clusters, only a photometric redshift estimated by the cluster-finder algorithm of Fromenteau et al. (2013) is available and is reported.

We show in Fig. 24 the distribution of redshifts of the *Planck* clusters. The mean redshift of the sample is 0.25 and its median is 0.22. One third of the *Planck* clusters with measured redshifts lie above $z = 0.3$. The new *Planck* clusters probe higher redshifts and represent 40% of the $z \geq 0.3$ clusters. Their mean redshift is 0.38 and the median is $z = 0.35$. At even higher redshifts, $z \geq 0.5$, the *Planck* catalogue contains 65 clusters including *Planck* SZ clusters identified with WHL12's clusters (Wen et al. 2012), or with clusters from ACT and SPT, or with X-ray clusters. The *Planck* detections in this range of redshifts, 29 *Planck* new clusters, almost double the number of high redshift clusters.

The *Planck* SZ catalogue has been followed up by the *Planck* collaboration using different facilities and only a small fraction of the *Planck* candidates were observed to date. A systematic follow-up effort for the confirmation of the remaining cluster candidates will likely reveal clusters at redshifts above 0.3. As a matter of fact, very few new clusters were found below $z = 0.2$ (see Fig. 24). Such an observational programme is challenging and will most likely be undertaken by the *Planck* collaboration

and by the community. It will increase further the value of the *Planck* SZ catalogue as the first all-sky SZ-selected catalogue.

7. Physical properties of *Planck* SZ clusters

The first goal of the external validation process based on the ancillary multi-wavelength data is to assess the status of the *Planck* SZ detections in terms of known clusters, brand new clusters or cluster candidates. The wealth of information assembled and used during this process also allows us to explore the properties of the *Planck* SZ clusters and candidates. We present in the following some of these properties, namely the contamination levels of the *Planck* SZ detections, a refined measurement of the Compton Y parameter for the *Planck* clusters identified with X-ray clusters from the MCXC, an SZ-mass estimate based on a new proxy for all the *Planck* clusters with measured redshifts, and an estimate of the X-ray flux from the RASS data for the *Planck* SZ detections not included in the X-ray catalogues. This additional information associated with the *Planck* clusters and candidates derived from the validation process is summarized in the form of an ensemble of outputs given in Table C.1.

We further present an updated and extended study of the SZ versus X-ray scaling relation, confirming at higher precision the strong agreement between the SZ and X-ray measurements (within R_{500}) of the intra-cluster gas properties found by Planck Collaboration XI (2011).

7.1. Point-source contamination

Galactic and extragalactic sources, emitting in the radio or infrared domain, are known to lie in galaxy clusters and hence are a possible source of contamination for the SZ measurement (e.g., Rubiño-Martín & Sunyaev 2003; Aghanim et al. 2005; Lin et al. 2009). We address the possible contamination of the SZ flux by bright radio sources that may affect the measured signal in the direction of some of the *Planck* SZ detections. In order to do so, we searched for known radio sources in the vicinity of the *Planck* cluster candidates. In particular, we use the NVSS 1.4 GHz survey (Condon et al. 1998) and SUMMS 0.85 GHz survey (Bock et al. 1999) to identify bright radio sources within seven arcmin of the *Planck* cluster or candidate position. We assumed a spectral index $\alpha = -0.5$ for these sources to extrapolate their flux to the *Planck* frequencies. Most bright sources in NVSS and SUMSS have steeper spectral indexes (-0.6 or -0.7), so the value $\alpha = -0.5$ provides us with an upper limit in most cases. After convolving the radio sources by *Planck*'s beam, we estimate the maximum amplitude in units of μK within five arcmin of the *Planck* position. We report only those cases where this amplitude is above 5 μK in the 143 GHz channel and could thus contaminate the SZ signal. Below this value, the emission from radio sources can be considered negligible.

We find that a total of 274 *Planck* clusters and candidates, i.e., 22% of the SZ detections, are affected by such emission from bright radio sources. These clusters or candidates are identified in the PSZ catalogue and a specific note is provided. We find that the fraction of contaminated *Planck* SZ clusters identified with known X-ray, optical, or SZ clusters is also 22%. The *Planck* candidate-clusters of CLASS1 and CLASS2 are less contaminated by bright radio sources; only a fraction of 15% and 17% for CLASS1 and 2, respectively. This is due to the definition of our quality criteria for SZ detection, which results in less contamination for the high and good reliability candidates.

Another approach used to assess the contamination is based on the stacking analysis of the *Planck* clusters and candidates described in Sect. 6.2. This analysis is performed on the sample of *Planck* clusters identified with known clusters and on the sample of low-reliability CLASS3 *Planck* candidates. To do so we fit a GNFW pressure profile to the signal at 100 GHz and 143 GHz and we subtract the associated SZ signal from

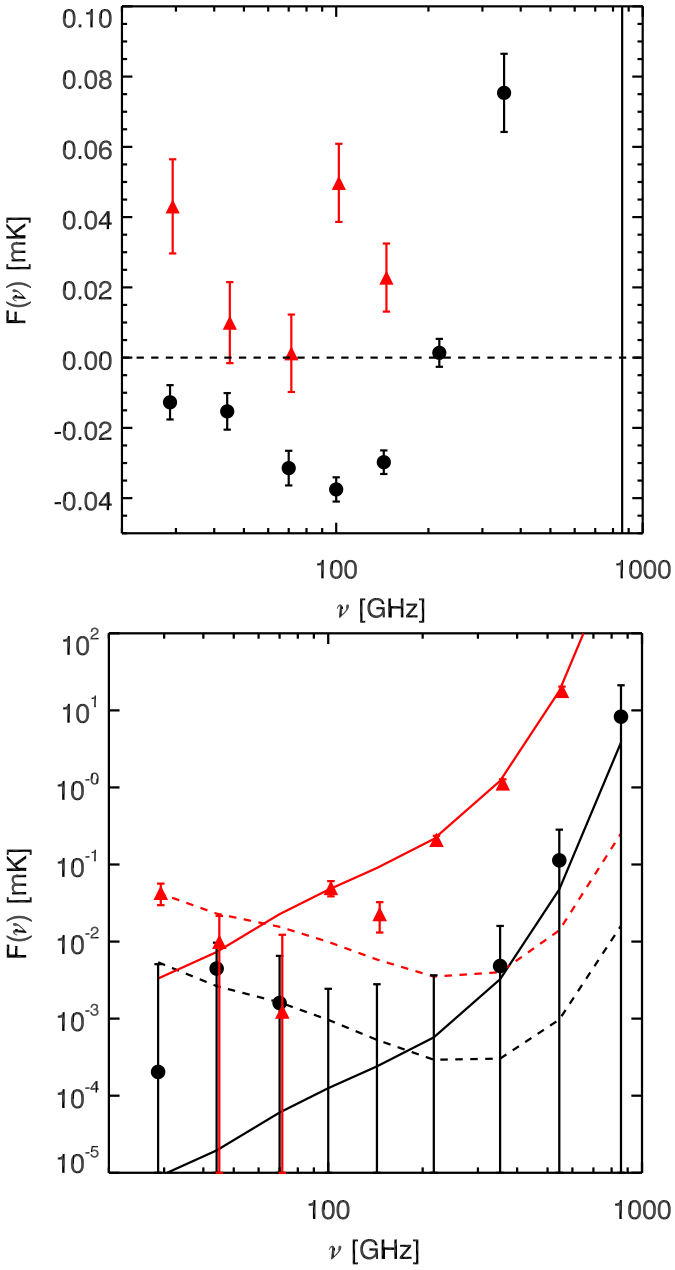

Fig. 25: Stacked spectrum for known clusters SZ fluxes across *Planck* frequency bands. Stacked fluxes are measured in an aperture equal to the FWHM of the 143 GHz channel (i.e., about 7 arcmin) for the known clusters (black filled circles) and the low-reliability CLASS3 candidates (red filled triangles). The associated uncertainties correspond to the fluctuation of the background outside the cluster region. The average signal is estimated in each channel before (upper panel) and after (lower panel) the removal of the SZ signal. The average signals expected from IR and radio sources are shown as solid and dashed lines, respectively. Red and black lines are for CLASS3 and bona fide clusters, respectively. No subtraction of an SZ signal is performed for the CLASS3 candidates.

the stacked maps. The residual signal is then compared with a toy model for point sources ($F_\nu = S_{30}^{\rm rad}(\nu/30\,{\rm GHz})^{\alpha_{\rm rad}}$ for radio sources) and ($F_\nu = S_{857}^{\rm IR}(\nu/857\,{\rm GHz})^{\alpha_{\rm IR}}$ for IR point sources). Note that the residual signal at high frequencies is a combination of possible IR sources and IR emission from Galactic dust; the latter is not explicitly modelled in the present analysis. The PS toy models are convolved by the beam at each frequency and the signal is measured at a fixed aperture set to the FWHM of the 143 GHz channel. The average signal within this aperture is estimated for each channel before (Fig. 25, upper panel) and after (Fig. 25, lower panel) removal of the SZ signal. The black filled circles are for *Planck* SZ sources associated with known clusters and the red filled triangles stand for CLASS3 candidates. The average signal from the PS models is shown in Fig. 25 as solid (IR sources) and dashed (radio sources) lines. Red and black are for CLASS3 and bona fide clusters, respectively. The error bars correspond to the fluctuation of the background outside the cluster region. For the sample of CLASS3 candidates no SZ-signal removal was applied, since no significant detection is seen at 100 GHz or 143 GHz.

We find that the residual signal (after SZ subtraction) in the sample of known *Planck* clusters is compatible with the emission from radio sources at low frequencies with $(S_{30}^{\rm rad}, \alpha_{\rm rad}) = (14.6\,{\rm mJy}, -1)$ for the known clusters. It is also compatible with IR emission at high frequencies with a spectral index $\alpha_{\rm IR} = 2.5$, in agreement with the results of Planck Collaboration Int. VII (2013) and with $S_{857}^{\rm IR} = 0.117$ Jy. For CLASS3, where no SZ signal is subtracted, it is the full signal that is compatible with the IR emission at high frequencies, with $(S_{857}^{\rm IR}, \alpha_{\rm IR}) = (43.9\,{\rm Jy}, 2.5)$, and with radio emission from point sources with $(S_{30}^{\rm rad}, \alpha_{\rm rad}) = (117.1\,{\rm mJy}, -0.8)$.

7.2. Refined measurement of Y

While the true Y_{500} is expected to be a low-scatter mass proxy, this is not the case for the blind Y_{500}. Without a cluster-size estimate, Y_{500} cannot be accurately measured. Moreover, the blind SZ flux is biased high on average, because the size is overestimated on average. This effect is amplified by the non-linear nature of the size–flux degeneracy, with a larger effect of size over-estimation than size under-estimation. This behaviour, first identified and discussed in Planck Collaboration VIII (2011) and Planck and AMI Collaborations (2013), hampers the direct use of the blind SZ fluxes as a mass proxy. As shown in Planck Collaboration VIII (2011), this degeneracy calls for a refined measurement of the SZ signal. In this section, we present two ways of refining the Y measurement. Both are based on fixing the cluster size in two cases, by setting it equal to the X-ray estimated size or by using the redshift information when available. The outputs of the refined measurement are provided as additional information complementary to the catalogue of *Planck* SZ detections (see Appendix C and Table C.1).

7.2.1. Y at fixed X-ray size and position

As shown by Planck Collaboration VIII (2011), the size–flux degeneracy can be broken by introducing a higher-quality estimate of the cluster size θ_{500}. This prior is directly provided by X-ray observations using an X-ray mass proxy such as $Y_{\rm X}$ or the luminosity $L_{\rm X}$. Resorting to estimates of the cluster size from optical richness is also possible, but suffers from the large scatter in richness–mass relation, as discussed previously.

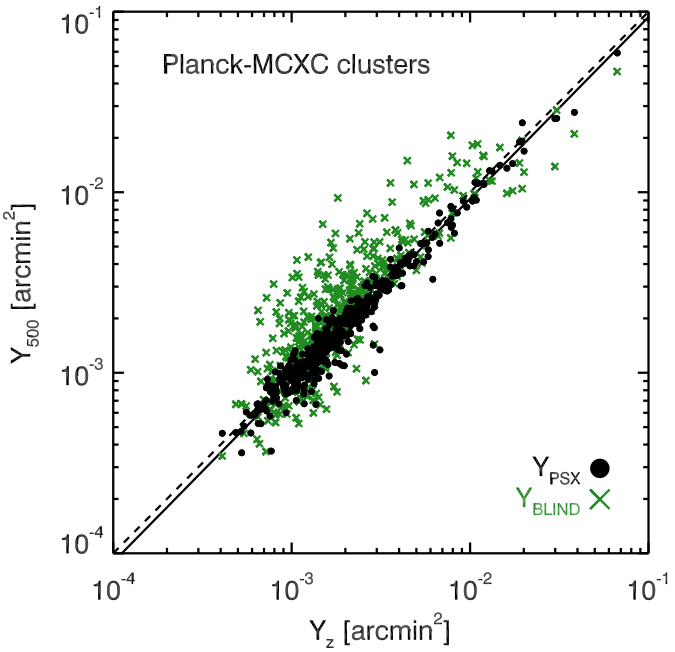

Fig. 26: Comparison of the different Y estimates for the *Planck* clusters identified with MCXC clusters. In green are the blind measured Y values and in black are the refined $Y_{500,\rm PSX}$ measured fixing the size and positions to the X-ray values. Both are plotted as a function of the new proxy Y_z.

A detailed investigation of the effects of fixing the cluster size was presented in Planck Collaboration XI (2011, Appendix A). Following this approach, and for the *Planck* detections identified with clusters from the MCXC meta-catalogue, we have adopted the R_{500} and z values reported in Piffaretti et al. (2011) as priors to re-extract at the X-ray position the SZ signal denoted $Y_{500,\rm PSX}$ assuming the Arnaud et al. (2010) pressure profile (see Table C.1). The comparison between the blind Y_{500} and refined $Y_{500,\rm PSX}$ (Fig. 26) shows that both the scatter and the offset are significantly reduced by the refined SZ measure. The SZ re-extraction at X-ray position and fixing the size to the X-ray derived size provides an unbiased estimate of the SZ signal. However, as stressed in Planck Collaboration XI (2011, Appendix A), the MCXC cluster size derivation involves the M_{500}–$L_{\rm X,500}$ relation, which exhibits a non-negligible scatter. This leads to a remaining systematic discrepancy between the expected Y value from X-ray measurements and the actual SZ flux derived from the *Planck* data. The use of the $Y_{\rm X}$ proxy does not suffer from such an effect, but high-quality X-ray data permitting the use of such a quantity are not available for a large number of clusters (see Sect. 7.5 for the presentation of a sample of *Planck* SZ clusters with high-quality X-ray data).

7.2.2. Y from the $Y(\theta)$–M relation

The size–flux degeneracy can further be broken, as proposed by Arnaud et al. (2013), using the M_{500}–$D_{\rm A}^2 Y_{500}$ relation itself that relates θ_{500} and Y_{500}, when z is known. Then Y_{500} is derived from the intersection of the M_{500}–$D_{\rm A}^2 Y_{500}$ relation and the size–flux degeneracy curve. A detailed description of the method and the comparison of results in terms of bias and scatter can be found in Arnaud et al. (2013).

The derived Y_{500} parameter is denoted Y_z (since it involves a measurement of the Compton Y signal for clusters with mea-

sured redshift z). It is the SZ mass proxy Y_z that is equivalent to the X-ray mass proxy Y_X. Y_z is computed for all the 813 *Planck* clusters with measured redshifts. We use Malmquist-bias-corrected scaling relation between mass and Y given in Planck Collaboration XX (2013)

$$E^{-2/3}(z)\left[\frac{D_A^2(z)\,Y_{500}}{10^{-4}\,\mathrm{Mpc}^2}\right] = 10^{-0.19}\left[\frac{M_{500}}{6\times10^{14}\,\mathrm{M}_\odot}\right]^{1.79}, \quad (5)$$

with $E^2(z) = \Omega_m(1+z)^3 + \Omega_\Lambda$ computed in the fiducial ΛCDM cosmology.

In Fig. 26, the refined Y_{500} value, measured fixing the size and position to the X-ray values $Y_{500,PSX}$, is compared to the blind Y as a function of the derived Y_z proxy. We see that the scatter and the offset are significantly reduced.

Under the two hypotheses of cosmology and scaling relation, Y_z provides the best estimate of Y_{500} for the *Planck* SZ clusters and conversely a homogeneously-defined estimate of an SZ-mass, X-ray calibrated, denoted $M_{500}^{Y_z}$. For the ensemble of *Planck* clusters with measured redshifts, the largest such sample of SZ-selected clusters, we show in Fig. 27 the distribution (black solid line) of the masses obtained from the SZ-based mass proxy. The distribution of the SZ masses is compared with those of the RASS clusters (dashed blue line) computed from the X-ray luminosity $L_{X,500}$. The mean and median masses of the *Planck* clusters are 3.3 and $3.5\times10^{14}\,\mathrm{M}_\odot$, respectively. The *Planck* SZ catalogues contains all the massive clusters of the RASS catalogues. Interestingly, the distribution of newly-discovered *Planck* clusters extends to higher masses with a median mass of $5.7\times10^{14}\,\mathrm{M}_\odot$. Besides providing a homogeneous estimate of the masses from an SZ proxy for the largest SZ selected sample of clusters, we show that *Planck* detections significantly extend the mass range in the high-mass region up to $1.6\times10^{15}\,\mathrm{M}_\odot$.

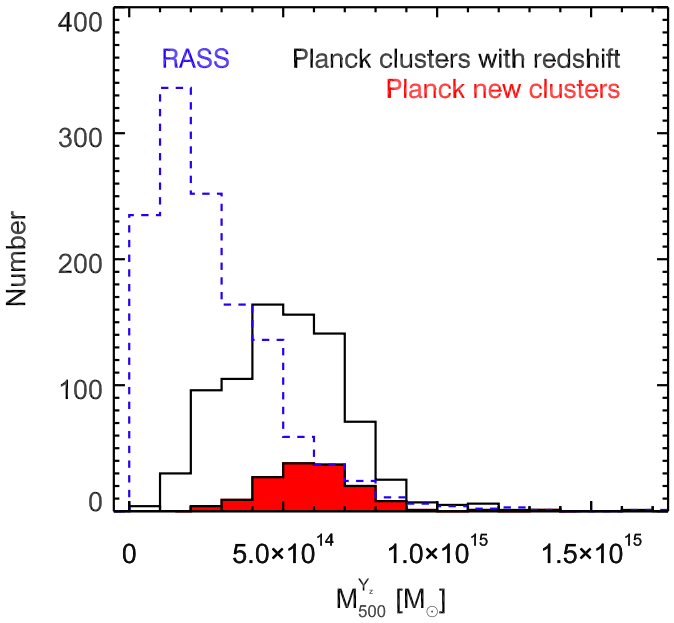

Fig. 27: Distribution of masses for the *Planck* SZ clusters, known or new confirmed clusters (solid black line), compared to the distribution of masses from the RASS-based cluster catalogues (dashed blue line). The masses for the MCXC clusters are estimated from the luminosity–mass relation. The masses for the *Planck* clusters are computed using the SZ-proxy. The filled red histogram shows the distribution of the newly-discovered *Planck* clusters.

7.3. *M–z* distribution and comparison with other surveys

Based on the masses derived from the SZ-proxy, we illustrate for `MMF3` the *M–z* distribution of *Planck* SZ clusters detected over 83.7% of the sky. We show in all panels of Fig. 28 the limiting mass M_{lim} computed following Planck Collaboration XX (2013) for three values of the completeness: 20% (solid line); 50% (dashed line); and 80% (dotted line). The upper left panel exhibits the *Planck* clusters, with redshifts, detected by `MMF3` at S/N≥4.5. The mass limit corresponds to the average limit computed from the noise over the 83.7% sky fraction used by the SZ-finder algorithm. The resulting M_{lim} is not representative of the inhomogeneity of the noise across the sky (see Fig. 3). We therefore show the limiting mass in three areas of the sky (Fig. 3): the deep-survey area (upper right panel); the medium-deep survey area (lower left panel); and the shallow-survey area (lower right panel). The lines indicate the limit at which clusters have C% chances to be detected (C being the completeness value). We clearly see that whereas the average M_{lim} at 20% completeness does not fully represent the SZ detections by `MMF3`, the limiting masses in different survey depths are more representative of the detection process. We further note that except at low redshifts, $z < 0.3-0.4$, the *Planck* cluster distribution exhibits a nearly redshift-independent mass limit with a cut that varies according to the survey depth.

It is worth examining the distribution of the *Planck* SZ clusters in the *M–z* plane and comparing it to that of other catalogues. For illustration, we compare to an X-ray selected sample, namely REFLEX-I, on the one hand (Fig. 29, right panel green open circles) and to the large-area SZ-selected cluster catalogues by ACT (Hasselfield et al. 2013) and SPT (Reichardt et al. 2013), on the other hand (Fig. 29, red open symbols). In this comparison we report, for the ACT clusters (open squares), the so-called UPP (Universal Pressure Profile) masses given in Hasselfield et al. (2013).

The range of redshifts covered by the *Planck* SZ sample, from $z = 0.01$ to about 1 with 67% of the clusters lying below $z = 0.3$, is quite complementary to the high redshift range explored by ACT and in by SPT. For the comparison of the mass distribution we take advantage of our newly-proposed SZ-mass estimate, derived from Y_z, which provides us with a homogeneous definition of the masses over the whole range of *Planck* SZ clusters with measured redshifts. The *Planck* clusters populate the full redshift range and they quite nicely fill a unique space of massive, $M \geq 5\times10^{14}\,\mathrm{M}_\odot$, and high redshift $z \geq 0.5$ clusters, as shown in Fig. 29. This contrasts with the SZ clusters detected in 720 square degrees of SPT observations and those of ACT observations, which are dominated, as shown in Fig. 29 left panel, by lower-mass higher-redshift clusters (up to $z \sim 1.3$). The combination of *Planck* and SPT/ACT catalogues samples the *M–z* space in a complementary manner. Clearly the all-sky nature of the *Planck* makes the most massive clusters preferentially accessible to *Planck* whereas the highest redshift clusters, $z \geq 1$, are accessible to SPT.

Very few massive high-redshift clusters exist in the X-ray catalogues, as seen in Fig. 29 (right panel open blue squares). The all-sky NORAS/REFLEX catalogues (Böhringer et al. 2000, 2004) are limited to $z = 0.45$, a result of the $(1+z)^4$ surface brightness dependence of the X-ray detection limit (Fig. 29, right panel solid green line). The smaller-area MACS sample, based on systematic follow-up of *ROSAT* bright sources (Ebeling

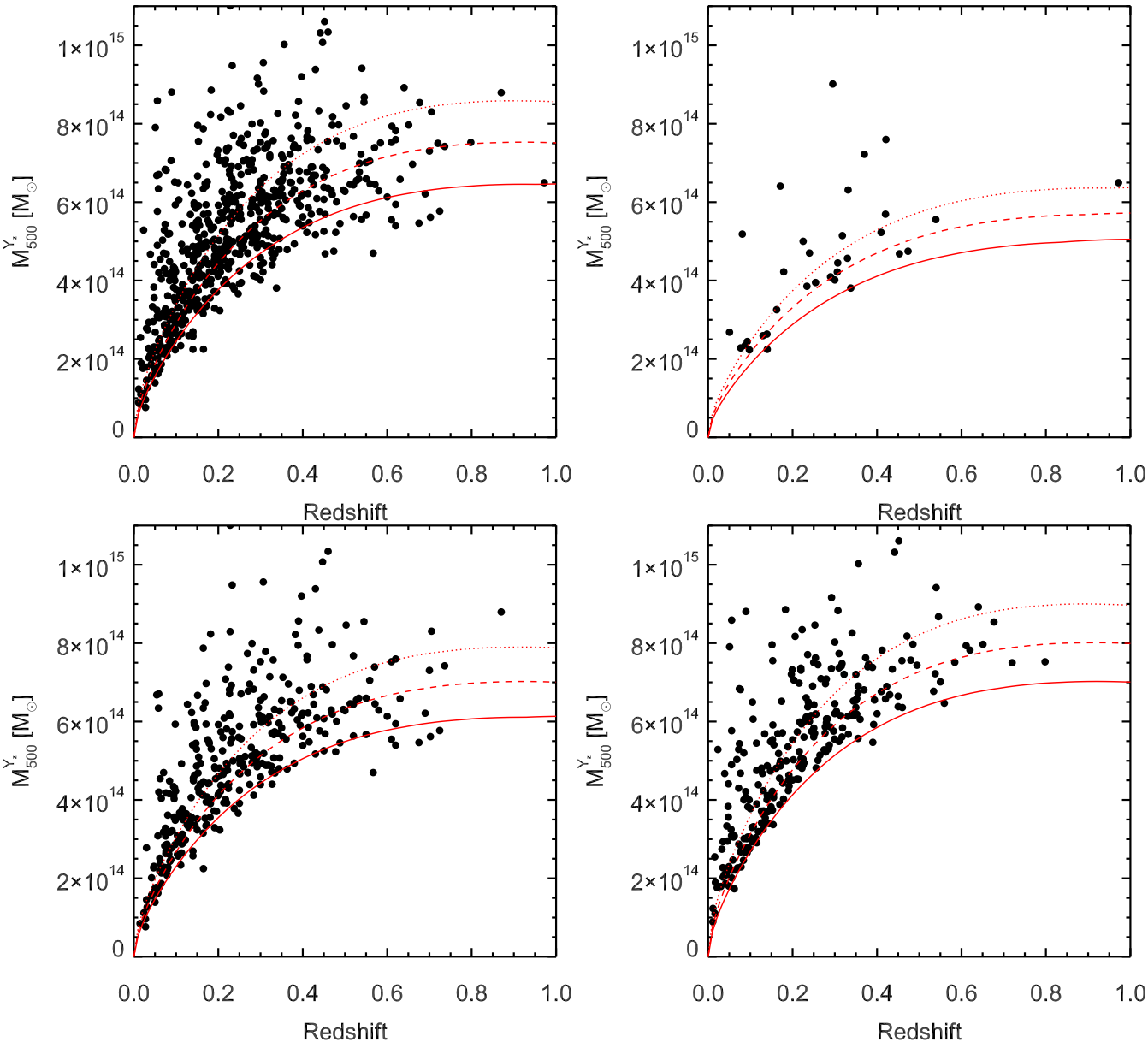

Fig. 28: Mass limit illustrated for SZ detections by MMF3 algorithm. *Upper left:* average mass limit computed from the average noise over the sky. *Upper right:* same for the deep survey zone corresponding to 2.7% sky coverage centred at the Ecliptic polar regions. *Lower left:* same for the medium-deep survey area covering 41.3% of the sky. *Lower right:* same for the shallow-survey area covering 56% of the sky. In each panel, only detections in the corresponding areas are plotted. The lines dotted, dashed and solid lines show the *Planck* mass limit at 80, 50 and 20% completeness, respectively.

et al. 2007), contains a dozen clusters at $z \geq 0.5$. The 400SD sample (Burenin et al. 2007), based on serendipitous detections in 400 deg^2 of ROSAT pointed observations, contains only two clusters with $M \geq 5 \times 10^{14}\,M_\odot$ and $z \geq 0.5$. Finally, only a couple of clusters in the range $M \geq 5 \times 10^{14}\,M_\odot$ are found in the *XMM-Newton* based serendipitous cluster samples (XCS, Mehrtens et al. (2012); XMM-LSS, Pacaud et al. (2007); XDCP, Fassbender et al. (2011)). By contrast to an X-ray selected cluster catalogue, the *Planck* detection-limit, illustrated for the medium-deep survey zone and shown in Fig. 29 (right panel solid black line), has a much shallower dependence on redshift and is quasi-redshift independent above $z = 0.4$. The difference in cluster selection starts at redshifts $z \geq 0.2$. As a result of the quasi-redshift independent mass-selection of SZ surveys, *Planck* probes deeper than the X-ray selection. This is also seen in the overall distribution of redshifts of the *Planck* clusters, Fig. 24.

This leaves the *Planck* SZ catalogue as the deepest all-sky catalogue spanning the broadest cluster mass range from 0.1 to $1.6 \times 10^{15}\,M_\odot$, and particularly adapted to the detection of rare very massive clusters in the tail of the distribution in the range $M \geq 5 \times 10^{14}\,M_\odot$ and $z \geq 0.5$.

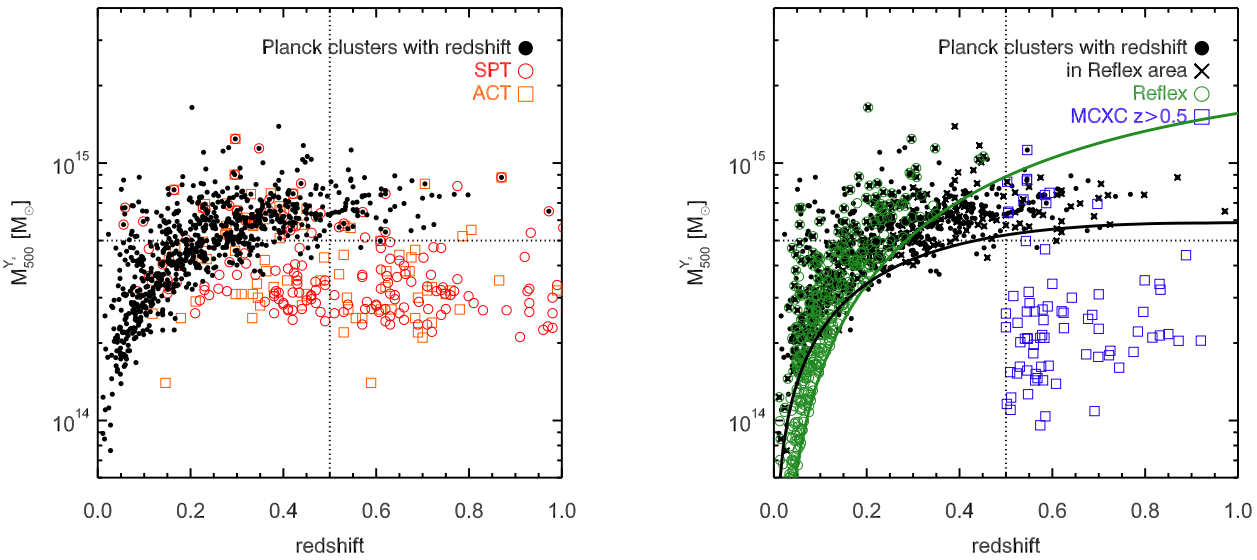

Fig. 29: *Left panel:* distribution in the *M*–*z* plane of the *Planck* clusters (filled circles) compared with the SPT clusters (open light red circles) from Reichardt et al. (2013) and ACT catalogue (open red squares) from Hasselfield et al. (2013). *Right panel:* distribution in the *M*–*z* plane of the *Planck* clusters (black symbols) as compared to the clusters from the REFLEX catalogue (green open circles) Böhringer et al. (2004). The black crosses indicate the *Planck* clusters in the REFLEX area. The open blue squares represent clusters from the MCXC catalogue with redshifts above $z = 0.5$. The green solid line shows the REFLEX detection limit whereas the black solid line shows the *Planck* mass limit for the medium-deep survey zone at 20% completeness.

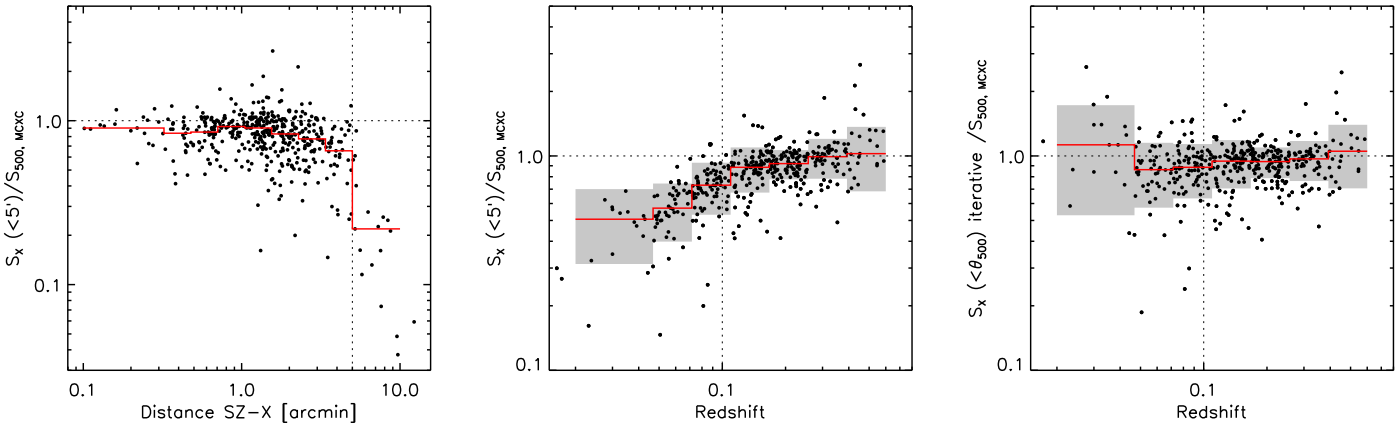

Fig. 30: Ratio between RASS flux, computed in an aperture of five arcmin in radius centred on the *Planck* position, and MCXC value for *Planck* candidates identified with MCXC clusters. The fluxes are computed in the [0.1–2.4] keV band at Earth and corrected for absorption. S_{500} is the flux corresponding to the luminosity within R_{500} published in the MCXC catalogue. *Left panel:* the ratio is plotted as a function of distance between the *Planck* and X-ray positions; *Middle panel:* same, as a function of cluster redshift, for distances smaller than five arcmin; *Right panel:* same as middle panel, for RASS flux within R_{500} derived from the aperture flux, using the MCXC iterative procedure based on the L_{500}–M_{500} relation and the REXCESS gas density profile (Piffaretti et al. 2011). The red line is the median ratio in distance or redshift bins with the grey area corresponding to $\pm 1\,\sigma$ standard deviation in each bin.

7.4. X-ray flux of the Planck clusters and candidates

For all *Planck* SZ detections, we estimated the unabsorbed fluxes at Earth in the [0.1–2.4] keV band (as in the MCXC) measured in an aperture of five arcmin. The aperture is centred on the *Planck* candidate position, except for candidates associated with a BSC source, for which we adopt the X-ray position, since the BSC source is very likely the counterpart (Planck Collaboration Int. IV 2013). The conversion between the RASS count rate in the hard band and flux is performed using an absorbed thermal emission model with the $N_{\rm H}$ value fixed to the 21 cm value. The conversion depends weakly on temperature and redshift and we assumed typical values of $kT = 6$ keV and $z = 0.5$. Planck Collaboration Int. IV (2013) compared such flux estimates with precise *XMM-Newton* fluxes measured within R_{500}, S_{500}, for candidates confirmed with the *XMM-Newton* follow-up programme. These clusters lie in the range $0.1 < z < 0.9$ and the $0.3 \times 10^{-12} < S_{500} < 6 \times 10^{-12}$ erg s^{-1} cm^{-2} flux range. The RASS aperture fluxes were found to underestimate the "true" flux by about 30 %.

Figure 30 extends this comparison further to all the *Planck* SZ detections identified with MCXC clusters. Piffaretti et al.

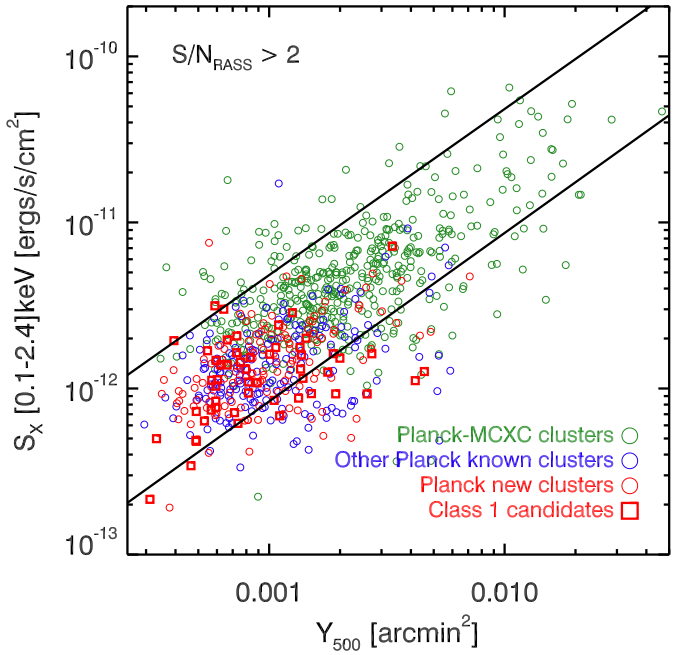

Fig. 31: X-ray unabsorbed flux versus SZ flux. For *Planck* SZ detections identified with MCXC clusters (open green circles), the X-ray flux is estimated from L_{500}. For other *Planck* SZ detections, the flux is derived from RASS count-rate in a five-arcmin aperture (see Sect. 4.1.1). *Planck* new clusters and CLASS1 candidates are shown as open red circles and squares, respectively. The two lines corresponds to the expected L_{500}–Y_{500} relation (Arnaud et al. 2010) at $z = 0.01$ and $z = 1$, respectively.

(2011) published homogenized L_{500} and R_{500} values derived from the flux given in the original catalogues in various apertures, using an iterative procedure based on the REXCESS L_{500}–M_{500} relation and gas density profile shape. We simply computed S_{500} from L_{500}, taking into account the K-correction at the cluster redshift, but neglecting its variation with temperature.

Although derived from *ROSAT* survey data as our present flux estimate, S_{500} values from the MCXC are expected to be more accurate due to: (i) optimum choice of the X-ray centre; (ii) higher S/N detection; (iii) more sophisticated flux extraction adapted to data quality and source extent (e.g., growth curve analysis); and (iv) use of R_{500} rather than a fixed aperture. Not surprisingly, the ratio between the present flux estimate and the MCXC value decreases with increasing offset between the *Planck* position and X-ray position (Fig. 30, left panel). The ratio drops dramatically when the distance is larger than five arcmin, i.e., when the X-ray peak lies outside the integration aperture. Those are rare cases, 18 nearby clusters ($z < 0.1$ with a median value of $z = 0.05$), for which a physical offset likely contributes to the overall offset. When these cases are excluded, the median ratio is 0.85 and depends on redshift (Fig. 30, middle panel); it significantly decreases with decreasing redshift below z of 0.1. The median ratio is 0.65 and 0.92, with a standard deviation of 0.10 and 0.15 dex, below and above $z = 0.1$, respectively. This is mostly due to the choice of a fixed aperture that becomes too small as compared to R_{500} at low z. If we apply the same iterative procedure used by Piffaretti et al. (2011) to estimate S_{500} from the aperture flux, the resulting value is consistent on average with the MCXC value at all redshifts (Fig. 30, right panel). The dispersion is slightly increased. The aperture unabsorbed fluxes are thus reliable estimates of the X-ray fluxes above $z > 0.1$ on average.

Figure 31 shows the X-ray flux as function of Y_{500} for *Planck* candidates identified with known clusters, for the confirmed new *Planck* clusters and for the CLASS1 candidates. For *Planck* detections identified with MCXC clusters we plot the more precise published S_{500} value. All three categories of sources behave in a similar manner in good agreement with the range of redshifts probed by the sample. In this respect CLASS1 candidates do not exhibit any departure with respect to the known or confirmed clusters. We provide the X-ray fluxes for the *Planck* clusters and candidates that are not identified with MCXC clusters (see Appendix C and Table C.1). For the *Planck* cluster with MCXC identifier, we refer the reader to the RASS catalogue outputs or to the homogenized MCXC meta-catalogue. The main limitation of the aperture unabsorbed fluxes is the statistical precision on the RASS estimate (most of the *Planck* SZ detections not identified with MCXC clusters have low $(S/N)_{RASS}$ values) and the relatively large scatter (±30% standard deviation). For $z < 0.1$ clusters, and if the RASS detection is reasonably good a more precise procedure is recommended, such as an adapted growth curve analysis, on a case-by-case basis.

7.5. Scaling relations between SZ and X-ray quantities

A fundamental scaling relation is that between Y_{500} and its X-ray analogue, Y_X. Introduced by Kravtsov et al. (2006), Y_X is the product of $M_{g,500}$, the gas mass within R_{500}, and T_X, the spectroscopic temperature outside the core [25]. From the fact that the gas density profile used to compute $M_{g,500}$ is derived from deprojection of the X-ray surface brightness profile, and that the X-ray emission depends on the square of the density, the ratio of these two quantities is

$$\frac{D_A^2\, Y_{500}}{C_{XSZ}\, Y_X} = \frac{1}{Q}\frac{\langle n_e T\rangle_{R_{500}}}{\langle n_e\rangle_{R_{500}} T_X} \qquad (6)$$

$$Q = \frac{\sqrt{\langle n_e^2\rangle_{dr}}}{\langle n_e\rangle_{dr}},$$

where the angle brackets denote volume-averaged quantities, and Q is the clumpiness factor at the scale of the radial bins used to derive the density profile. The numerical constant $C_{XSZ} = \sigma_T/(m_e\, c^2\, \mu_e\, m_p) = 1.416 \times 10^{-19}\,\mathrm{Mpc^2\,(M_\odot\,keV)^{-1}}$. The ratio thus depends only on the internal structure of the intra-cluster medium.

The properties of the Y_X–Y_{500} relation, in particular its variation with mass and redshift and the dispersion about the mean relation, are important probes of the physics of cluster formation.

7.5.1. Data set

Here we extend the study of a sample of 62 clusters from the *Planck*–ESZ sample with good quality *XMM-Newton* archive data presented in Planck Collaboration XI (2011, hereafter PEPXI). This study found $D_A^2\, Y_{500}/C_{XSZ}\, Y_X = 0.95 \pm 0.03$, in a good agreement with REXCESS prediction, 0.924 ± 0.004, of Arnaud et al. (2010).

All 62 objects in the PEPXI sample are included in the present catalogue. We further add 40 clusters from the catalogue, including nine additional objects from the *XMM-Newton*

[25] Here we use the temperature measured in the [0.15–0.75] R_{500} aperture.

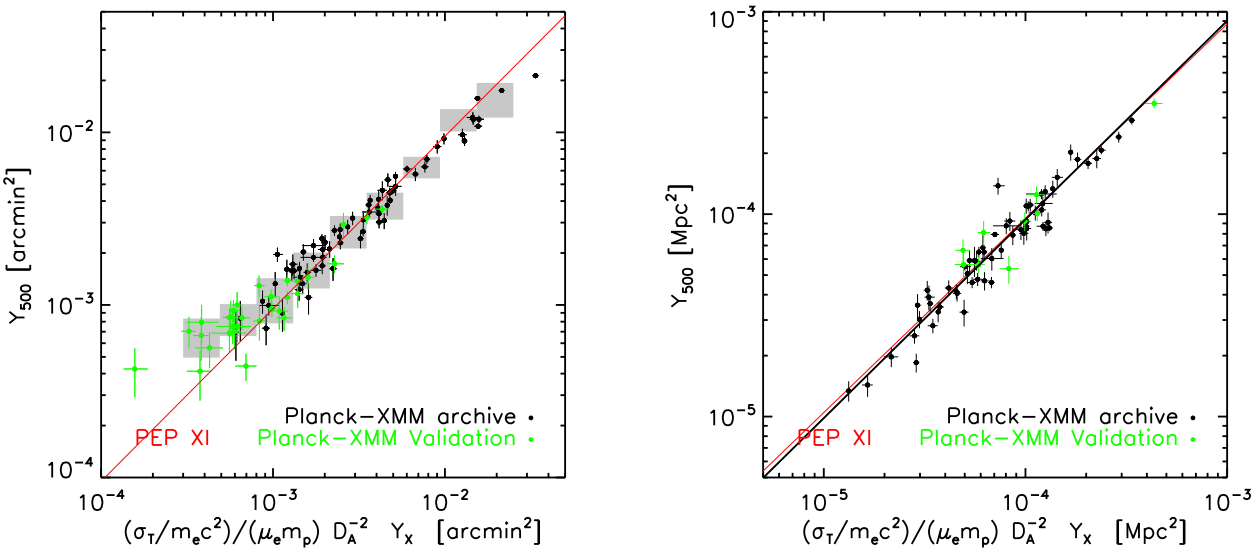

Fig. 32: Relation between the Comptonization parameters Y_{500}, and the normalized Y_X parameter for a sub-sample of the present catalogue. Black points show clusters in the *Planck*-ESZ sample with *XMM-Newton* archival data presented by Planck Collaboration XI (2011) and additional LoCuSS clusters studied by Planck Collaboration Int. III (2013). Green points represent new *Planck* clusters confirmed with *XMM-Newton* (Planck Collaboration IX 2011; Planck Collaboration Int. I 2012; Planck Collaboration Int. IV 2013). The red line denotes the scaling relations of Planck Collaboration XI (2011). *Left panel:* relation in units of arcmin^2 where Y_{500} is extracted using the Arnaud et al. (2010) pressure profile. The grey area corresponds to median Y_{500} values in Y_X bins with $\pm\sigma$ standard deviation. *Right panel:* scaling relation between the intrinsic Compton parameter, $D_A^2 Y_{500}$, and Y_X for the sub-sample of S/N > 7 clusters used in the cosmological analysis. The data are corrected for Malmquist bias, and Y_{500} is extracted using the *Planck* pressure profile (see text). The black line is the best-fit power-law relation.

Table 6: The Y_{500}–Y_X relation. Column(1): sample under consideration; Column(2): Malmquist bias correction; Column (3): Pressure profile shape used in Y_{500} extraction; Column (4): number of clusters in the sample; Column (5-6) Slope and normalization of the best-fit relation expressed as $Y_{500}/Y_p = A\,(Y_X/Y_p)^\alpha$, using BCES orthogonal regression. The pivot is $Y_p = 10^{-4}$Mpc^2; Column (7-8) Intrinsic and raw scatter around the best-fit relation; Column (9): mean ratio in logarithm, $\Delta(\log(Q))=\log(Y_{500}/Y_X)$; Column (10-11): corresponding intrinsic scatter and raw scatter. The scatters are error-weighted values. The best estimate is indicated in bold face. The last line gives the REXCESS prediction (Arnaud et al. 2010).

Data				Power-law Fit				Mean ratio		
Sample	MB	P Profile	N_c	$A\times10^2$	α	$\sigma_{\log}^{\rm int}\times10^2$	$\sigma_{\log}^{\rm raw}\times10^2$	$\Delta\,log(Q)$	$\sigma_{\rm int}\times10^2$	$\sigma_{\rm raw}\times10^2$
PEPXI	N	A10	62	-2.0 ± 1.0	0.960 ± 0.040	10.0 ± 1.0	-	-0.022 ± 0.014	...	...
ESZ	N	A10	62	-2.2 ± 1.1	0.966 ± 0.034	7.2 ± 1.1	8.2 ± 1.0	-0.023 ± 0.011	7.3 ± 1.1	8.5
ESZ	Y	A10	62	-3.0 ± 1.1	0.975 ± 0.035	7.1 ± 1.1	8.2 ± 1.0	-0.031 ± 0.011	7.2 ± 1.1	8.4
S/N > 7	Y	A10	78	-2.4 ± 1.0	0.972 ± 0.029	6.9 ± 1.1	8.1 ± 0.9	-0.024 ± 0.010	6.9 ± 1.0	8.3
Cosmo	Y	A10	71	-1.9 ± 1.1	0.990 ± 0.032	7.2 ± 1.2	8.3 ± 1.0	-0.021 ± 0.010	6.9 ± 1.0	8.3
Cosmo	Y	A10+err	71	-1.9 ± 1.1	0.987 ± 0.031	6.3 ± 1.1	7.9 ± 0.9	-0.019 ± 0.010	6.5 ± 1.1	8.2
Cosmo	**Y**	**PIP-V**	**71**	$\mathbf{-2.6\pm1.0}$	$\mathbf{0.981\pm0.027}$	$\mathbf{6.6\pm1.2}$	$\mathbf{7.8\pm1.0}$	$\mathbf{-0.027\pm0.010}$	$\mathbf{6.6\pm1.0}$	**8.0**
REXCESS	X-ray prediction							-0.034 ± 0.002		

archival study of *Planck*-detected LoCuSS systems presented by Planck Collaboration Int. III (2013), and the 31 *Planck*-discovered clusters with good redshift estimates ($Q_z = 2$) confirmed with the *XMM-Newton* (Planck Collaboration IX 2011; Planck Collaboration Int. I 2012; Planck Collaboration Int. IV 2013). The total sample thus consists of 102 clusters.

For each object, Y_X and the corresponding R_{500} value were estimated simultaneously by iteration about the M_{500}–Y_X relation of Arnaud et al. (2010),

$$E^{2/5}(z)M_{500} = 10^{14.567}\left[\frac{Y_X}{2\times10^{14}\,M_\odot\,\mathrm{keV}}\right]^{0.561} M_\odot\,. \quad (7)$$

In the present study, we focus on the physical relation between Y_{500} and Y_X. While these quantities must be estimated within the same radii, the exact value of R_{500} is irrelevant as the radial dependence of the Y_{500}/Y_X ratio is negligible. We thus propagated only the measurement uncertainties on the temperature and gas mass profiles, fixing the aperture to R_{500}. We ignored the statistical and systematic uncertainties on the M_{500}–Y_{500} relation itself.[26] Similarly Y_{500} was re-extracted at the X-ray position with size fixed to X-ray size. Its uncertainty corresponds to the statistical error on the SZ signal. The results are summarized Table 6, with the best estimate indicated in bold face.

[26] These must however be taken into account when using Y_{500} or Y_X as a mass proxy, e.g., when calibrating the Y_{500}–M_{500} relation from combining the M_{500}–Y_X relation and the relation between Y_{500} and Y_X (or equivalently M_{500}). This calibration is extensively addressed in the Planck Collaboration XX (2013).

7.5.2. The best-fit Y_{500}–Y_X relation

The Y_{500}–Y_X scaling relation for the full sample is shown in units of arcmin^2 in Fig. 32. At high flux the points follow the PEP XI relation. The slope and normalization are determined at slightly higher precision, due to the better quality SZ data. The derived intrinsic scatter (Table 6) is significantly smaller, a consequence of the propagation of gas mass profile errors in the Y_X error budget, which was neglected in our earlier study.

The relation levels off at around $Y_X = 5\times10^{-4}$ arcmin^2, with a bin average deviation increasing with decreasing Y_X (Fig. 32 left panel). This is an indication of Malmquist bias, as noted by Planck Collaboration Int. I (2012). Full correction of this bias when fitting scaling relations involves drawing mock catalogues according to the cluster mass function, to which the sample selection criteria are then applied. The present sample is a small subset of the full S/N $\geq$ 4.5 *Planck* catalogue and thus such a procedure cannot be applied. To minimize bias effects we will only consider high S/N detections, S/N > 7. To correct for the residual bias, we adapted the approach proposed by Vikhlinin et al. (2009). Before fitting the Y_{500}–Y_X relation, each individual Y value was divided by the mean bias, b, given by

$$\ln b = \frac{\exp\left(-x^2/2\sigma^2\right)}{\sqrt{\pi/2}\,\mathrm{erfc}\left(x/\sqrt{2}\sigma\right)}\,\sigma\,, \tag{8}$$

where $x = -\log(Y/Y_{\rm min})$, $Y_{\rm min}$ being the flux threshold corresponding to the signal-to-noise cut, $(\mathrm{S/N})_{\rm cut}$. At the location of the cluster, $Y/Y_{\rm min} = (\mathrm{S/N})/(\mathrm{S/N})_{\rm cut}$. Here σ is the log-normal dispersion at fixed Y_X. We took into account both the intrinsic dispersion $\sigma_{\rm int}$, estimated iteratively, and the statistical dispersion, given by $\sigma = \sqrt{\ln\left[((\mathrm{S/N})+1)/(\mathrm{S/N})\right]^2 + [\ln 10\,\sigma_{\rm int}]^2}$. The correction decreases the effective Y_{500} values at a given Y_X, an effect that is larger for clusters closer to the S/N threshold; i.e., low-flux objects. The net effect on the scaling relation is small, giving a $0.7\,\sigma$ decrease of the normalization and a slight steepening of the power-law slope (Table 6).

The slope and normalization of the relation are robust to the inclusion of newly-discovered *Planck* clusters. The results derived from the extended sample of 78 clusters with S/N > 7 agree with those obtained for the updated XMM-ESZ sample within $0.5\,\sigma$ (Table 6). They are also in agreement with the subsample of 71 S/N > 7 clusters included in the cosmological sample discussed by Planck Collaboration XX (2013). We measured a significant intrinsic scatter of $\sigma_{\rm int} = 0.07 \pm 0.01$ dex. There is one spectacular outlier with an Y_{500}/Y_X ratio nearly twice as big as the mean. This is the *Planck* ESZ cluster identified with A2813 or RXC J0043.4-2037 in the REFLEX catalogue, located at $z = 0.29$. Its high ratio is very puzzling. It cannot result from an inaccurate redshift measurement, as this is based on spectroscopic data for several cluster galaxies (Böhringer et al. 2004). There is no evidence of a peculiar dynamical state from the X-ray morphology, and there is no evidence of contamination in the SZ data.

Part of the dispersion could be due to the use of an inappropriate fixed pressure profile in the Y_{500} extraction. When including possible errors on Y_{500} due to dispersion around the mean Arnaud et al. (2010) profile, the scatter is decreased to $\sigma_{\rm int} = 0.06$, a decrease at the $1\,\sigma$ level. To further assess the effect of the choice of the pressure profile, we re-extracted the SZ signal using the *Planck*+*XMM-Newton* profile shape measured for ESZ clusters by Planck Collaboration Int. V (2013, hereafter PIPV). Individual profiles are used for *Planck* ESZ clusters, and the mean profile is used for the other clusters. This should give the most reliable estimate of the Y_{500}–Y_X relation, since it is based directly on measured profile shapes. In this case, the slope and scatter remain unchanged but the normalization is slightly decreased (at the $0.5\,\sigma$ level). This is a result of the more inflated nature of the PIPV profile as compared to the Arnaud et al. (2010) REXCESS profile. The relation derived using PIPV pressure profiles is plotted in the right-hand panel of Fig. 32 together with the corresponding data points.

The relation does not exhibit significant evidence of variance of the Y_{500}/Y_X ratio with mass, the slope is consistent with unity, as expected from strong self-similarity of pressure profile shape. However, we found an intrinsic scatter about three times larger than the results of Kay et al. (2012). Partly this is due to the presence of outliers in our data set (as discussed above), or it may be due to projection effects in observed data sets (Kay et al. 2012). The mean ratio is very well constrained with a precision of 2.5%, $\log(Y_{500}/Y_X) = -0.027 \pm 0.010$. This confirms at higher precision the strong agreement between the SZ and X-ray measurements (within R_{500}) of the intra-cluster gas properties found by PEP XI and other studies (Andersson et al. 2011; Sifon et al. 2012; Marrone et al. 2012; Rozo et al. 2012). The ratio is perfectly consistent with the X-ray prediction, suggesting that the clumpiness must be low. However there are still large systematics that are discussed in Appendix D.

8. Summary

Planck's all-sky coverage and broad frequency range are designed to detect the SZ signal of galaxy clusters across the sky. We provide, from the first 15.5 months of observations, the largest ensemble of SZ-selected sources detected from an all-sky survey. The *Planck* catalogue of SZ sources contains 1227 detections. This catalogue, statistically characterized in terms of completeness and statistical reliability, was validated using external X-ray and optical/NIR data, alongside a multi-frequency follow-up programme for confirmation. A total of 861 SZ detections are confirmed associations with bona fide clusters, of which 178 are brand-new clusters. The remaining cluster candidates are divided into three classes according to their reliability, i.e., the quality of evidence that they are likely to be bona fide clusters.

A total of 813 *Planck* clusters have measured redshifts ranging from $z = 0.01$ to order one, with one-third of the clusters lying above $z = 0.3$. The brand-new *Planck* clusters extend the redshift range above $z = 0.3$. For all the *Planck* clusters with measured redshift, a mass can be estimated from the Compton Y measure. We provide a homogeneous mass estimate ranging from $(0.1 \text{ to } 1.6)\times10^{15}\,\mathrm{M}_\odot$. Except at low redshifts, the *Planck* cluster distribution exhibits a nearly redshift-independent mass limit and occupies a unique region in the M–z space of massive, $M \geq 5\times10^{14}\,\mathrm{M}_\odot$, and high-redshift ($z \geq 0.5$) clusters. Owing to its all-sky nature, *Planck* detects new clusters in a region of the mass–redshift plane that is sparsely populated by the RASS catalogues. It detects the rarest clusters, i.e., the most massive clusters at high redshift in the exponential tail of the cluster mass function that are the most useful clusters for cosmological studies. With the presently confirmed *Planck* SZ detections, *Planck* doubles the number of massive clusters above redshift 0.5, as compared to other surveys. The *Planck* SZ catalogue is, and will be for years to come, the deepest all-sky SZ catalogue spanning the broadest cluster mass range.

The *Planck* SZ catalogue should motivate multi-wavelength follow-up efforts. The confirmation of the cluster candidates

will reveal clusters at higher redshifts than the present distribution. Such follow-up efforts will further enhance the value of the *Planck* SZ catalogue as the first all-sky SZ selected catalogue. It will serve as a reference for studies of cluster physics (e.g., galaxy properties versus intra-cluster gas physics, dynamical state, evolution, etc.). Using an extended sub-sample of the *Planck* SZ clusters with high-quality *XMM-Newton* data, the scaling relations between SZ and X-ray properties were reassessed and updated. With better-quality data and thus higher precision, we show excellent agreement between SZ and X-ray measurements of the intra-cluster gas properties. We have thus derived a new up-to-date reference calibrated local relation between Y and Y_X.

The *Planck* SZ catalogue will also serve to define samples for cosmological studies. A first step in this direction is already taken in Planck Collaboration XX (2013), where an analysis of the SZ cluster abundance to constrain the cosmological parameters is performed using a sub-sample selected from the PSZ catalogue consisting of 189 clusters detected above a signal-to-noise ratio of 7 with measured redshifts. The value-added information derived from the validation of the *Planck* SZ detections, in particular the SZ-based mass estimate, increases even further the value of the *Planck* SZ catalogue.

The combination of the *Planck* all-sky SZ data with near future and planned observations of the large-scale structure by surveys such as PAN-STARRS, LOFAR, Euclid, LSST, and RSG/e-ROSITA will revolutionize our understanding of large-scale structure formation and evolution.

Acknowledgements. The development of *Planck* has been supported by: ESA; CNES and CNRS/INSU-IN2P3-INP (France); ASI, CNR, and INAF (Italy); NASA and DoE (USA); STFC and UKSA (UK); CSIC, MICINN, JA and RES (Spain); Tekes, AoF and CSC (Finland); DLR and MPG (Germany); CSA (Canada); DTU Space (Denmark); SER/SSO (Switzerland); RCN (Norway); SFI (Ireland); FCT/MCTES (Portugal); and PRACE (EU). A description of the *Planck* Collaboration and a list of its members, including the technical or scientific activities in which they have been involved, can be found at http://www.sciops.esa.int/index.php?project=planck&page=Planck_Collaboration. The authors thank N. Schartel, ESA *XMM-Newton* project scientist, for granting the Director Discretionary Time used for confirmation of SZ *Planck* candidates. The authors thank TUBITAK, IKI, KFU and AST for support in using RTT150 (Russian-Turkish 1.5-m telescope, Bakyrlytepe, Turkey); in particular we thank KFU and IKI for providing significant amount of their observing time at RTT150. We also thank BTA 6-m telescope Time Allocation Committee (TAC) for support of optical follow-up project. The authors acknowledge the use of the INT and WHT telescopes operated on the island of La Palma by the Isaac Newton Group of Telescopes at the Spanish Observatorio del Roque de los Muchachos of the Instituto de Astrofísica de Canarias (IAC); the Nordic Optical Telescope, operated on La Palma jointly by Denmark, Finland, Iceland, Norway, and Sweden, at the Spanish Observatorio del Roque de los Muchachos of the IAC; the TNG telescope, operated on La Palma by the Fundacion Galileo Galilei of the INAF at the Spanish Observatorio del Roque de los Muchachos of the IAC; the GTC telescope, operated on La Palma by the IAC at the Spanish Observatorio del Roque de los Muchachos of the IAC; and the IAC80 telescope operated on the island of Tenerife by the IAC at the Spanish Observatorio del Teide of the IAC. Part of this research has been carried out with telescope time awarded by the CCI International Time Programme. The authors thank the TAC of the MPG/ESO-2.2m telescope for support of optical follow-up with WFI under *Max Planck* time. Observations were also conducted with ESO NTT at the La Silla Paranal Observatory. This research has made use of SDSS-III data. Funding for SDSS-III http://www.sdss3.org/ has been provided by the Alfred P. Sloan Foundation, the Participating Institutions, the National Science Foundation, and DoE. SDSS-III is managed by the Astrophysical Research Consortium for the Participating Institutions of the SDSS-III Collaboration.
This research has made use of the following databases: the NED and IRSA databases, operated by the Jet Propulsion Laboratory, California Institute of Technology, under contract with the NASA; SIMBAD, operated at CDS, Strasbourg, France; SZ repository operated by IAS Data and Operation Center (IDOC) under contract with CNES and CNRS. The authors acknowledge the use of software provided by the US National Virtual Observatory.

References

Abdo, A. A., Ackermann, M., Ajello, M., et al. 2010, ApJ, 715, 429
Abell, G. O. 1958, ApJS, 3, 211
Abell, G. O., Corwin, Jr., H. G., & Olowin, R. P. 1989, ApJS, 70, 1
Afanasiev, V. L. & Moiseev, A. V. 2005, Astronomy Letters, 31, 194
Aghanim, N., da Silva, A. C., & Nunes, N. J. 2009, A&A, 496, 637
Aghanim, N., de Luca, A., Bouchet, F. R., Gispert, R., & Puget, J. L. 1997, A&A, 325, 9
Aghanim, N. & Fromenteau, S. 2013, A&A
Aghanim, N., Hansen, S. H., & Lagache, G. 2005, A&A, 439, 901
Akritas, M. G. & Bershady, M. A. 1996, ApJ, 470, 706
Allen, S. W., Evrard, A. E., & Mantz, A. B. 2011, ARA&A, 49, 409
AMI Consortium, Hurley-Walker, N., Brown, M. L., et al. 2011, MNRAS, 414, L75
AMI Consortium, Zwart, J. T. L., Barker, R. W., et al. 2008, MNRAS, 391, 1545
Andersson, K., Benson, B. A., Ade, P. A. R., et al. 2011, ApJ, 738, 48
Angulo, R. E., Springel, V., White, S. D. M., et al. 2012, MNRAS, 426, 2046
Arnaud, M., Pointecouteau, E., & Pratt, G. W. 2005, A&A, 441, 893
Arnaud, M., Pratt, G. W., Piffaretti, R., et al. 2010, A&A, 517, A92
Arnaud, M., XX, x., YY, y., & ZZ, z. 2013, A&A
Aussel, H., Pratt, G., & Arnaud, M. 2013, A&A
Bajkova, A. T. 2005, Astronomy Reports, 49, 947
Barbosa, D., Bartlett, J. G., Blanchard, A., & Oukbir, J. 1996, A&A, 314, 13
Belsole, E., Birkinshaw, M., & Worrall, D. M. 2005, MNRAS, 358, 120
Benítez, N. 2000, ApJ, 536, 571
Bertin, E. & Arnouts, S. 1996, A&AS, 117, 393
Bock, D., Large, M. I., & Sadler, E. M. 1999, AJ, 117, 1578
Böhringer, H., Schuecker, P., Guzzo, L., et al. 2004, A&A, 425, 367
Böhringer, H., Schuecker, P., Pratt, G. W., et al. 2007, A&A, 469, 363
Böhringer, H., Voges, W., Huchra, J. P., et al. 2000, ApJS, 129, 435
Borgani, S. & Kravtsov, A. 2009, ArXiv e-prints
Borgani, S., Murante, G., Springel, V., et al. 2004, MNRAS, 348, 1078
Burenin, R. A., Vikhlinin, A., Hornstrup, A., et al. 2007, ApJS, 172, 561
Carvalho, P., Rocha, G., & Hobson, M. P. 2009, MNRAS, 393, 681
Carvalho, P., Rocha, G., Hobson, M. P., & Lasenby, A. 2011, ArXiv e-prints
Chon, G. & Böhringer, H. 2012, A&A, 538, A35
Condon, J. J., Cotton, W. D., Greisen, E. W., et al. 1998, AJ, 115, 1693
Crawford, C. S., Allen, S. W., Ebeling, H., Edge, A. C., & Fabian, A. C. 1999, MNRAS, 306, 857
Cunha, C. E., Lima, M., Oyaizu, H., Frieman, J., & Lin, H. 2009, MNRAS, 396, 2379
da Silva, A. C., Kay, S. T., Liddle, A. R., & Thomas, P. A. 2004, MNRAS, 348, 1401
Ebeling, H., Barrett, E., Donovan, D., et al. 2007, ApJ, 661, L33
Eckert, D., Molendi, S., & Paltani, S. 2011, A&A, 526, A79
Fabian, A. C. 2012, ARA&A, 50, 455
Fassbender, R., Böhringer, H., Nastasi, A., et al. 2011, New Journal of Physics, 13, 125014
Fromenteau, S., Bartlett, J., & Mei, S. 2013, in prep.
Giles, P. A., Maughan, B. J., Birkinshaw, M., Worrall, D. M., & Lancaster, K. 2012, MNRAS, 419, 503
Gioia, I. M., Henry, J. P., Mullis, C. R., et al. 2003, ApJS, 149, 29
Hao, J., McKay, T. A., Koester, B. P., et al. 2010, The Astrophysical Journal Supplement Series, 191, 254
Hasselfield, M., Hilton, M., Marriage, T. A., et al. 2013, ArXiv e-prints
Herranz, D., Sanz, J. L., Hobson, M. P., et al. 2002, MNRAS, 336, 1057
Hlavacek-Larrondo, J., Fabian, A. C., Edge, A. C., et al. 2012, MNRAS, 421, 1360
Hudson, D. S., Mittal, R., Reiprich, T. H., et al. 2010, A&A, 513, A37
Hurier, G., Hildebrandt, S. R., & Macias-Perez, J. F. 2010, ArXiv e-prints
Johnston, D. E., Sheldon, E. S., Wechsler, R. H., et al. 2007, ArXiv e-prints
Kay, S. T., Peel, M. W., Short, C. J., et al. 2012, MNRAS, 422, 1999
Kepner, J., Fan, X., Bahcall, N., et al. 1999, ApJ, 517, 78
Koester, B. P., McKay, T. A., Annis, J., et al. 2007, ApJ, 660, 239
Kravtsov, A. V., Vikhlinin, A., & Nagai, D. 2006, ApJ, 650, 128
Li, C. & White, S. 2013, A&A
Lin, Y., Partridge, B., Pober, J. C., et al. 2009, ApJ, 694, 992
Lin, Y.-T., Stanford, S. A., Eisenhardt, P. R. M., et al. 2012, ApJ, 745, L3
Magliocchetti, M. & Brüggen, M. 2007, MNRAS, 379, 260
Mann, A. W. & Ebeling, H. 2012, MNRAS, 420, 2120
Mantz, A., Allen, S. W., Ebeling, H., Rapetti, D., & Drlica-Wagner, A. 2010, MNRAS, 406, 1773
Marrone, D. P., Smith, G. P., Okabe, N., et al. 2012, ApJ, 754, 119
Maughan, B. J., Giles, P. A., Randall, S. W., Jones, C., & Forman, W. R. 2012, MNRAS, 421, 1583
McNamara, B. R. & Nulsen, P. E. J. 2012, New Journal of Physics, 14, 055023
Mehrtens, N., Romer, A. K., Hilton, M., et al. 2012, MNRAS, 423, 1024

Melin, J., Bartlett, J. G., & Delabrouille, J. 2006, A&A, 459, 341
Melin, J.-B., Aghanim, N., Bartelmann, M., et al. 2012, ArXiv e-prints
Menanteau, F., González, J., Juin, J., et al. 2010, ApJ, 723, 1523
Mitra, S., Rocha, G., Górski, K. M., et al. 2011, ApJS, 193, 5
Montier, L. A., Pelkonen, V., Juvela, M., Ristorcelli, I., & Marshall, D. J. 2010, A&A, 522, A83+
Motl, P. M., Hallman, E. J., Burns, J. O., & Norman, M. L. 2005, ApJ, 623, L63
Muchovej, S., Leitch, E., Culverhouse, T., Carpenter, J., & Sievers, J. 2012, ApJ, 749, 46
Nagai, D. 2006, ApJ, 650, 538
Nagai, D., Kravtsov, A. V., & Vikhlinin, A. 2007, ApJ, 668, 1
Navarro, J. F., Frenk, C. S., & White, S. D. M. 1997, ApJ, 490, 493
Pacaud, F., Pierre, M., Adami, C., et al. 2007, MNRAS, 382, 1289
Peebles, P. J. E. 1980, The large-scale structure of the universe, ed. Peebles, P. J. E. (Princeton University Press)
Piffaretti, R., Arnaud, M., Pratt, G. W., Pointecouteau, E., & Melin, J.-B. 2011, A&A, 534, A109+
Piffaretti, R. & Valdarnini, R. 2008, A&A, 491, 71
Plagge, T., Benson, B. A., Ade, P. A. R., et al. 2010, ApJ, 716, 1118
Planck and AMI Collaborations. 2013, A&A, 550, A128
Planck Collaboration ES. 2013, The Explanatory Supplement to the Planck 2013 results (ESA)
Planck Collaboration I. 2013, In preparation
Planck Collaboration II. 2013, In preparation
Planck Collaboration Int. I. 2012, A&A, 543, A102
Planck Collaboration Int. III. 2013, A&A, 550, A129
Planck Collaboration Int. IV. 2013, A&A, 550, A130
Planck Collaboration Int. V. 2013, A&A, 550, A131
Planck Collaboration Int. VII. 2013, A&A, 550, A133
Planck Collaboration Int. X. 2013, Submitted to A&A
Planck Collaboration IX. 2011, A&A, 536, A9
Planck Collaboration VI. 2013, In preparation
Planck Collaboration VIII. 2011, A&A, 536, A8
Planck Collaboration X. 2011, A&A, 536, A10
Planck Collaboration XI. 2011, A&A, 536, A11
Planck Collaboration XII. 2013, In preparation
Planck Collaboration XIII. 2013, In preparation
Planck Collaboration XX. 2013, In preparation
Planck Collaboration XXI. 2013, In preparation
Planck Collaboration XXII. 2011, A&A, 536, A22
Planck Collaboration XXIII. 2011, A&A, 536, A23
Planck Collaboration XXVI. 2011, A&A, 536, A26
Planck Collaboration XXVIII. 2013, In preparation
Pratt, G. W., Croston, J. H., Arnaud, M., & Böhringer, H. 2009, A&A, 498, 361
Rafferty, D. A., McNamara, B. R., & Nulsen, P. E. J. 2008, ApJ, 687, 899
Rawle, T. D., Edge, A. C., Egami, E., et al. 2012, ApJ, 747, 29
Reichardt, C. L., Stalder, B., Bleem, L. E., et al. 2013, ApJ, 763, 127
Reichert, A., Böhringer, H., Fassbender, R., & Mühlegger, M. 2011, A&A, 535, A4
Reiprich, T. H. & Böhringer, H. 2002, ApJ, 567, 716
Remazeilles, M., Delabrouille, J., & Cardoso, J.-F. 2011, MNRAS, 410, 2481
Rozo, E., Rykoff, E. S., Evrard, A., et al. 2009, ApJ, 699, 768
Rozo, E., Vikhlinin, A., & More, S. 2012, ApJ, 760, 67
Rubiño-Martín, J. A. & Sunyaev, R. A. 2003, MNRAS, 344, 1155
Sayers, J., Czakon, N. G., Bridge, C., et al. 2012a, ApJ, 749, L15
Sayers, J., Czakon, N. G., Mantz, A., et al. 2012b, ArXiv e-prints
Schlegel, D. J., Finkbeiner, D. P., & Davis, M. 1998, ApJ, 500, 525
Schuecker, P., Böhringer, H., Collins, C. A., & Guzzo, L. 2003, A&A, 398, 867
SDSS-III Collaboration, :, Ahn, C. P., et al. 2012, ArXiv e-prints
Sifon, C., Menanteau, F., Hasselfield, M., et al. 2012, ArXiv e-prints
Story, K., Aird, K. A., Andersson, K., et al. 2011, ArXiv e-prints, arXiv:1102.2189
Sunyaev, R. A. & Zeldovich, I. B. 1980, ARA&A, 18, 537
Sunyaev, R. A. & Zeldovich, Y. B. 1972, Comments on Astrophysics and Space Physics, 4, 173
Szabo, T., Pierpaoli, E., Dong, F., Pipino, A., & Gunn, J. 2011, ApJ, 736, 21
Takey, A., Schwope, A., & Lamer, G. 2011, A&A, 534, A120
Tinker, J., Kravtsov, A. V., Klypin, A., et al. 2008, ApJ, 688, 709
Vanderlinde, K., Crawford, T. M., de Haan, T., et al. 2010, ApJ, 722, 1180
Vikhlinin, A., Allen, S. W., Arnaud, M., et al. 2009, in ArXiv Astrophysics e-prints, Vol. 2010, astro2010: The Astronomy and Astrophysics Decadal Survey, 304–+
Vikhlinin, A., Kravtsov, A., Forman, W., et al. 2006, ApJ, 640, 691
Vikhlinin, A., McNamara, B. R., Forman, W., et al. 1998, ApJ, 502, 558
Voges, W., Aschenbach, B., Boller, T., et al. 1999, A&A, 349, 389
Voges, W., Aschenbach, B., Boller, T., et al. 2000, VizieR Online Data Catalog, 9029, 0
Voit, G. M. 2005, Reviews of Modern Physics, 77, 207
Wen, Z. L., Han, J. L., & Liu, F. S. 2010, Monthly Notices of the Royal Astronomical Society, 407, 533
Wen, Z. L., Han, J. L., & Liu, F. S. 2012, ApJS, 199, 34
Wik, D. R., Sarazin, C. L., Ricker, P. M., & Randall, S. W. 2008, ApJ, 680, 17
Williamson, R., Benson, B. A., High, F. W., et al. 2011, ArXiv e-prints, arXiv:1101.1290
Wright, E. L., Eisenhardt, P. R. M., Mainzer, A. K., et al. 2010, AJ, 140, 1868
York, D. G., Adelman, J., Anderson, Jr., J. E., et al. 2000, AJ, 120, 1579
Zwicky, F., Herzog, E., & Wild, P. 1961, Catalogue of galaxies and of clusters of galaxies, Vol. I

Appendix A: Selection of Frequency Channel Maps

An assessment of which combination of *Planck* frequency channels to use was performed using the `MMF1` implementation of the matched multi-filter described in Sect. 2.2.2. The HFI and LFI channel maps were preprocessed as described in Sect. 2.1, with the only difference being that the point-source mask contained, in addition, detections from the LFI channel maps with S/N $\geq$ 10. Five different combinations of frequency channels were investigated, all *Planck* channels (30-857 GHz), all HFI channels plus the 70 GHz channel map from LFI (70-857 GHz), all HFI channels (100-857 GHz), the five lowest frequency HFI channels (100-545 GHz) and the four lowest frequency HFI channels (100-353 GHz). For each combination of frequency channels a catalogue of SZ sources was extracted, resulting in five different catalogues; the only differences between them must be entirely due to the choice of channels in the combination.

The first four of these catalogues are in good agreement in terms of the clusters detected, with all the differences amongst them being due to detections with S/N $<$ 5. The (100-353 GHz) catalogue, however, contains significantly more detections, resulting in a poor agreement between it and the other catalogues that is not limited to low S/N detections. This is interpreted as being due to the lack of a dust-dominated channel in this combination, without which it is more difficult to constrain contamination due to dust emission.

In order to assess any improvement in the S/N ratios of detected clusters with the inclusion of extra data, a robust sample of reliable sources is required. To produce this, only clusters outside the 65% dust mask and with S/N $\geq$ 8 were kept from each combination. The differences in the S/N of the same sources detected using different frequency channel combinations can then be examined. The ratio between the S/N values of the common detections in each combination to those of the (100-857) combination was then found; the mean of this ratio is shown in Table A.1. This approach clearly shows the (100-353) combination to be considerably noisier than the other combinations, which is consistent with the observations reported above. Neither the inclusion of the LFI frequency channels or just the 70 GHz channel brings any significant improvement in the S/N of the clusters. Using the six HFI channel combination results in marginally better S/N than the (100-545 GHz) combination. The frequency channel combination chosen therefore is (100-857 GHz) since this gives the highest S/N with the smallest dataset. Reducing the S/N threshold from 8 to 6 and hence doubling the number of SZ sources used to evaluate the mean ratio does not change the conclusions of this analysis.

Appendix B: Extract from the *Planck* catalogue of SZ sources

We describe here the *Planck* catalogue of SZ sources delivered by the collaboration and available together with the individual

Table A.1: Mean of the ratio of the S/N of the common detections between the catalogues produced using different frequency channel combinations, excluding all detections inside the 35% dust mask. The improvement in the S/N of the detected clusters between the (100-353) and (100-857) combinations is clearly demonstrated, as is the lack of significant improvement in S/N when LFI data is included. The improvement between the (100-545) and (100-857) combinations is smaller and in the region of 1 to 2%.

Combination	(100-353)/(100-857)	(100-545)/(100-857)	(70-857)/(100-857)	(30-857)/(100-857)
S/N ≥ 6	0.86	0.99	1.00	1.00
S/N ≥ 8	0.84	0.98	1.00	1.00

lists from all three detections methods, the union mask used by these methods and the ensemble of notes on individual clusters at http://www.sciops.esa.int/index.php?page=Planck_Legacy_Archive\&project=planck.

The union *Planck* SZ catalogue contains the coordinates and the signal-to-noise ratio of the SZ detections and a summary of the validation information, including external identification of the cluster and redshifts if they are available. The external identification quoted in the delivered product corresponds to the first identifier as defined in the external validation hierarchy, namely identification with MCXC clusters followed by Abell and Zwicky, followed by SDSS-based catalogues, followed by SZ catalogues, followed finally by searches in NED and SIMBAD. Due to the size–flux degeneracy discussed in Sect. 2.3, no reference flux quantity is outputted for the union catalogue.

The individual catalogues from the three detection methods, MMF1, MMF3, and PwS, contain the coordinates and the S/N ratio of the detections, and information on the size and flux of the clusters. The size is given in terms of θ_s and the flux is given in terms of the total integrated Comptonization parameter, $Y = Y_{5R_{500}}$. The full information on the degeneracy between and Y is provided in the form of the two-dimensional marginal probability distribution for each cluster.
The degeneracy information is provided in this form so that it can be combined with a model or external data to produce tighter constraints on the parameters. For example, combining it with an X-ray determination of the size can be done by taking a slice through the distribution at the appropriate θ_s. This is what is done in Sect. 7.2.1 and the refined measurement using X-ray information can be found in Table C.1.

Table B.1 presents an extract of the PSZ catalogue, in terms of the first rows of the online table and the following selected columns:
NAME: name of cluster.
R.A., DEC: right ascension (J2000) and declination (J2000).
S/N: signal-to-noise ratio of the SZ detection.
VALIDATION: status of the SZ detection from external validation: 20 = previously-known cluster; 10 = new confirmed *Planck* cluster; 1 = CLASS1 candidate ; 2 = CLASS2 candidate; 3 = CLASS3 candidate.
ID$_{\rm EXT}$: first external identifier of the known clusters.
z: redshift of the cluster as reported from the external validation.
COMMENTS: F = no comment; T = comment. Comments are readable in an external file.
The complete version of the PSZ catalogue also contains the additional columns:
INDEX: index of the detection, determined by the order of the clusters in the union catalogue and sorted into order of ascending Galactic longitude.
GLON, GLAT: Galactic coordinates.
POS_ERR: errors on the position.
PIPELINE: pipeline from which information is taken; namely 1 = MMF1; 2 = MMF3; 3 = PwS.
PIPE_DET: pipeline making the detection, with the following order in bits: 1st = MMF1; 2nd = MMF3; 3rd = PwS.
PCCS: flag for a match with sources from the PCCS catalogue.
COSMO: flag for those clusters that are included in the sample used for the cosmological analysis of Planck Collaboration XX (2013).

Appendix C: Outstanding outputs from the external validation

Based on the ancillary data used for the validation of the *Planck* SZ catalogue, we provide value-added information to the *Planck* SZ detections.
Namely, we provide, in addition to the first external identifier, possible other common identifiers, IDs.
We report the redshift information associated with the *Planck* clusters (z) and specify its source, (scr).
For clusters with measured redshifts, we compute the SZ-proxy Y_z and the mass estimate ($M_{500}^{Y_z}$) and associated errors. For the clusters identified with MCXC clusters we provide the SZ signal, $Y_{500,\rm PSX}$, re-extracted fixing the size to the X-ray size provided in the MCXC catalogue at the X-ray position. Note that the X-ray positions used in the present study are those quoted in the MCXC meta-catalogue. The positions reported in the ESZ sample were taken from a sampled grid of coordinates with a pixel size of 1.71 arcmin. Due to this sampling, the reported MCXC positions in the ESZ sample exhibit an average offset of 70 arcsec (less than a pixel, which varies depending on the position of the object on the sphere).
For *Planck* SZ detections not associated with a previously-known X-ray cluster and with a signal-to-noise, $(\mathrm{S/N})_{\rm RASS} \geq 1\,\sigma$, we provide the unabsorbed X-ray flux, $S_{\rm X}$ (and error), measured in an aperture of 5 arcmin in the band [0.1-2.4] keV. We only provide an upper limit in the case of $(\mathrm{S/N})_{\rm RASS} < 1\,\sigma$, except for three SZ detections for which RASS exposure is very low and $(\mathrm{S/N})_{\rm RASS} < -5\,\sigma$. The aperture is centred on the *Planck* position, except for candidates associated with a BSC source for which we adopt the X-ray position. These clusters are flagged.

Appendix D: Systematic effects on the X-ray versus SZ scaling relation

Both X-ray and SZ measurements are likely affected by systematic effects linked to e.g., background estimation and subtraction methods, calibration issues, etc. One sign of the impact of these effects is the fact that the slope of the relation between Y_{500} flux and $Y_{\rm X}/D_{\rm A}^2$ in units of arcmin^2 is $\alpha = 0.91 \pm 0.02$, which is significantly smaller than unity even after Malmquist bias correction.

Table B.1: Extract from the *Planck* catalogue of SZ sources. First rows of the online table are shown. The online table contains additional columns as documented in the Explanatory Supplement, and in the text.

NAME	R.A. degrees	Dec. degrees	S/N	Validation	ID_{EXT}	z	Comments
PSZ1 G000.08+45.15	229.19790	-0.9792795	4.60	20	RXC J1516.5-0056	0.1198	F
PSZ1 G000.42-41.84	316.06990	-41.339730	5.99	20	RXC J2104.3-4120	0.1651	F
PSZ1 G000.42-41.84	307.93571	-40.595198	5.30	20	RXC J2031.8-4037	0.3416	F
PSZ1 G000.77-35.67	244.58411	-13.070074	6.04	3	...	...	F
PSZ1 G001.00+25.71	349.60728	-36.278003	4.50	20	ACO S 1109	0.1400	F
PSZ1 G002.24-68.27	334.65975	-38.880540	7.84	20	RXC J2218.6-3853	0.1411	F
PSZ1 G002.77-56.16	234.99997	-3.2929395	7.03	20	RXC J1540.1-0318	0.1533	F
PSZ1 G002.80+39.24	292.16440	-35.711064	4.92	3	...	...	F

Table C.1: Additional information from the external validation process. `IDs` represents the first external identifier and possible other common identifiers. z is the cluster redshift. `scr` is the source from which redshift was taken. The `scr` takes defined values, e.g., 11 for redshifts from the MCXC meta-catalogue Piffaretti et al. (2011), 17 for redshifts taken from NED or SIMBAD databases, etc. Y_z is the SZ-proxy with asymmetric errors. $M_{500}^{Y_z}$ is the derived mass estimate with asymmetric errors. $Y_{500,PSX}$ is the SZ signal, re-extracted fixing the size to the X-ray size provided in the MCXC catalogue at the X-ray position, for PSZ clusters identified with MCXC clusters. S_X is the unabsorbed X-ray flux measured in an aperture of 5 arcmin in the band [0.1-2.4] keV. The aperture is centred on the *Planck* position, except for candidates associated with a BSC source for which we adopt the X-ray position. For sources with $(S/N)_{RASS} < 1\,\sigma$, we only quote an upper limit. The full table will be available at `http://www.sciops.esa.int/index.php?page=Planck_Legacy_Archive\&project=planck.` upon final acceptance of the article. Until then, it can be provided upon request.

NAME	z (scr)	Y_z	$M_{500}^{Y_z}$	S_X	IDs	$Y_{500,PSX}$
PSZ1 G000.08+45.15	0.1198 (11)	$12.35^{3.43}_{3.33}$	$3.10^{0.45}_{0.50}$	...	RXC J1516.5-0056, A2051	2.73
PSZ1 G000.42-41.84	0.1651 (11)	$14.05^{2.78}_{2.70}$	$4.46^{0.47}_{0.50}$	...	RXC J2104.3-4120, A3739	1.28
PSZ1 G000.42-41.84	0.3416 (11)	$9.14^{1.98}_{1.93}$	$6.20^{0.72}_{0.77}$	...	RXC J2031.8-4037	11.80
PSZ1 G000.77-35.67	... (-1)	...	...	≤ 1.35	...	...
PSZ1 G001.00+25.71	0.1400 (17)	$7.43^{2.71}_{2.61}$	$2.69^{0.51}_{0.58}$	1.74 ± 0.65	ACO S 1109	...
PSZ1 G002.24-68.27	0.1411 (11)	$18.29^{2.92}_{2.85}$	$4.49^{0.39}_{0.41}$	...	RXC J2218.6-3853, A3856	7.94
PSZ1 G002.77-56.16	0.1533 (11)	$26.14^{4.68}_{4.53}$	$5.91^{0.57}_{0.60}$	...	RXC J1540.1-0318, A2104	0.20
PSZ1 G002.80+39.24	... (-1)	...	...	≤ -0.07	...	...

As this is not the case for the relation in physical units (Mpc^2), the observed slope cannot be due to a true physical variation in the ratio (e.g., with mass).

SZ fluxes are subject to uncertainties due to systematic differences between measurement methods. From the comparison between `PwS` and `MMF` photometry (Sect. 2.3), we estimate that the net effect is typically 0.03 dex. The effect is independent of SZ flux, thus cannot explain the shallower than expected slope.

Uncertainties in the X-ray measurements are dominated by temperature uncertainties due to calibration systematics. We can investigate the magnitude of these effects by examining the relation between the Y_X values obtained with *XMM-Newton* by Planck Collaboration XI (2011, hereafter the PEP XI ESZ-XMM sample) to those obtained with *Chandra* in a study of 28 clusters from the same sample by Rozo et al. (2012) (hereafter the ESZ–*Chandra* sample). The *Chandra* values are larger, with a mean offset of 0.02 dex. However, there is no significant evidence of variation with Y_X, thus X-ray calibration issues again cannot explain the observed slope.

A further source of uncertainty in X-ray measurements concerns the X-ray analysis method (e.g., due to background estimation and subtraction of point sources and substructure). Rozo et al. (2012) noted the difference between the ratio obtained with ESZ–*Chandra* and ESZ-XMM samples and suggested that it might be due to *XMM-Newton* data analysis issues. The PEP XI ESZ-XMM sample was analyzed by two independent methods depending on the cluster extension in the field-of-view. Subsample A consisted of 19 nearby clusters that extend beyond the *XMM-Newton* field–of–view, and for which direct background estimates are not possible, while the background for the remaining 43 objects was estimated using a region external to the cluster. The ESZ–*Chandra* sample studied by Rozo et al. (2012) consists mostly sub-sample A objects. While systematic effects due to background estimation are certainly more important for sub-sample A than for sub-sample B, these effects cannot fully explain the observed behaviour of the Y_{500}/Y_X ratio. Indeed, excluding sub-sample A clusters, the slope of the Y_{500}–Y_X/D_A^2 relation is $\alpha = 0.89 \pm 0.04$, still significantly smaller than unity. The origin of the systematic differences between sub-sample A and B objects is unclear.

The variation of the Y_{500}/Y_X ratio with flux remains largely unexplained. It may be due to residual Malmquist bias, in addition to a complex combination of systematic effects in SZ and X–ray measurements. For instance, we note that higher flux clusters correspond to nearby objects that have larger angular sizes. The background estimate in both X-ray and SZ signals is subject to larger uncertainty in this case.

The lack of a complete explanation for the observed slope of the Y_{500}–Y_X relation, and its ultimate correction, has several implications. Firstly, the shallower slope in units of arcmin^2 translates into an over-estimate of the dispersion about the relation when measured in Mpc^2. From the difference in intrinsic scatter about the relation in both physical and arcmin units, we estimate that this effect contributes at the level of about 0.01 dex to the scatter seen in the physical Y_{500}–Y_X relation.

Secondly, the Y_{500}/Y_X ratio will depend on the exact sample definition, via the range of fluxes probed. The observed slope of $\alpha = 0.91 \pm 0.02$ translates into a variation of about ± 0.06 dex of the Y_{500}/Y_X ratio over the range of SZ fluxes studied here. The ESZ–*Chandra* objects studied by Rozo et al. (2012) lie preferentially at high fluxes, with a median flux two times higher than the PEP XI-XMM sample. For $\alpha = 0.91$, this will translate into a roughly 0.03 dex difference in the Y_{500}/Y_X ratio. The Y_{500}/Y_X ratio found by Rozo et al. (2012), $\log(Y_{500}/Y_X) = -0.088 \pm 0.012$, is significantly lower than our value of -0.027 ± 0.010. However, it can be explained by a combination of their sample definition, a neglect of Malmquist bias, and the aforementioned calibration issues between *XMM-Newton* and *Chandra*.

In summary, uncertainties on the Y_{500}/Y_X ratio are dominated by systematic effects in both X–ray and SZ measurements. This unfortunately precludes any definitive statement on the magnitude of the gas clumpiness within R_{500}. Follow-up of well-defined sub-samples (e.g., above a given S/N) should help to disentangle biases due to sample selection and measurement of the different quantities.

[1] APC, AstroParticule et Cosmologie, Université Paris Diderot, CNRS/IN2P3, CEA/lrfu, Observatoire de Paris, Sorbonne Paris Cité, 10, rue Alice Domon et Léonie Duquet, 75205 Paris Cedex 13, France
[2] Aalto University Metsähovi Radio Observatory, Metsähovintie 114, FIN-02540 Kylmälä, Finland
[3] Academy of Sciences of Tatarstan, Bauman Str., 20, Kazan, 420111, Republic of Tatarstan, Russia
[4] African Institute for Mathematical Sciences, 6-8 Melrose Road, Muizenberg, Cape Town, South Africa
[5] Agenzia Spaziale Italiana Science Data Center, c/o ESRIN, via Galileo Galilei, Frascati, Italy
[6] Agenzia Spaziale Italiana, Viale Liegi 26, Roma, Italy
[7] Astrophysics Group, Cavendish Laboratory, University of Cambridge, J J Thomson Avenue, Cambridge CB3 0HE, U.K.
[8] Astrophysics & Cosmology Research Unit, School of Mathematics, Statistics & Computer Science, University of KwaZulu-Natal, Westville Campus, Private Bag X54001, Durban 4000, South Africa
[9] Atacama Large Millimeter/submillimeter Array, ALMA Santiago Central Offices, Alonso de Cordova 3107, Vitacura, Casilla 763 0355, Santiago, Chile
[10] CITA, University of Toronto, 60 St. George St., Toronto, ON M5S 3H8, Canada
[11] CNRS, IRAP, 9 Av. colonel Roche, BP 44346, F-31028 Toulouse cedex 4, France
[12] California Institute of Technology, Pasadena, California, U.S.A.
[13] Centre for Theoretical Cosmology, DAMTP, University of Cambridge, Wilberforce Road, Cambridge CB3 0WA U.K.
[14] Centro de Astrofísica, Universidade do Porto, Rua das Estrelas, 4150-762 Porto, Portugal
[15] Centro de Estudios de Física del Cosmos de Aragón (CEFCA), Plaza San Juan, 1, planta 2, E-44001, Teruel, Spain
[16] Computational Cosmology Center, Lawrence Berkeley National Laboratory, Berkeley, California, U.S.A.
[17] Consejo Superior de Investigaciones Científicas (CSIC), Madrid, Spain
[18] DSM/Irfu/SPP, CEA-Saclay, F-91191 Gif-sur-Yvette Cedex, France
[19] DTU Space, National Space Institute, Technical University of Denmark, Elektrovej 327, DK-2800 Kgs. Lyngby, Denmark
[20] Département de Physique Théorique, Université de Genève, 24, Quai E. Ansermet,1211 Genève 4, Switzerland
[21] Departamento de Física Fundamental, Facultad de Ciencias, Universidad de Salamanca, 37008 Salamanca, Spain
[22] Departamento de Física, Universidad de Oviedo, Avda. Calvo Sotelo s/n, Oviedo, Spain
[23] Department of Astronomy and Astrophysics, University of Toronto, 50 Saint George Street, Toronto, Ontario, Canada
[24] Department of Astronomy and Geodesy, Kazan Federal University, Kremlevskaya Str., 18, Kazan, 420008, Russia
[25] Department of Astrophysics/IMAPP, Radboud University Nijmegen, P.O. Box 9010, 6500 GL Nijmegen, The Netherlands
[26] Department of Electrical Engineering and Computer Sciences, University of California, Berkeley, California, U.S.A.
[27] Department of Physics & Astronomy, University of British Columbia, 6224 Agricultural Road, Vancouver, British Columbia, Canada
[28] Department of Physics and Astronomy, Dana and David Dornsife College of Letter, Arts and Sciences, University of Southern California, Los Angeles, CA 90089, U.S.A.
[29] Department of Physics and Astronomy, University College London, London WC1E 6BT, U.K.
[30] Department of Physics and Astronomy, University of Sussex, Brighton BN1 9QH, U.K.
[31] Department of Physics, Gustaf Hällströmin katu 2a, University of Helsinki, Helsinki, Finland
[32] Department of Physics, Princeton University, Princeton, New Jersey, U.S.A.
[33] Department of Physics, University of California, Berkeley, California, U.S.A.
[34] Department of Physics, University of California, One Shields Avenue, Davis, California, U.S.A.
[35] Department of Physics, University of California, Santa Barbara, California, U.S.A.
[36] Department of Physics, University of Illinois at Urbana-Champaign, 1110 West Green Street, Urbana, Illinois, U.S.A.
[37] Dipartimento di Fisica e Astronomia G. Galilei, Università degli Studi di Padova, via Marzolo 8, 35131 Padova, Italy
[38] Dipartimento di Fisica e Scienze della Terra, Università di Ferrara, Via Saragat 1, 44122 Ferrara, Italy
[39] Dipartimento di Fisica, Università La Sapienza, P. le A. Moro 2, Roma, Italy
[40] Dipartimento di Fisica, Università degli Studi di Milano, Via Celoria, 16, Milano, Italy
[41] Dipartimento di Fisica, Università degli Studi di Trieste, via A. Valerio 2, Trieste, Italy
[42] Dipartimento di Fisica, Università di Roma Tor Vergata, Via della Ricerca Scientifica, 1, Roma, Italy
[43] Discovery Center, Niels Bohr Institute, Blegdamsvej 17, Copenhagen, Denmark
[44] Dpto. Astrofísica, Universidad de La Laguna (ULL), E-38206 La Laguna, Tenerife, Spain
[45] European Southern Observatory, ESO Vitacura, Alonso de Cordova 3107, Vitacura, Casilla 19001, Santiago, Chile
[46] European Space Agency, ESAC, Planck Science Office, Camino bajo del Castillo, s/n, Urbanización Villafranca del Castillo, Villanueva de la Cañada, Madrid, Spain
[47] European Space Agency, ESTEC, Keplerlaan 1, 2201 AZ Noordwijk, The Netherlands
[48] Finnish Centre for Astronomy with ESO (FINCA), University of Turku, Väisäläntie 20, FIN-21500, Piikkiö, Finland
[49] GEPI, Observatoire de Paris, Section de Meudon, 5 Place J. Janssen, 92195 Meudon Cedex, France
[50] Helsinki Institute of Physics, Gustaf Hällströmin katu 2, University of Helsinki, Helsinki, Finland

[51] INAF - Osservatorio Astrofisico di Catania, Via S. Sofia 78, Catania, Italy
[52] INAF - Osservatorio Astronomico di Padova, Vicolo dell'Osservatorio 5, Padova, Italy
[53] INAF - Osservatorio Astronomico di Roma, via di Frascati 33, Monte Porzio Catone, Italy
[54] INAF - Osservatorio Astronomico di Trieste, Via G.B. Tiepolo 11, Trieste, Italy
[55] INAF/IASF Bologna, Via Gobetti 101, Bologna, Italy
[56] INAF/IASF Milano, Via E. Bassini 15, Milano, Italy
[57] INFN, Sezione di Bologna, Via Irnerio 46, I-40126, Bologna, Italy
[58] INFN, Sezione di Roma 1, Università di Roma Sapienza, Piazzale Aldo Moro 2, 00185, Roma, Italy
[59] IPAG: Institut de Planétologie et d'Astrophysique de Grenoble, Université Joseph Fourier, Grenoble 1 / CNRS-INSU, UMR 5274, Grenoble, F-38041, France
[60] ISDC Data Centre for Astrophysics, University of Geneva, ch. d'Ecogia 16, Versoix, Switzerland
[61] IUCAA, Post Bag 4, Ganeshkhind, Pune University Campus, Pune 411 007, India
[62] Imperial College London, Astrophysics group, Blackett Laboratory, Prince Consort Road, London, SW7 2AZ, U.K.
[63] Infrared Processing and Analysis Center, California Institute of Technology, Pasadena, CA 91125, U.S.A.
[64] Institut Néel, CNRS, Université Joseph Fourier Grenoble I, 25 rue des Martyrs, Grenoble, France
[65] Institut Universitaire de France, 103, bd Saint-Michel, 75005, Paris, France
[66] Institut d'Astrophysique Spatiale, CNRS (UMR8617) Université Paris-Sud 11, Bâtiment 121, Orsay, France
[67] Institut d'Astrophysique de Paris, CNRS (UMR7095), 98 bis Boulevard Arago, F-75014, Paris, France
[68] Institute for Space Sciences, Bucharest-Magurale, Romania
[69] Institute of Astronomy and Astrophysics, Academia Sinica, Taipei, Taiwan
[70] Institute of Astronomy, University of Cambridge, Madingley Road, Cambridge CB3 0HA, U.K.
[71] Institute of Theoretical Astrophysics, University of Oslo, Blindern, Oslo, Norway
[72] Instituto de Astrofísica de Canarias, C/Vía Láctea s/n, La Laguna, Tenerife, Spain
[73] Instituto de Física de Cantabria (CSIC-Universidad de Cantabria), Avda. de los Castros s/n, Santander, Spain
[74] Jet Propulsion Laboratory, California Institute of Technology, 4800 Oak Grove Drive, Pasadena, California, U.S.A.
[75] Jodrell Bank Centre for Astrophysics, Alan Turing Building, School of Physics and Astronomy, The University of Manchester, Oxford Road, Manchester, M13 9PL, U.K.
[76] Kavli Institute for Cosmology Cambridge, Madingley Road, Cambridge, CB3 0HA, U.K.
[77] LAL, Université Paris-Sud, CNRS/IN2P3, Orsay, France
[78] LERMA, CNRS, Observatoire de Paris, 61 Avenue de l'Observatoire, Paris, France
[79] Laboratoire AIM, IRFU/Service d'Astrophysique - CEA/DSM - CNRS - Université Paris Diderot, Bât. 709, CEA-Saclay, F-91191 Gif-sur-Yvette Cedex, France
[80] Laboratoire Traitement et Communication de l'Information, CNRS (UMR 5141) and Télécom ParisTech, 46 rue Barrault F-75634 Paris Cedex 13, France
[81] Laboratoire de Physique Subatomique et de Cosmologie, Université Joseph Fourier Grenoble I, CNRS/IN2P3, Institut National Polytechnique de Grenoble, 53 rue des Martyrs, 38026 Grenoble cedex, France
[82] Laboratoire de Physique Théorique, Université Paris-Sud 11 & CNRS, Bâtiment 210, 91405 Orsay, France
[83] Lawrence Berkeley National Laboratory, Berkeley, California, U.S.A.
[84] MPA Partner Group, Key Laboratory for Research in Galaxies and Cosmology, Shanghai Astronomical Observatory, Chinese Academy of Sciences, Nandan Road 80, Shanghai 200030, China
[85] Max-Planck-Institut für Astrophysik, Karl-Schwarzschild-Str. 1, 85741 Garching, Germany
[86] Max-Planck-Institut für Extraterrestrische Physik, Giessenbachstraße, 85748 Garching, Germany
[87] McGill Physics, Ernest Rutherford Physics Building, McGill University, 3600 rue University, Montréal, QC, H3A 2T8, Canada
[88] MilliLab, VTT Technical Research Centre of Finland, Tietotie 3, Espoo, Finland
[89] Moscow Institute of Physics and Technology, Dolgoprudny, Institutsky per., 9, 141700, Russia
[90] Niels Bohr Institute, Blegdamsvej 17, Copenhagen, Denmark
[91] Observational Cosmology, Mail Stop 367-17, California Institute of Technology, Pasadena, CA, 91125, U.S.A.
[92] Optical Science Laboratory, University College London, Gower Street, London, U.K.
[93] SB-ITP-LPPC, EPFL, CH-1015, Lausanne, Switzerland
[94] SISSA, Astrophysics Sector, via Bonomea 265, 34136, Trieste, Italy
[95] SUPA, Institute for Astronomy, University of Edinburgh, Royal Observatory, Blackford Hill, Edinburgh EH9 3HJ, U.K.
[96] School of Physics and Astronomy, Cardiff University, Queens Buildings, The Parade, Cardiff, CF24 3AA, U.K.
[97] Space Research Institute (IKI), Russian Academy of Sciences, Profsoyuznaya Str, 84/32, Moscow, 117997, Russia
[98] Space Sciences Laboratory, University of California, Berkeley, California, U.S.A.
[99] Special Astrophysical Observatory, Russian Academy of Sciences, Nizhnij Arkhyz, Zelenchukskiy region, Karachai-Cherkessian Republic, 369167, Russia
[100] Stanford University, Dept of Physics, Varian Physics Bldg, 382 Via Pueblo Mall, Stanford, California, U.S.A.
[101] Sub-Department of Astrophysics, University of Oxford, Keble Road, Oxford OX1 3RH, U.K.
[102] TÜBİTAK National Observatory, Akdeniz University Campus, 07058, Antalya, Turkey
[103] Theory Division, PH-TH, CERN, CH-1211, Geneva 23, Switzerland
[104] UPMC Univ Paris 06, UMR7095, 98 bis Boulevard Arago, F-75014, Paris, France
[105] Universität Heidelberg, Institut für Theoretische Astrophysik, Philosophenweg 12, 69120 Heidelberg, Germany
[106] Université Denis Diderot (Paris 7), 75205 Paris Cedex 13, France
[107] Université de Toulouse, UPS-OMP, IRAP, F-31028 Toulouse cedex 4, France
[108] Universities Space Research Association, Stratospheric Observatory for Infrared Astronomy, MS 232-11, Moffett Field, CA 94035, U.S.A.
[109] University Observatory, Ludwig Maximilian University of Munich, Scheinerstrasse 1, 81679 Munich, Germany
[110] University of Granada, Departamento de Física Teórica y del Cosmos, Facultad de Ciencias, Granada, Spain
[111] University of Miami, Knight Physics Building, 1320 Campo Sano Dr., Coral Gables, Florida, U.S.A.
[112] Warsaw University Observatory, Aleje Ujazdowskie 4, 00-478 Warszawa, Poland